DISSERTATION

Determination of Arctic land surface and soil properties with Synthetic Aperture Radar information from satellites

Ausgeführt zum Zweck der Erlangung des akademischen
Grades eines Doktors der technischen Wissenschaften

unter der Leitung von
Priv.-Doz. Dipl.-Geogr. Annett Bartsch, PhD

E120.1
Department für Geodäsie und Geoinformation
Forschungsgruppe Fernerkundung

eingereicht an der Technischen Universität Wien
Fakultät für Mathematik und Geoinformation

von

Dipl.-Ing. Barbara Widhalm
Matrikelnummer: 0626444
Viktoriagasse 7/2/15
1150 Wien

Wien, am   ....

Eidesstattliche Erklärung

Hiermit erkläre ich, dass ich diese Arbeit selbständig verfasst habe, dass ich die verwendeten Quellen und Hilfsmittel vollständig angegeben habe und dass ich die Stellen der Arbeit einschließlich Tabellen, Karten und Abbildungen -, die anderen Werken oder dem Internet im Wortlaut oder dem Sinn nach entnommen sind, auf jeden Fall unter Angaben der Quelle als Entlehnt kenntlich gemacht habe.

Wien, am ....

Parts of this cumulative thesis have been published in peer-reviewed journals (3) and as proceedings papers (2):

Widhalm, B., A. Bartsch, and B. Heim, A novel approach for the characterization of tundra wetland regions with C-band SAR satellite data, *International Journal of Remote Sensing*, *36*(22), 5537–5556, doi: 10.1080/01431161.2015.1101505, 2015

Widhalm, B., A. Bartsch, M. Leibman, and A. Khomutov, Active-layer thickness estimation from X-band SAR backscatter intensity, *The Cryosphere*, *11*(1), 483–496, doi: 10.5194/tc-11-483-2017, 2017

Widhalm, B., A. Bartsch, and R. Goler, Simplified normalization of C-band synthetic aperture radar data for terrestrial applications in high latitude environments, *Remote Sensing*, *10*(4), doi: 10.3390/rs10040551, 2018

Widhalm, B., A. Bartsch, M. B. Siewert, G. Hugelius, B. Elberling, M. Leibman, Y. Dvornikov, and A. Khomutov, Site scale wetness classification of tundra regions with C-band SAR satellite data, in *Proc. 'Living Planet Symposium 2016', Prague, Czech Republic*, ESA SP-740, 2016

Widhalm, B., A. Bartsch, A. Roth, and M. Leibman, Classification of tundra regions with polarimetric TerraSAR-X data, in *Proc. 'IGARSS 2018', Valencia, Spain*, in press

The work has been conducted as part of the following research projects:

Abstract

Permafrost is an essential climate variable and prone to change with future warming. Extensive permafrost degradation is likely to occur within this century. Currently stored carbon will potentially be mobilized effecting the global carbon cycle. Furthermore permafrost degradation will cause impacts on infrastructure and ecosystems. Permafrost monitoring is therefore essential and often challenging due to the fact that Arctic regions affected by permafrost are vast and often remote. Therefore Remote Sensing holds great potential due to continuous coverage.

As permafrost is a subsurface phenomenon it cannot be measured directly via satellite data. However its state can be indirectly derived and degradation impacts can be observed. This thesis focuses on the possibilities of synthetic aperture radar (SAR) for circumpolar monitoring. Relationships between SAR backscatter and arctic land cover as well as soil properties are explored, incorporating SAR data of different spatial scales and wavelengths as well as in situ data gathered during field campaigns.

In a first publication the influence of vegetation types of certain wetness regimes on C-band summer and winter backscatter is investigated in order to derive a circumpolar wetness map and subsequently to apply at site scale and medium resolution.

Soil properties are further explored within a second paper, where the interrelations of arctic vegetation, soil moisture and active layer thickness are analyzed and connected to X-band backscatter as to delineate a continuous active layer map for a study site on the central Yamal Peninsula.

Within a third paper a simplified normalization approach is introduced by investigating land cover specific incidence angle dependencies for arctic regions.

Zusammenfassung

Permafrost ist eine essentielle Klimavariable, die durch zukünftige Erderwärmung gefährdet ist. Noch in diesem Jahrhundert wird ein erheblicher Permafrostrückgang erwartet. Kohlenstoff, welcher zurzeit im Permafrost gespeichert ist, wird voraussichtlich freigesetzt werden, mit negativen Auswirkungen auf den globalen Kohlenstoffkreislauf. Daher ist Permafrostmonitoring von großer Bedeutung. Da von Permafrost betroffene Regionen oft eine große Ausdehnung haben und zusätzlich schwer zugänglich sind, stellt dies eine besondere Herausforderung dar. In diesem Zusammenhang besitzt Fernerkundung durch die Möglichkeit der kontinuierlichen Erfassung ein großes Potential.

Da Permafrost eine Erscheinungsform des Untergrundes ist kann er nicht direkt mittels Satellitendaten erfasst werden. Jedoch lässt sich sein Zustand indirekt ableiten und Auswirkungen verursacht durch Permafrostrückgang können beobachtet werden.

Diese Arbeit befasst sich mit den Möglichkeiten von Synthetic Aperture Radar (SAR) Rückstreuung für circumpolares Monitoring. Es werden die Beziehungen zwischen SAR Rückstreuung und arktischer Landbedeckung als auch Bodeneigenschaften untersucht. Hierfür werden SAR Daten unterschiedlicher räumlicher Auflösung und Wellenlänge, als auch in situ Daten von Feldkampagnen herangezogen.

In der ersten Arbeit werden die Einflüsse von Vegetationsarten verschiedener Feuchtigkeitsregime auf C-Band Sommer- und Winterrückstreueigenschaften untersucht um eine circumpolare Feuchtigkeitskarte abzuleiten. Diese Methode wird schließlich auch lokal und mit mittlerer Auflösung angewendet.

Weiters werden Bodeneigenschaften in einer zweiten Arbeit analysiert. Hierfür werden die Zusammenhänge zwischen arktischer Vegetation, Bodenfeuchte und Auftautiefe begutachtet und mit X-Band Rückstreuung in Zusammenhang gebracht um für das Untersuchungsgebiet

auf der Yamal-Halbinsel eine kontinuierliche Auftautiefenkarte abzuleiten.

In einer dritten Arbeit wird eine vereinfachte Normalisierungsmethode vorgestellt. Hierfür werden landbedeckungsspezifische Einfallswinkelabhängigkeiten für arktische Regionen untersucht.

Acknowledgements

I would like to thank everybody who supported me during the course of this dissertation. First and foremost I owe great gratitude to my supervisor Annett Bartsch. Thank you for your mentoring and constant support throughout the years. I would also like to thank my coauthors for their scientific input. Many thanks to those I met during my fieldwork and throughout the projects, during which this thesis was conducted, for making it a unique experience. I would also like to thank my colleagues at the Technical University of Vienna, where I started this dissertation and my colleagues at the ZAMG for their support. Last but not least, many thanks to my friends and family for always being there for me.

Contents

List of Figures

List of Tables

Chapter 1

Introduction

1.1 Problem statement

Permafrost is a key element of the terrestrial Cryosphere and an Essential Climate Variable (ECV). It is defined as ground that remains continuously at or below 0°C for at least two consecutive years [*Harris et al.*, 1988]. About a quarter of the landmasses of the northern hemisphere is underlain by Permafrost [*Brown et al.*, 1997], with thicknesses ranging from a view centimeters to several hundred meters. Permafrost is predominantly influenced by climate and is therefore prone to change with observed and projected future warming. Due to this influencing factor, permafrost inherently increases for increasing latitudes, but it can also be found at higher elevation of mountainous regions. It can therefore be separated into mountain permafrost and lowland permafrost [*Westermann et al.*, 2015a]. Permafrost can be characterized by properties like ice content, permafrost temperature or depth of seasonal thaw. This layer, which annually freezes and thaws and is underlain by permafrost is described as the active layer. It is controlled by ambient temperature and is also influenced by insulating layers like snow cover and vegetation, slope, drainage, soil type, organic layer thickness and water content [*Leibman*, 1998; *Shiklomanov and Nelson*, 1999; *Hinkel and Nelson*, 2003; *Kelley et al.*, 2004; *Melnikov et al.*, 2004; *Vasiliev et al.*, 2008]. It can range in thickness from a few centimeters up to several meters. In this layer most ecological, hydrological and biochemical activities take place [*Kane et al.*, 1991; *Brown et al.*, 2000] and it is therefore an essential permafrost variable to monitor. Permafrost is projected to decline within this century, caused by climate change, which

leads to widespread thawing and degradation of permafrost. Permafrost temperature measurements in boreholes indicate a warming of Northern Hemispheres permafrost and a degradation in discontinuous permafrost during the last three decades [*Romanovsky et al.*, 2010]. Climate models also project strong future warming leading to a mobilization of carbon and nitrogen currently stored in permafrost. Besides its effects on global carbon cycle, permafrost degradation will lead to impacts on infrastructure and ecosystems. Land cover is expected to change gradually by shrub expansion and landscapes dry and wet due to hydrological disturbances. More rapid changes include thaw slumps, active layer detachment slides, thermokarst or erosion, as well as lake formation, expansion or shrinkage [*Grosse et al.*, 2011].

Due to its implications in global climate and its vulnerability to climate change, it is necessary to monitor permafrost. Remote sensing provides a valuable tool for this purpose. Arctic regions affected by permafrost are vast and often remote providing limited access. Field sites are often sparse with only few continuous datasets. Here remote sensing can provide continuous coverage of large areas. Although permafrost cannot be measured directly by remote sensing, many remote sensing target characteristics provide informations from which the permafrost state can be indirectly derived as well as enabling the mapping of degradation impacts and hazards [*Westermann et al.*, 2015a]. Possible targets strongly depend on sensor parameters such as frequency or spatial and temporal resolution. Sensors provide data from for instance visible to infrared spectrum, as well as passive or active microwave, like synthetic aperture radar (SAR), Scatterometer or Altimeter. Features indicating changing permafrost conditions such as thermokarst, thaw slumps or coastal erosions can be monitored, as well as vegetation types or surface covers correlating with the presence of permafrost [*Westermann et al.*, 2015a]. Furthermore physical parameters related to permafrost can be derived such as land surface temperature or the freeze-thaw state of surfaces.

In this thesis the possibilities of microwave remote sensing will be further emphasized. SAR data provides great advantages for the monitoring of arctic regions. It is hardly affected by cloud cover and independent of sunlight, providing consistent data for areas which are often clouded and subject to polar nights or low sun angles. Target parameters

incorporate seasonal and long term changes of open water extent [e.g., *Bartsch et al.*, 2012; *Muster et al.*, 2013], as well as changes of bottom fast lake ice [e.g., *Surdu et al.*, 2014; *Antonova et al.*, 2016a; *Bartsch et al.*, 2017], the detection of features related to periglacial processes [e.g., *Stettner et al.*, 2017; *Jones et al.*, 2012] or terrain changes like frost heave and subsidence detectable by interferometric SAR (InSAR, [e.g., *Liu et al.*, 2010, 2014; *Chen et al.*, 2013; *Antonova et al.*, 2018]).

SAR backscatter intensity is dependent on sensor parameters like incidence angle, polarization and wavelength, as well as on target parameters such as surface roughness, vegetation structure and dielectric properties [*Ulaby et al.*, 1982]. Due to the interconnections of backscatter, vegetation and soil properties like soil type, soil moisture and active layer, SAR data may be a valuable proxy to determine permafrost relevant soil variables.

For many applications an accurate and consistent representation of land cover of northern high latitudes is essential [*Westermann et al.*, 2015b; *Ottlé et al.*, 2013]. Although the suitability of satellite data has been demonstrated on local and regional scale, a suitable circumpolar map does not yet exist [*Bartsch et al.*, 2016a]. Land cover maps needed for permafrost modelling often lack in detail and consistency [*Trofaier et al.*, 2017]. Circumpolar land cover information is needed for Arctic regions, especially related to sub ground properties like wetness, active layer thickness or soil organic carbon content.

A representation of arctic wetlands and spatial wetness patterns is required for applications like upscaling of flux measurements or climate modelling. Wetland classes of available land cover maps often lack in accuracy for Arctic regions [*Krankina et al.*, 2011] and global data sets of surface soil moisture only provide relatively coarse spatial resolution. The comprehensive record of medium-resolution Envisat Advanced SAR Global Monitoring mode (ASAR GM, 1 km spatial resolution) holds great potential to derive general wetness patterns for the Arctic [*Bartsch et al.*, 2009]. More recently the Sentinel-1 satellites continue this C-band data set, providing even higher resolution (5 - 40 m spatial resolution). TerraSAR-X offers X-band data at a spatial resolution of 3 m (StripMap mode). Such high spatial resolution data is essential for Arctic regions, where heterogeneity is a major issue. Processing and data storage efforts are consequently increased for extensive higher resolution data sets, calling for faster processing routines.

1.2 Objectives

As shown in section 1.1 remote sensing is a valuable tool for monitoring and providing useful products for Arctic research. Meeting the needs for earth observation products for these often remote and vast regions, this thesis aims to explore the potentials of SAR data for circumpolar monitoring, incorporating data of different spatial scales and wavelengths. The focus of this thesis lies on soil properties and their connections to land cover and consequently SAR backscatter. In Particular the interrelations between SAR backscatter intensity and arctic vegetation types, surface roughness, wetness and eventually active layer thickness and SOC content are explored. Furthermore the influence of arctic vegetation types on incidence angle dependence of SAR backscatter is investigated and employed in order to implement a simplified normalization approach and eventually enable circumpolar monitoring and higher spatial resolution than available so far.

The following objectives are addressed within the research articles which form the basis of this thesis:

- Investigating the influence of arctic wetlands on summer and winter C-band backscatter and delineating a circumpolar wetness map as well as applying the found method at site scale and medium resolution.

- Exploring the connections of X-band backscatter and active-layer thickness in order to delineate a continuous active-layer map.

- Analyzing land cover specific incidence angle dependencies of arctic regions in order to derive a simplified normalization approach for C-band HH data and to classify X-band polarimetric data.

1.3 Methodology

The following methods have been used in the course of this thesis:

- Literature review, focusing on microwave remote sensing with emphasis on Arctic regions, land cover of the Arctic and their inherent wetness conditions, relations to soil properties including active-layer thickness and incidence angle dependencies.

- Preprocessing of SAR data using the SAR Geophysical Retrieval Toolbox (SGRT), the software NEST (Next ESA SAR Toolbox), ESAs Sentinel Application Platform (SNAP), incorporating calibration, terrain correction, resampling and normalization as well as use of Python for adapted normalization and batch processing.

- Statistical and time series analysis of backscatter intensity with respect to land cover types and soil properties such as soil moisture and active-layer thickness including GIS analyses.

- Statistical analysis of backscatter dependence on incidence angle and connections on vegetation cover available from external datasets as well as own dedicated field surveys.

- Field surveys including the collection of in situ reference data like vegetation survey, soil moisture measurements and active-layer thickness measurements.

1.4 Summary of publications

1.4.1 Publication I: A novel approach for the characterization of tundra wetland regions with C-band SAR satellite data

A representation of spatial wetness patterns is required for many Arctic research applications, such as upscaling of flux measurements or soil properties like wetness and carbon content which impact heat transfer and are therefore relevant for permafrost modeling. Despite this current need for a circumpolar consistent wetland map, available datasets often lack necessary accuracy or thematic detail [*Bartsch et al.*, 2016a]. While wetland classes do exist for available land cover maps, their accuracy for Arctic regions, especially concerning different types, remains largely uncertain [*Krankina et al.*, 2011]. Existing global soil moisture and inundation data sets provide only coarse resolution (25-50 km) ([e.g., *Kerr et al.*, 2001; *Njoku*, 2004; *Naeimi et al.*, 2009a] and hamper their suitability for Arctic regions, which often feature high heterogeneity and making higher resolution products a necessity [*Högström et al.*, 2014]. Synthetic Aperture Radar (SAR) data has been shown to be regionally applicable for wetland mapping, with Envisat Advanced SAR Global Monitoring mode (ASAR GM) providing an extensive global medium-resolution

data set [*Bartsch et al.*, 2009]. In this study circumpolar Envisat ASAR GM data is therefore analyzed, emphasizing on spatial wetness patterns.

Radar backscatter intensity depends on sensor parameters like incidence angle, wavelength and polarization, and geometric parameters such as surface roughness and vegetation structure, as well as soil properties [*Ulaby et al.*, 1982]. The dielectric constant, which depicts material characteristics, is highly dependent on soil moisture content and therefore leads to higher backscatter values under wet soil conditions. To derive relative soil moisture, location specific dry (minimum) and wet (maximum) backscatter references can be derived [*Wagner et al.*, 1999]. However this dry reference has to be defined differently for wetland areas, which never dry out. Because backscatter values of frozen soils are similar to dry soils, the backscatter of winter data can be used instead [*Duguay et al.*, 2013; *Naeimi et al.*, 2012]. *Bartsch et al.* [2011] postulated the combined use of summer and winter minimum backscatter to identify Arctic wetlands. In this study we therefor processed circumpolar summer (July and August) and winter (December) ASAR GM data of HH polarization of the years 2005 - 2011. The data was calibrated, geocoded, orthorectified and normalized to a common incidence angle of 30° by using the SAR Geophysical Retrieval Toolbox (SGRT, Vienna University of Technology, *Sabel et al.* [2012]). Summer and winter dry-reference maps were calculated, representing conditions of minimum soil moisture and frozen conditions respectively. Winter minimum backscatter values, as well as their differences to summer minimum values were compared to the Circumpolar Arctic Vegetation Map (CAVM, *Walker et al.* [2002]), which is the only circumpolar product with adequate thematic detail and can be differentiated into vegetation classes of three different moisture levels (wet, medium and dry).

Results showed that, although backscatter values increase with wetness, it does not have an essential influence on backscatter values of permanently wet Arctic areas. Summer as well as winter values were found to be lower for wetter areas. Due to comparable summer and winter values it can be concluded that the main influences on backscatter amount are surface roughness and volume scattering within the vegetation, which showed to decrease for land cover types typical for wetter regions. Summer to winter backscatter differences, which depend mostly on soil moisture content, expectedly showed higher values

for wet regions. However due to similar summer and winter values, the sole use of winter data proved to be more applicable due to better separability, showing low values for wet areas (<-16.5 dB , normalized to 30 incidence angele) and high values for dryer regions (>-15.2 dB). Thresholds delineated based on the CAVM were used for a simple hierarchical classification. Due to a lack of comparable regional to circumpolar data with respect to thematic detail, the derived wetland map could not directly be validated. However the wetness level map was assessed with land cover maps, indicating its applicability. A subsequent study which made use of the wetness levels showed that these winter backscatter classes can be used as proxy for actual amounts of soil organic carbon [*Bartsch et al.*, 2016b] as well as maximum active layer thickness (additional publication A: *Widhalm et al.* [2016]). The latter study also demonstrated the transferability of the approach to different ENVISAT ASAR modi.

1.4.2 Publication II: Active-layer thickness estimation from X-band SAR backscatter intensity

The active-layer is defined as the top layer of ground underlain by permafrost that is subject to annual thawing and freezing. It is an important parameter for monitoring the state of permafrost and therefore an essential climate variable [*Schaefer et al.*, 2015]. The active-layer thickness (ALT), predominantly controlled by ambient temperature is also influenced by insulating layers like snow cover and vegetation, slope, drainage, soil type, organic layer thickness and water content [*Leibman*, 1998; *Shiklomanov and Nelson*, 1999; *Hinkel and Nelson*, 2003; *Kelley et al.*, 2004; *Melnikov et al.*, 2004; *Vasiliev et al.*, 2008]. Because of interactions between these often spatially very variable surface and subsurface variables, the ALT may vary substantially over short lateral distances [*Shiklomanov and Nelson*, 1999; *Leibman et al.*, 2012].

Traditionally the active-layer is measured by probing with metal rods. However these in situ measuring methods are not efficient at regional scale. Although accurate analytical procedures do exist [*Harlan and Nixon*, 1978], they are often labor-intensive and limited in spatial coverage [*Gangodagamage et al.*, 2014]. Remote sensing holds a great potential to delineate active-layer thickness continuously over larger scales. It has been shown

that empirical relationships between in situ measurements and remotely sensed attributes can be used to derive ALT maps. Normalized difference vegetation index (NDVI) values [*McMichael et al.*, 1997; *Kelley et al.*, 2004], as well as delineated land cover classes and digital elevation models (Nelson et al. 1997, Peddle and Franklin 1993) have been used for the delineation of ALT. Furthermore interferometrically measured subsidence rates have been demonstrated to be applicable for ALT derivation under saturated soil conditions [*Schaefer et al.*, 2015]. Backscatter intensity values had so far not been investigated for this purpose.

In this study the common dependency of ALT and X-band backscatter values on land cover types, as well as the interrelation of terrain, vegetation and soil moisture is investigated and exploited in order to derive ALT maps. Six TerraSAR-X images of HH polarization (spatial resolution of 3m) from August 2014 and 2015 were preprocessed using the software NEST (Next ESA SAR Toolbox) and averaged over time as well as spatially filtered in order to minimize effects due to speckle. In situ data was collected over the study site on the central Yamal Peninsula, which is dominated by highly dissected alluvial-lacustrine-marine plains and terraces and underlain by continuous permafrost [*Leibman et al.*, 2015]. ALT was measured at four grid sites including the Circumpolar Active Layer Monitoring (CALM) grid. The three monitoring sites used for calibration featured more or less homogeneous vegetation. For the far more heterogeneous CALM site additionally soil moisture measurements of the top 5 cm and a vegetation survey was conducted. The dominant vegetation cover within a 3 x 3 m area was determined and the following classes were distinguished: cryptogam crust, low shrubs (<15 cm), medium shrubs (1530 cm), high shrubs (>30 cm), grass and moss, a class where sedges dominate and classes of mixed vegetation.

Results showed that higher ALT values generally corresponded with higher backscatter values for the tested ALT range of 40-140 cm, yielding a linear relation with an R^2 of 0.66 for the calibration sites and a RMSE of 20 cm over the CALM site, which was used for validation. Higher willow shrubs, which featured higher backscatter amount due to volume scattering coincided with greater ALT values, due to the retention of snow and the fact that they were predominantly found on saline clay, which can lead to higher ALT

values measured by probing caused by a deviation of the freezing point. Soil moisture is another factor that influences backscatter amount and ALT. A rise in soil moisture and therefore dielectric constant, increases backscatter and also ALT due to an increased heat flux and an enhanced conductive heat transfer into subsurface layers [*Gross et al.*, 1990; *Shiklomanov et al.*, 2010]. Validation at the CALM grid revealed lower accuracies for the backscatter delineated ALT map for areas of mixed vegetation and cryptogam crusts. However results indicated a better performance than NDVI for higher ALT, yet investigations with higher spatial resolution optical data, than the here used Landsat data (30 m spatial resolution), would be required for confirmation. This study also only used data from a certain incidence angle. A subsequent study demonstrated the role of incidence angle for tundra vegetation at X-band (additional publication B: *Widhalm et al.* [in press]). Indicators which rely on ratios (such as certain Kennaugh-parameters) can provide a solution. In case of direct use of backscatter, land cover dependent normalization is required. This was further emphasized for C-band in Publication III of this thesis [*Widhalm et al.*, 2018]

1.4.3 Publication III: Simplified normalization of C-Band synthetic aperture radar data for terrestrial applications in high latitude environments

The incidence angle has a major effect on backscatter values of Synthetic Aperture Radar (SAR) acquisitions. For many applications it is therefore necessary to eliminate this effect and to normalize the scenes to a single incidence angle in order to achieve comparability of images with different acquisition geometry. Various approaches for angular normalization do exist. Advanced approaches use histogram or frequency matching [*Mladenova et al.*, 2013], while many empirical approaches rely on fitting a first or second order polynomial to incidence angle and backscatter values [*Wickel et al.*, 2001; *Loew et al.*, 2006; *Pathe et al.*, 2009; *Baup et al.*, 2007; *Van Doninck et al.*, 2014; *Bartsch et al.*, 2017]. As shown in previous studies [*Mäkynen et al.*, 2002; *Van Doninck et al.*, 2014] the relationship between incidence angle and backscatter can be considered as linear for a limited incidence angle range, which approximately corresponds to the incidence angle range covered by Sentinel-1. The variation of backscatter with incidence angle depends on scattering mechanisms and

therefore on surface variables such as surface roughness and vegetation [*Ulaby et al.*, 1982; *Frison and Mougin*, 1996; *Menges et al.*, 2001]. The dependence decreases with increasing surface roughness [*Mäkynen et al.*, 2002] and varies with liquid water content [*Pathe et al.*, 2009]. By excluding the effects of liquid water content, backscatter only depends on surface roughness and vegetation structure. This can be achieved by using acquisitions under frozen conditions. Frozen surface backscatter information can be used for a variety of applications, like for the derivation of wetness patterns (Publication I,*Widhalm et al.* [2015]), as a proxy for soil organic carbon [*Bartsch et al.*, 2016b], or as dry reference for the retrieval of relative soil moisture [*Pathe et al.*, 2009]. In these studies Envisat ASAR data was used and data was normalized by deriving a linear relationship for every pixel individually. Sentinel-1 provides higher resolution (93 m x 87 m, (range x azimuth) in EW GRDM (ExtraWide Swath, Ground Range Detected Medium Resolution) mode) and is therefore of further benefit in heterogeneous Arctic regions. Higher spatial resolution data does however increase processing and data storage efforts in case of the pixel based normalization procedure. In this study a simplified normalization approach for winter (frozen surface) data of Arctic regions is therefore introduced, which is applicable for single scenes. The relationship of incidence angle and Sentinel-1 backscatter across the tundra to boreal transition zone is analyzed in order to derive a universal normalization function for this region.

Sentinel-1 EW GRDM data of HH polarization of December 2014-2016 was preprocessed using ESAs Sentinel Application Platform (SNAP). Backscatter and local incidence angle for land cover classes of three Arctic land cover maps was analyzed and in most cases revealed an adequate linear dependence for the existing incidence angle range. As expected, tall vegetation like forest showed higher backscatter and less dependence on incidence angle variations, than smoother surfaces lake non-vegetated, plain coastal areas. A linear relation between the slope of the regression lines and the backscatter at a constant local incidence angle could be observed and allowed the derivation of a normalization function which depends on backscatter amount and local incidence angle. Comparisons with the pixel based normalization approach revealed good agreements, however deviations were found in mountainous regions, where the assumed linear relationship was no longer valid

due to an increase in incidence angle range [*Van Doninck et al.*, 2014]. Derived minimum backscatter images proved to be dependent on the number of used images. This effect could however be averted by using the 10th percentile. Nevertheless comparisons of Sentinel-1 frozen ground maps to those of Envisat ASAR GM revealed differences between study sites, which could not be explained explicitly with the available reference data and may result from scale and thematic content differences. Nevertheless, higher resolution SAR data can be expected to be beneficial in heterogeneous Arctic landscapes and therefore making less computationally intensive normalization approaches essential.

1.4.4   Additional publication A: Site scale wetness classification of tundra regions with C-Band SAR satellite data

As described in Publication I [*Widhalm et al.*, 2015], Envisat ASAR GM (1 km spatial resolution) minimum winter backscatter data can be used to derive circumpolar wetness patterns, which are essential for applications like upscaling of carbon fluxes and pools or for modelling of permafrost properties. Heterogeneity is a major challenge for Arctic regions and higher resolution maps are therefore essential. In this publication the applicability of the introduced approach is therefore investigated for site scale using Envisat ASAR WS (Wide Swath) data ($\sim$120 m spatial resolution).

ASAR WS data of at least one December acquisition of five years each (2007 - 2011) was processed for selected arctic study sites using the software NEST. Minimum backscatter values were calculated and due to a lack of normalisation for local incidence angle, corrected for a resulting offset between GM and WS data. The resulting WS wetness maps where then compared to previous results of GM and to landcover maps and field points. Results showed that, although WS wetness classes did not necessarily dominate within their respective GM counterparts, an increase of dry and decrease of wet WS pixels could be observed for wet to dry GM classes. Furthermore, the method proved to be not applicable for regions where scattering due to tree trunks may occur and showed limitations for land cover types which are not exclusive for one wetness state.

1.4.5 Additional publication B: Classification of tundra regions with polarimetric TerraSAR-X data

In this publication polarimetric TerraSAR-X data is used to derive local land cover classifications, identifying periglacial features and process areas like thaw slumps, wetland areas and thaw lakes. Polarimetric data (HH/VV polarisation) is used to derive so called Kennaugh parameters [*Schmitt et al.*, 2015] in order to separate different scattering mechanisms inherent for different features of tundra landscapes. Probability density functions were derived for Kennaugh-elements of three arctic calibration sites. Thresholds were derived depending on incidence angles and linear functions were employed in order to compensate for inconsitencies due to incidence angle variations. Results were compared to NDVI mean values and validated using field data and Sentinel-2 images. A remaining issue proved to be windy conditions, which hampered classification of water bodies.

1.4.6 Author's contribution

- **Publication I:** Conducting all data processing and analysis, designing the figures and compiling the manuscript.

- **Publication II:** Performing all data analyses, collecting moisture and vegetation information at the CALM site, designing the figures and compiling the manuscript.

- **Publication III:** Development of the concept of the study, conducting all data processing and analysis, the literature research, designing the figures and writing the majority of the manuscript.

- **Additional publication A:** Conducting all data processing and analysis, designing the figures and compiling the manuscript.

- **Additional Publication B:** Conducting the analysis and classification, designing the figures and compiling the manuscript.

1.5 Scientific impact

Following the objectives of this thesis (see section 1.2), the key findings and main scientific contributions for microwave remote sensing of arctic regions are listed below:

- It could be shown that C-band winter minimum backscatter values as well as their differences to summer minimum values reflect vegetation physiognomy units of certain wetness regimes. Winter minimum backscatter proved to be more suitable for the delineation of wetness classes in arctic tundra regions. Due to low roughness and low volume scattering of plant communities typical for wet tundra regions, arctic wetlands could be identified by their lower winter minimum backscatter values. The introduced method of using winter minimum backscatter in order to delineate wetness level classes could successfully be applied at circumpolar as well as at regional scale.

- X-band backscatter data has been for the first time demonstrated to be suitable for deriving an active-layer thickness map with an RMSE of 20 cm. The connection between active-layer thickness and X-band backscatter could be attributed to a common dependency on land cover types as well as on the interrelation of vegetation, terrain, soil moisture and snow cover. The high spatial resolution of X-band SAR data allows to address the typically high heterogeneity of tundra landscapes.

- A linear relationship between C-band winter backscatter and the incidence angle dependency of the backscatter could be established allowing the deviation of a simplified normalization approach, applicable for single scenes of non-mountainous arctic regions and reducing processing efforts. As incidence angle dependency slopes do not change for constant roughness and volume scattering, slope values derived from winter data may be applicable to normalize data independent of acquisition time. Variations due to phenology may however need to be considered.

Chapter 2

Publication I

A novel approach for the characterization of tundra wetland regions with C-band SAR satellite data

Widhalm, B.[1,2], A. Bartsch[1,2,3], and B. Heim[4]

[1] Department of Geodesy and Geoinformation, Research group Remote Sensing, Vienna University of Technology, Vienna 1040, Austria

[2] Austrian Polar Research Institute, c/o Universitt Wien, 1090 Vienna, Austria

[3] Section Climate Change Impacts, ZAMG- Zentralanstalt für Meteorologie und Geodynamik, Vienna 1190, Austria

[4] Hemholtz-Zentrum für Polar und Meeresforschung, Periglacial Research, Alfred Wegener Institute, Potsdam 14473, Germany

Abstract

A circumpolar representative and consistent wetland map is required for a range of applications ranging from upscaling of carbon fluxes and pools to climate modelling and wildlife habitat assessment. Currently available data sets lack sufficient accuracy and/or thematic detail in many regions of the Arctic. Synthetic aperture radar (SAR) data from satellites have already been shown to be suitable for wetland mapping. Envisat Advanced SAR (ASAR) provides global medium-resolution data which are examined with particular focus on spatial wetness patterns in this study. It was found that winter minimum backscatter values as well as their differences to summer minimum values reflect vegetation physiognomy units of certain wetness regimes. Low winter backscatter values are mostly found in areas vegetated by plant communities typically for wet regions in the tundra biome, due to low roughness and low volume scattering caused by the predominant vegetation. Summer to winter difference backscatter values, which in contrast to the winter values depend almost solely on soil moisture content, show expected higher values for wet regions. While the approach using difference values would seem more reasonable in order to delineate wetness patterns considering its direct link to soil moisture, it was found that a classification of winter minimum backscatter values is more applicable in tundra regions due to its better separability into wetness classes. Previous approaches for wetland detection have investigated the impact of liquid water in the soil on backscatter conditions. In this study the absence of liquid water is utilized.

Owing to a lack of comparable regional to circumpolar data with respect to thematic detail, a potential wetland map cannot directly be validated; however, one might claim the validity of such a product by comparison with vegetation maps, which hold some information on the wetness status of certain classes. It was shown that the Envisat ASAR-derived classes are related to wetland classes of conventional vegetation maps, indicating its applicability; 30% of the land area north of the treeline was identified as wetland while conventional maps recorded 1-7%.

2.1   Introduction

The representation of spatial wetness patterns is in great demand for research in Arctic environments, for example in upscaling of flux measurements, soil thermal properties assessment (heat transfer), and general soil properties (aerobic/anaerobic conditions carbon storage). Regional to global wetland products focus mostly on inundation fraction and its variation utilizing coarse-resolution (25-50 km) data sets [*Prigent et al.*, 2007; *Schroeder et al.*, 2010; *Jones et al.*, 2011]. Such data provide valuable information on seasonally waterlogged conditions and thus can be applied as a basis to estimate methane release [*Durden et al.*, 1996; *Morrissey et al.*, 1996; *Ringeval et al.*, 2010; *Watts et al.*, 2014]. Soils close to saturation (especially in peatlands) however need to be considered as well for carbon land surfaceatmosphere exchange studies [*Schneider et al.*, 2009; *Koven et al.*, 2011; *van Huissteden and Dolman*, 2012]. Microwave satellite data have been shown suitable for near-surface soil saturation retrieval (e.g. *Wagner et al.* [1999]; *Pathe et al.* [2009]; *Reschke et al.* [2012]).

Although global data sets of surface soil moisture based on satellite data do exist, their spatial resolution is relatively coarse, similar to the inundation data sets(25-50km)(e.g.*Kerr et al.* [2001]; *Njoku* [2004]; *Naeimi et al.* [2009a, b]. With heterogeneity being a major challenge in the Arctic, higher-resolution products are essential [*Högström et al.*, 2014]. It has been shown that such wetland products (<150 m) are possible when using synthetic aperture radar (SAR) data (e.g. *Bartsch et al.* [2008]), but data availability is still insufficient for spatially continuous circumpolar records to date [*Reschke et al.*, 2012; *Bartsch et al.*, 2012]. However, a comprehensive record is available from medium-resolution SAR (specifically Envisat Advanced SAR Global Monitoring mode (GM, 1 km)), which can be utilized to derive general wetness patterns for the Arctic [*Bartsch et al.*, 2009].

Wetland classes are also included in land-cover maps. However, the accuracy of land-cover products for Arctic regions, specifically classes related to wetland types, and the product utility for various applications remain largely uncertain [*Krankina et al.*, 2011]. *Pflugmacher et al.* [2011] compared coarse-resolution land cover maps like GlobCover, GLC-2000, and MODIS C4 and C5 for northern Eurasia and confirmed their low mean

agreement in the northern taiga-tundra zone.

Wetland classes typical of tundra environments are also only partially included in the widely used Global Lakes and Wetland database [*Lehner and Döll*, 2004; *Bartsch et al.*, 2008].

The purpose of this study is to explore circumpolar Envisat ASAR GM backscatter behaviour in subarctic and Arctic environments with special emphasis on spatial wetness patterns. Flux studies often distinguish between three classes: dry, mixed, and wet [*Parmentier et al.*, 2011]. Such categories can, for example, be associated with certain classes of detailed land-cover maps developed for methane flux upscaling [*Schneider et al.*, 2009].

Conventional land-cover maps are explored with respect to their C-band backscatter characteristics and wetness classes. A novel type of circumpolar wetland map based on surface scattering characteristics rather than land-cover classes is eventually proposed in order to meet the needs, in particular, of land-surface exchange upscaling studies. Such an approach may be also applicable to the data from the follow-on sensor Sentinel-1 on a regional basis but at higher spatial resolution.

2.2 Datasets

2.2.1 ASAR GM

The Advanced Synthetic Aperture Radar (ASAR) instrument on board ESA's Envisat satellite operated in C-band (5.3 GHz) in five different modes with varying temporal and spatial resolution from 30 m to 1 km, from 2002 to spring 2012. Among these, the GM formed the background mission and was active whenever no other mode had been requested. Using the ScanSAR technique, GM provided low-esolution images (1 km) with a wide swath width of 405 km and incidence angles from 15° to 45° [*ESA*, 2004]. These data became accessible from 2005. Data availability in the Arctic is high [*Bartsch et al.*, 2009] due to overlapping swaths related to the polar orbit and the low demand for higher-resolution acquisitions in these regions. All ASAR GM level 1b data used were acquired with HH-Polarization.

2.2.2   Circumpolar and regional land cover maps

Circumpolar Arctic Vegetation Map

The Circumpolar Arctic Vegetation Map (CAVM, *Walker et al.* [2002]) shows the types of vegetation that occur across the Arctic, between the ice-covered Arctic Ocean to the north and the northern limit of forests to the south. Its classes resemble vegetation communities and can be associated with the wetness levels dry, medium, and wet. It provides the source for the parameterization of the SAR-based classification approach.

A false-colour infrared image derived from biweekly 1993 and 1995 Advanced Very High Resolution Radiometer (AVHHR) data provided a base image for the interpretation of vegetation when the CAVM was developed. The approach used for making the CAVM was based on manual 'photo-interpretation' of the AVHRR satellite image mosaic. Vegetation is interpreted on the basis of 'integrated vegetation complexes' (IVC). These IVCs are derived from a combination of information from satellite-derived images and from existing source maps, such as bedrock geology, surficial geology, soils, hydrology, and previous vegetation maps. The CAVM is essentially a GIS database that uses expert knowledge of the relationship of plant communities to climate, parent material, and topographic factors to predict vegetation within landscape units that can be delineated on 1:7500-scale AVHRR images. [*Walker et al.*, 2002].

Furthermore, the *CAVM Team* [2003] identified three different moisture levels for certain vegetation physiognomic units (see Table 2.1).

Global Boreal Forest Mapping Project

A data set was produced for Alaska and Siberia within the framework of the Global Boreal Forest Mapping Project (GBFM), an initiative of the Japan Aerospace Exploration Agency (JAXA), and is based on L-band Japanese Earth Resources Satellite 1 (JERS-1) data acquired in years 1997-1998.

The GBFM Siberia data set classification covers a major part of Siberia, with special attention to wetlands, and has a resolution of 100 m. Improved classification accuracy was obtained by taking terrain features into consideration [*Kropacek and Grandi*, 2006].

The thematic map of wetlands throughout Alaska (100 m resolution) was also produced

Wetness level	CAVM class
Wet	12: Sedge/grass, moss wetland
	13: Sedge, moss, dwarf-shrub wetland
	14: Sedge, moss, low-shrub wetland
Medium	2: Rush/grass, forb, cryptogram tundra
	5: Graminoid, prostrate dwarf-shrub, forb tundra
	7: Non-tussock sedge, dwarf-shrub, moss tundra
	8: Tussock-sedge, dwarf-shrub, moss tundra
	9: Erect dwarf-shrub tundra
	10: Low-shrub tundra
Dry	1: Cryptogram, herb barren
	4: Prostrate dwarf-shrub, herb tundra
	6: Prostrate/hemiprostrate dwarf shrub tundra

Table 2.1: CAVM classes [*Walker et al.*, 2002] and wetness level categories.

using the GBFM data set. The classification was developed using the random forests decision tree algorithm with training and testing data compiled from the National Wetlands Inventory (NWI) and the Alaska Geospatial Data Clearinghouse (AGDC). The GBFM mosaics of summer and winter JERS-1 SAR imagery were employed together with other inputs and ancillary data sets [*Whitcomb et al.*, 2009].

United States Geological Survey Alaska

The United States Geological Survey (USGS) vegetation map of Alaska includes 19 vegetation classes (http://agdc.usgs.gov/data/usgs/erosafo/veg/vegetation.html) and has a resolution of 1 km. It uses the phenology of a vegetation index collected by the AVHRR during the 1991 growing season

Northern Land Cover of Canada-Circa 2000

The Northern Land Cover of Canada-Circa 2000 (NLCC, *Olthof et al.* [2009]) covers northern Canada north of the treeline and is based on medium-resolution (30 m) Landsat images which have been combined into 16 radiometrically balanced largearea mosaics. Spectral clusters were merged into 15 classes using look-up tables which were generated using existing land-cover products and limited field and additional reference data found in the literature.

Lena Delta

The Lena River Delta, situated in northern Siberia, is the largest Arctic delta and covers approximately 29,000 km^2. Remote sensing-derived regional land cover maps of the Lena Delta are publicly available from *Schneider et al.* [2009] and *Muster et al.* [2012]. Both Lena Delta data sets are derived from the same Landsat 7 ETM+ satellite data mosaic composed from cloud-free acquisitions in summer months in 2000 and 2001 at 30 m resolution. *Schneider et al.* [2009] applied supervised classification according training units taken from field descriptions and defined nine classes characterized by their vegetation, surface moisture, and topography. The map of wetness-related biome units was developed for upscaling of methane emissions. *Muster et al.* [2012] used high-spatial resolution aerial photography to develop a statistical downscaling approach to derive the surface water fraction from the Landsat reflectances. Both data sets show the spatial distribution of three main wetness regimes related to the geomorphological main terraces of the Lena Delta: wet polygonal tundra on the first terrace, dry sparsely vegetated regime of the sandy second terrace, and the medium wetness regime of the third Yedoma terrace.

2.2.3 Global maps

Global Lakes and Wetlands Database

The Global Lakes and Wetlands Database (GLWD) is based on a variety of existing maps, data, and information. Its wetlands layer contains lakes, reservoirs, rivers, and different wetland types within a global raster map at 30″ resolution [*Lehner and Döll*, 2004].

Climate Change Initiative

ESA's Climate Change Initiative (CCI) land-cover map is a global map at 300 m spatial resolution. It uses a multi-year, multi-sensor strategy and a legend based on the UN Land Cover Classification System (LCCS) [*ESA*, 2009].

2.3 Methodology

Radar backscatter is dependent on sensor parameters such as incidence angle, polarization, and wavelength, geometric parameters like surface roughness and vegetation structure, as

well as soil properties [*Ulaby et al.*, 1982]. Depicting material characteristics, the dielectric constant is highly dependent on soil moisture content, leading to higher backscatter values under wet soil conditions. In regions where mostly soil moisture contributes to the signal differences over time, wet areas can be determined by directly using backscatter values under unfrozen conditions (high-low corresponding to wet-dry, e.g. *Wagner et al.* [1999]; *Alvarez-Mozos et al.* [2005]; *Ulaby et al.* [1982]). This requires homogenous scattering within the resolution cell, which is often not the case in Arctic wetland environments (*Bartsch* [2010]; *Reschke et al.* [2012]; etc.). Especially for shorter wavelengths the penetration to the ground is limited in forests, hampering the detection of forested wetland patches. It also needs to be considered that there is a soil moisture threshold above which the saturated soil causes specular reflection leading to a decrease in radar backscatter (Henderson and Lewis 1998).

Temporal backscatter variations can be linked to soil moisture dynamics. Therefore time series-based approaches determine the location-specific dry (minimum) and wet (maximum) backscatter from time series records for unfrozen and non-snow-covered time periods to obtain the so-called dry and wet reference values [*Wagner et al.*, 1999]. By subtracting these reference images representing dry soil conditions from each radar image, surface roughness and land-cover patterns can be accounted for by change detection methods [*Moran et al.*, 2000; *Engman*, 2000].

However, in wetland areas which never dry out, this dry-reference value needs to be defined differently. In areas where freezing occurs, the frozen state backscatter can be used instead since the dielectric properties of frozen soil are similar to those of dry soil [*Duguay et al.*, 2013; *Naeimi et al.*, 2012]. In both cases no or little liquid water is present. It has been postulated by *Bartsch et al.* [2012] that a combined use of dry-reference determination approaches (historical summer minimum and frozen records) can be used to identify wetlands in subarctic and Arctic environments. A significant difference between the dry references is expected for permanent wetlands. This method is hereafter referred to as 'difference' or 'diff'.

Snow cover and especially changes in snow structure can cause backscatter increase during winter in C-band [*Naeimi et al.*, 2012]. The backscatter minimum from Envisat ASAR

GM under frozen conditions is therefore investigated for the month of December, which corresponds to the frozen period, and the impact of snow cover is considered to remain limited.

Arctic tundra regions are characterized by abundant lakes below the limits of GM resolution. This reduces the backscatter in summer and late winter when lakes freeze to the ground [*Duguay and Lafleur*, 2003]. It can be therefore assumed that the difference between summer and December is partially reduced in the case of a significant water fraction within the resolution cell. An alternative approach which utilizes only the December records is therefore now investigated.

For the required preprocessing of the Envisat ASAR GM level 1b data, the SAR Geophysical Retrieval Toolbox (SGRT, Vienna University of Technology, *Sabel et al.* [2012]) was used. This is a collection of routines which manages SAR geocoding and radiometric calibration by calling other non-commercial and commercial software packages. By incorporating orbit information (DORIS (Doppler Orbitography and Radiopositioning Integrated by Satellite) orbit files) and digital elevation data (Shuttle Radar Topography Mission-improved U.S. Geological Survey GTOPO30 digital elevation model), othorectified images were produced at sub-pixel accuracy [*Park et al.*, 2011; *Pathe et al.*, 2009], depicting the backscatter coefficient σ_0 in dB. Resampling the data into a fixed 15 arc-seconds grid (datum WGS-84), within 0.5° by 0.5° tiles, further allowed efficient spatial and temporal analysis, designed for global processing. To remove the influence of local incidence angle on radar backscatter, the data (>8000 scenes north of 60° N) were normalized to a reference angle of 30° by fitting a linear model to the backscatter data [*Pathe et al.*, 2009; *Sabel et al.*, 2012, 2007]. Dry-reference maps were calculated from Envisat ASAR GM data for summer (July and August, hereafter referred to as $\sigma_{0,\,\mathrm{smin}}$) and winter (December, hereafter referred to as $\sigma_{0,\,\mathrm{wmin}}$) of the years 2005-2011, representing the minimum backscatter values of this timespan. $\sigma_{0,\,\mathrm{smin}}$ can be seen as conditions of minimum soil moisture and therefore driest summer conditions, while $\sigma_{0,\,\mathrm{wmin}}$ represents frozen conditions, which appear similar to dry conditions. December data are expected to show limited liquid water content and low impact by snow cover.

It is expected that regions with higher soil moisture exhibit higher backscatter and a

greater decline in backscatter values in winter caused by freezing related to the drop in the dielectric constant. Therefore it is assumed that the difference between summer and winter dry reference is higher for wet regions than for dry ones.

Mean and median values, as well as standard deviation for vegetation classes of the circumpolar CAVM, were calculated for $\sigma_{0,\ wmin}$, $\sigma_{0,\ smin}$, and the difference between $\sigma_{0,\ wmin}$ and $\sigma_{0,\ smin}$ ($\sigma_{0,\ diff} = \sigma_{0,\ wmin}$ - $\sigma_{0,\ smin}$) (see Figure 1). At this stage no masking of areas with high water fraction was applied for the circumpolar assessment.

The CAVM is the only circumpolar product with adequate thematic detail. Its moisture information, which can be assigned to several classes, was used in order to investigate the ASAR GM-derived backscatter in relation to wetness classes. In addition, the more detailed wetland map of *Schneider et al.* [2009] was used to evaluate and refine the backscatter stratification over the Lena Delta.

In the derived wetness level product, a mask for open water and glaciers was applied based on the map classes of GLWD [*Lehner and Döll*, 2004] and GlobCover, [*Bicheron et al.*, 2008], which is an ESA land-cover map based on Medium Resolution Imaging Spectrometer (MERIS), 300 m) sensor observations. All these data sets do not, however, completely capture open water bodies in the Arctic [*Bartsch et al.*, 2008; *Muster et al.*, 2013]. An adequate circumpolar land-cover map is, to date, not available. The impact is discussed below.

Regions with backscatter ranges which can be associated with the wetness classes (as seen in Table 2.1) are compared to the conventional land-cover data sets listed in section 2.2.2. Due to a lack of comparable data sets, the derived wetness level map was compared to land-cover maps containing classes of wetlands.

2.4   Results

2.4.1   Backscatter analysis

The analysis of backscatter statistics for CAVM classes showed that for both $\sigma_{0,\ wmin}$ and $\sigma_{0,\ smin}$, barren and sparsely vegetated areas exhibit highest backscatter values, followed by plant communities considered as dry (Figure 2.1). Vegetation community classes which can be found in moist areas showed lower backscatter values, with even lower values
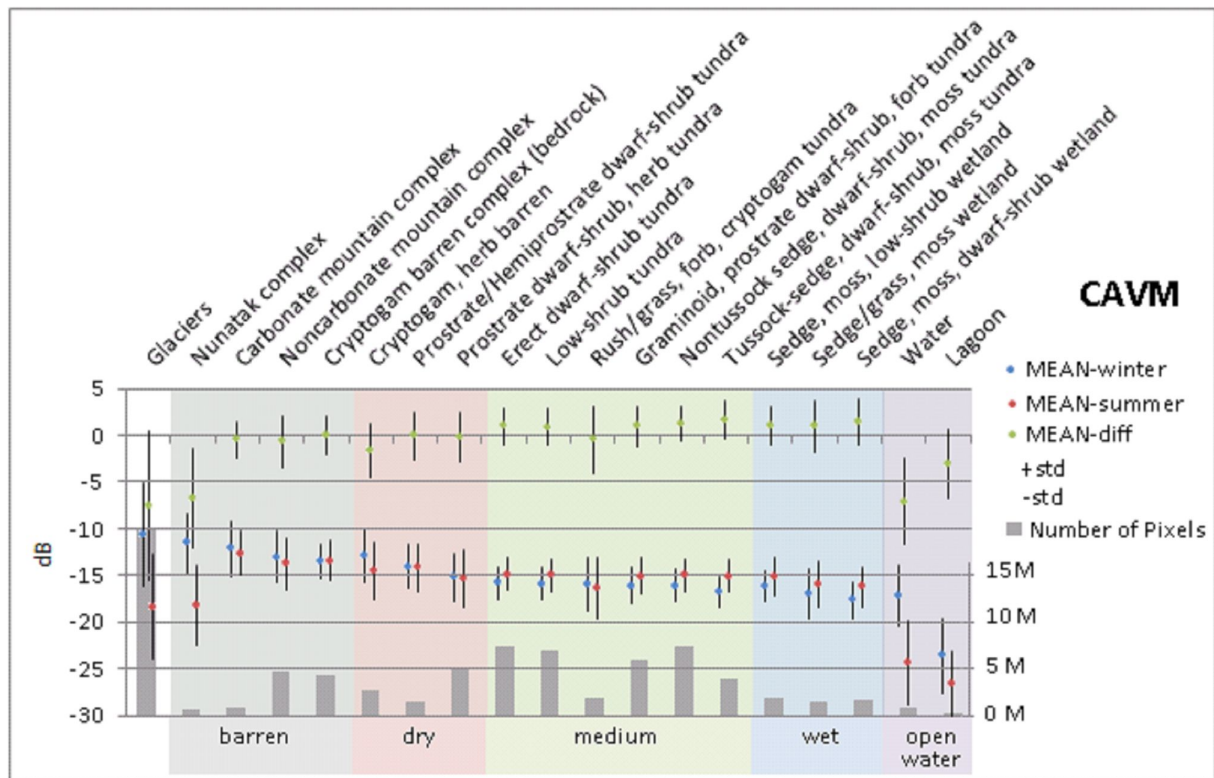
Figure 2.1: Mean values and standard deviations of $\sigma_{0,\,wmin}$, $\sigma_{0,\,smin}$, and $\sigma_{0,\,diff}$ (= $\sigma_{0,\,wmin}$ - $\sigma_{0,\,smin}$) for CAVM classes ordered by wetness (grey: barren, mountainous; red: dry; green: medium; blue: wet; violet: open water).

being encountered in wet areas and minimum values for open water bodies. The effect of roughness and volume scattering may thus be lower for wetter areas than for dry. Subpixel-size water bodies play an essential role in this environment and contribute to a reduction in backscatter in summer and increase in early winter.

In the $\sigma_{0,\,diff}$ product, negative values were found for barren areas and open water bodies; values increased from dry to wetter areas. Figure 2.1 shows that the wetter classes of the vegetation complexes of the CAVM (Table 2.1) show higher summerwinter differences than drier classes. This supports the hypothesis of *Bartsch et al.* [2012] that wetlands in this biome do not dry out in summer and can be therefore distinguished from other land cover when the expected backscatter value for dry conditions is known.

As apparent from Figure 2.2, $\sigma_{0,\,diff}$ values for the wet and medium CAVM classes overlap, preventing a feasible separation of these classes within a potential wetness level product. Only $\sigma_{0,\,wmin}$ is therefore further used for extraction of wetness level maps (Figure 2.3). The mean between CAVM median backscatter values for each wetness level was used to
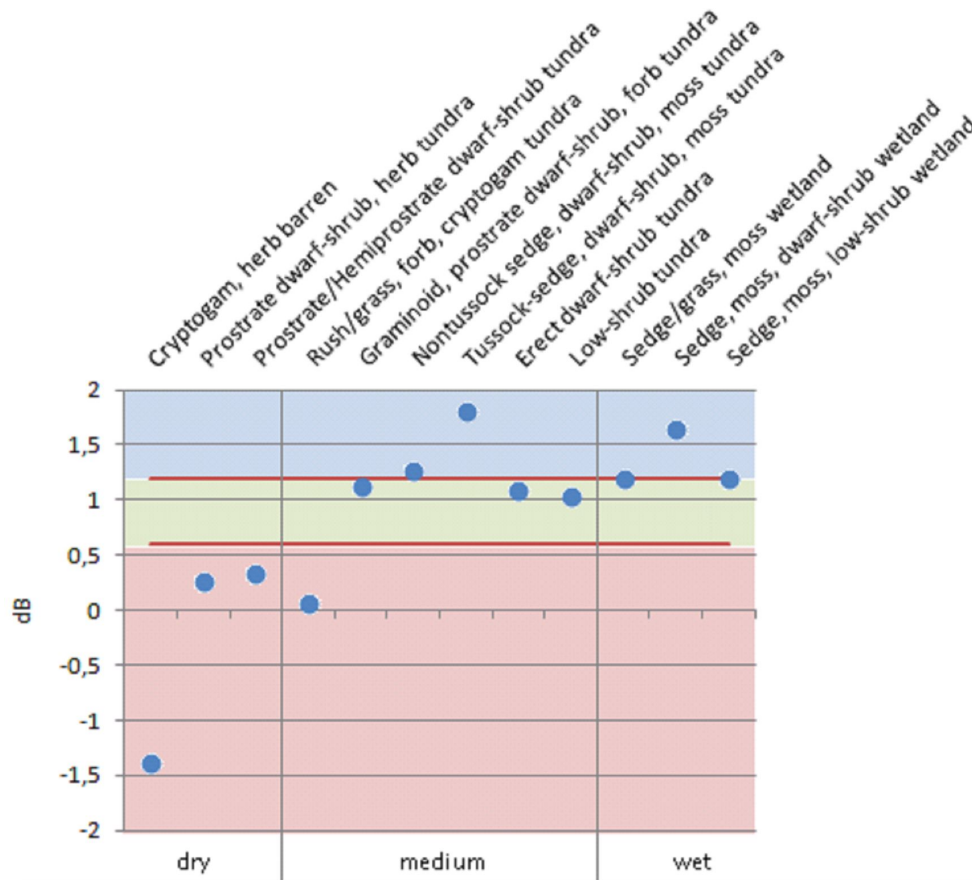
Figure 2.2: Median $\sigma_{0,\text{ diff}}$ values for dry, medium, and wet CAVM classes. Red lines indicate the chosen thresholds of 0.6 and 1.2 dB (red: dry; green: medium; blue: wet).

set the thresholds to -15.2 and -16.5 dB. The median was used here instead of the mean due to its robustness concerning outliers. Figure 2.4 shows the resulting classes based on $\sigma_{0,\text{ wmin}}$.

A comparison with the medium-resolution (30 m) land cover map of the Lena Delta [*Schneider et al.*, 2009] (Figure 2.5), as well as the global CCI Landcover product, was carried out as a first assessment step. It showed that the wetness level map reveals more detail than the global map but does not support the identification of the northern terrace which is characterized as 'dry moss-, sedge-, and dwarf shrub-dominated tundra' and comparably dry. With distinction of three wetness levels it is classified as wet. The comparison with $\sigma_{0,\text{ wmin}}$ (Figure 2.6) reveals that this area is characterized by even lower values. An additional class (class 'other') was therefore introduced in order to distinguish such open areas (sandbanks and flat sandy soils) as characteristic of a range of locations
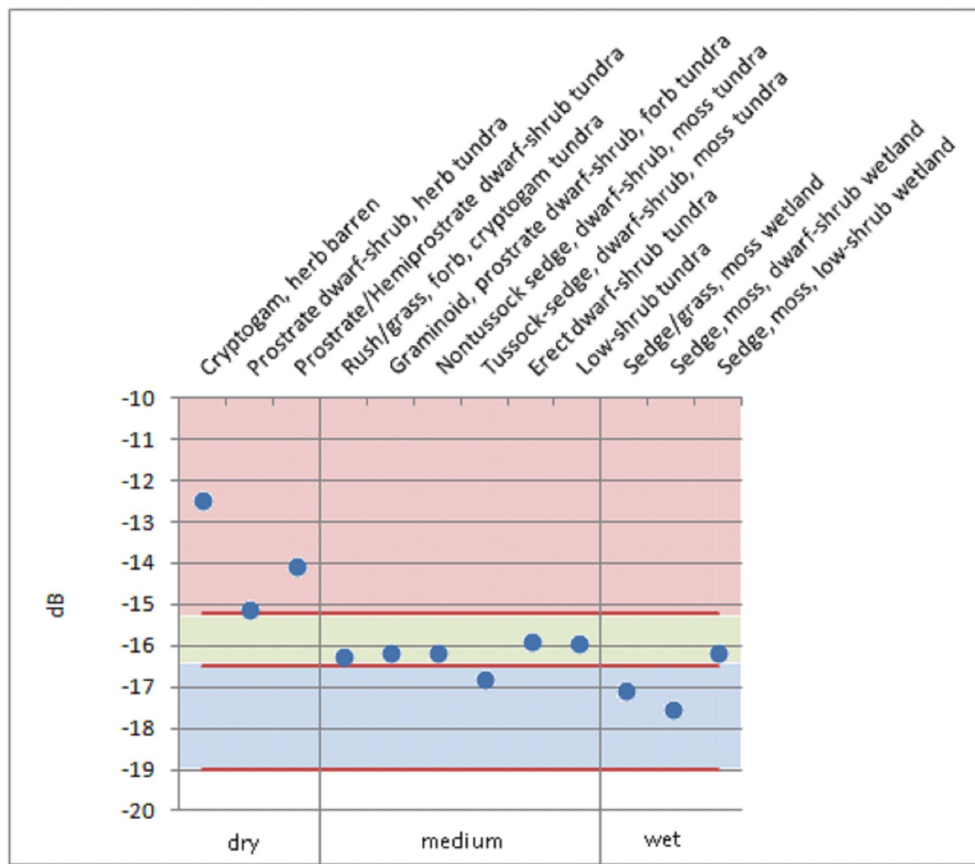
Figure 2.3: Median $\sigma_{0,\,\text{wmin}}$ values for dry, medium and wet CAVM classes. Red lines indicate the chosen thresholds of -15.2, -16.5, and -19 dB (red: dry; green: medium; blue: wet).

along Arctic coasts. The threshold for this class was set to -19 dB in $\sigma_{0,\,\text{wmin}}$ to match the conditions in the field.

In the following the stratified map and its classes are referred to as wetness level map (WL map) and wetness level classes (WL classes), respectively.

2.4.2 Comparison with conventional land cover

To evaluate the WL map, the fraction of WL classes within each class of the used land-cover maps was assessed. For this purpose the land-cover maps were kept at their original resolution.

GBFM Siberia

Comparison with the map GBFM Siberia showed that classes where the fraction of wet WL class pixels dominated are in fact to be considered as wet ('bogs', 'shallow water',
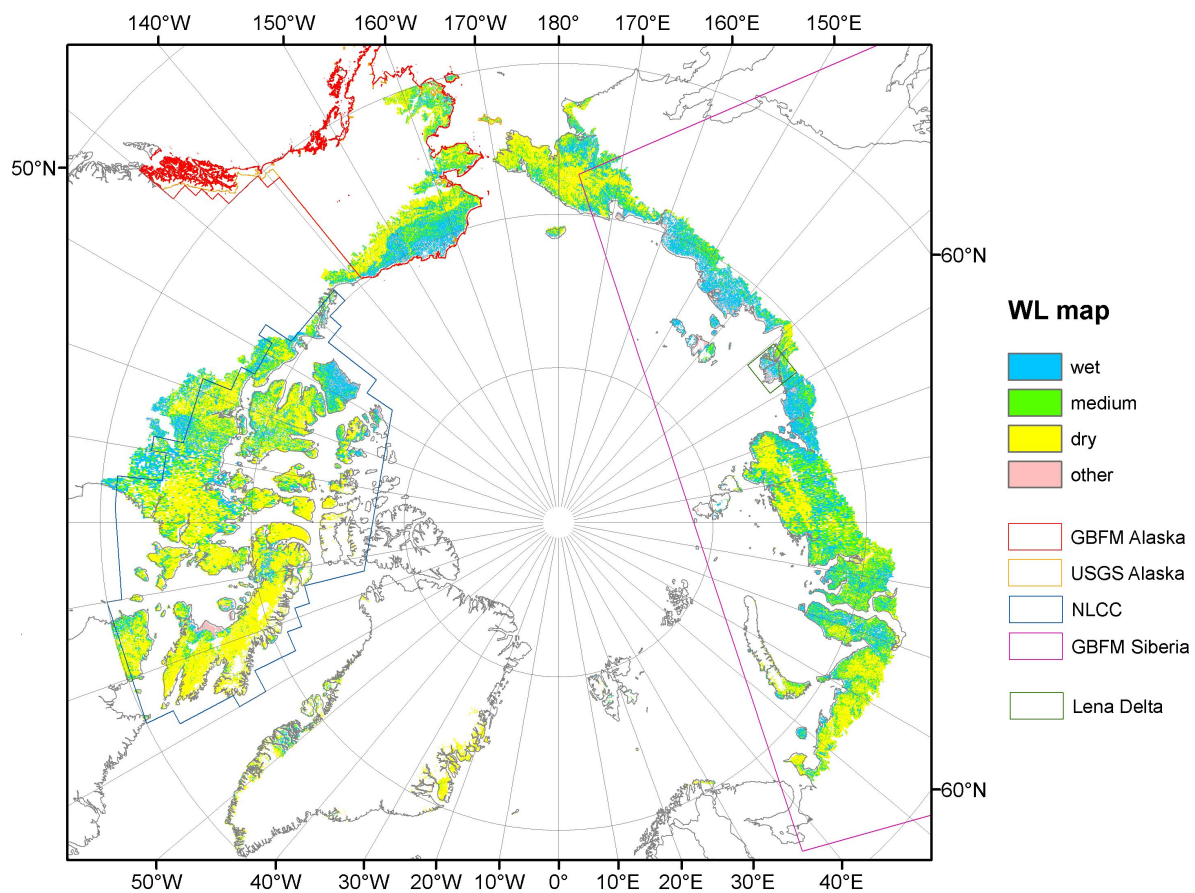
Figure 2.4: Wetness level map and outlines of the vegetation maps used for evaluation.

'water', Figure 2.7). Although the investigated area is situated north of the treeline as defined in the CAVM, a major portion of the GBFM Siberia map is classified as forest within this region. The class 'low biomass forest' shows similar fractions of wet, medium, and dry WL pixels and can be assumed to be medium class.

Even though the percentage of wet GBFM classes is considerably high within the dry WL class, the fraction increases for the medium and wet WL classes (Figure 2.8).

GBFM Alaska

For the GBFM Alaskan wetland map not all wetland classes were dominated by wet WL pixels, but those covering the largest areas were still mostly classified correctly (Figure 2.9). Therefore the wet WL map layer also consisted of more than its half of wetland classes, while in the dry WL class the class 'uplands' was predominant (Figure 2.10).

USGS Alaska

The USGS Alaskan vegetation map mostly corresponds to the WL map (Figures 2.11 and 2.2). Taking the classes 'wet sedge tundra' and 'moist herbaceous/shrub tundra' as wet and the class 'tussock sedge/dwarf shrub tundra' as medium, the WL classes are dominated by their respective vegetation classes. Furthermore, wet vegetation classes show the highest fractions of wet WL pixels. The fact that the water class shows higher fractions of dry WL pixels is expected, underlining that water can exhibit somewhat variable backscatter values depending on its freezing status, and should eventually be masked out.

NLCC

For the NLCC map only the classes 'wet sedge' and 'tussock graminoid tundra' featured a higher content of wet WL pixels, while the class 'wetland' was dominated by dry WL pixels (Figure 2.13). Nevertheless, the wet WL class still showed more definite wet NLCC classes than the dry WL layer (Figure 2.14).

Comparison with global maps

Table 2.2 shows a comparison of wetland extents derived from the WL map, GLWD, and the CCI land cover map. The wetland area was extracted as a percentage of the total area above the treeline and above 60° N. All maps were divided into western and eastern parts at 10° W, since the GLWD is based on a variety of existing maps, data, and information, and therefore show considerable dependency on their sources. The thematic detail shows specific discrepancies between Russia and North America [*Lehner and Döll*, 2004]. In North America three classes of fractional wetlands are available: '50-100% wetland', '25-50% wetland', and 'wetland complex (0-25% wetland)'. For the calculation of the wetland area of these classes the values used were, however, not reduced according to their fractional coverage, but set to 100%. This led to a wetland proportion of 7% for the western part of the GLWD, greatly exceeding the value found for the CCI land-cover product, which only accounts for 1% wetlands; however, the area covered by the 'wet' WL class identifies 11% of the total area as wetlands. If the medium WL class is also included, 21% is obtained.

Source	Classes	% wetland of total area (above 60°N and above treeline) [%]	
		West	East
GLWD	Freshwater marsh	7	5
	Coastal wetland		
	Bog, fen, mire		
	Intermittent wetland		
	50-100% wetland		
	25-50% wetland		
CCI	Shrub or herbaceous cover, flooded, fresh/saline/bracklish water	1	3
WL map	Wet	11	30
	Wet	21	54
	Medium		

Table 2.2: Comparison of wetland fraction of various sources (GLWD [*Lehner and Döll*, 2004], CCI [*ESA*, 2009], Wetness Level map) divided into eastern and western parts at 10° W.

For the eastern part, the wetland coverage of the GLWD is again higher than that of the CCI land cover (5 vs. 3%), but not nearly as high as the coverage of the 'wet' WL class. It identifies 30% of the total area as wetland and, by including the WL class 'medium', a percentage of 54 is obtained.

2.5   Discussion

Although backscatter values increase with soil moisture, the above results show that soil moisture in areas expected to be permanently wet does not have a crucial influence on backscatter values in Arctic regions. As in winter, summer values decrease for wetter areas. As winter values can be comparable to dry summer conditions, it can be assumed that the main influence lies within the roughness and volume scattering within the vegetation, which seems to decrease for land-cover types found in wetter regions. By investigating the difference between summer and winter minimum backscatter $\sigma_{0,\,\mathrm{diff}}$, it can be shown that wet regions show higher values resulting from a greater difference in dielectric constants. However, the derivation of WLs was shown to be more feasible using the $\sigma_{0,\,\mathrm{wmin}}$ values than $\sigma_{0,\,\mathrm{diff}}$. Due to an overlap $\sigma_{0,\,\mathrm{diff}}$ values of the wet and medium CAVM classes, their separation within a $\sigma_{0,\,\mathrm{diff}}$-delineated WL map could not be provided.

The reason why the application of $\sigma_{0,\text{diff}}$ values for moisture level retrieval was not particularly successful may be due to the fact that wetland-dominated pixels mostly did not show the expected higher values in summer resulting from permanently high soil moisture content. In fact they often exhibited lower winter-like values than other areas, similar to winter conditions. Similar findings were also reported for the L-band-derived Siberian GBFM mosaic. *Kropacek and Grandi* [2006] attributed this to the low biomass present in wetlands and specular reflection on the wet soil underneath, which behaves like a smooth surface. Although the roughness of a surface is dependent on the wavelength used, these findings for the L-band mosaic may also apply to C-band data. Furthermore, it can be expected that less than the entire resolution cell (1 km) is characterized by permanently saturated conditions. Small lakes are characteristic of tundra wetlands and reduce the backscatter [*Bartsch et al.*, 2008; *Muster et al.*, 2013]. In addition, C-band backscatter only represents the upper few centimetres and thus represents the fast-drying organic layer on top of the soil.

To date no comparable data set exists that can be used for validation of a WL product. It was nevertheless assessed with circumpolar and regional land-cover maps which identify some classes which can be expected to show wet or moist conditions. These comparisons showed that most wet land-cover classes exhibited higher fractions of wet WL pixels. The class 'medium' may be defined and labelled differently in different products. For instance, in methane flux studies *Parmentier et al.* [2011] used a 'mixed' class and for the CAVM the middle soil moisture class was labelled as 'moist'. Because the land-cover maps used did not define WL classes, this presented the problem of identifying land-cover classes of the medium WL class. However, in comparison with the underlying CAVM and assuming that 'tussock' classes found elsewhere also represented medium values, it was found that these vegetation classes often showed similar fractions of wet, medium, and dry WL pixels. Examination of the fractions of vegetation classes within the WL classes confirmed that $\sigma_{0,\text{wmin}}$ can be associated with wetland classes. Though the corresponding classes may not always dominate within the respective WL layer, which may be enhanced due to when maps do not show a certain wetness level, it nevertheless became clear that wet vegetation classes had higher percentages within the wet WL class than in the dry one and vice versa.

The only map that was designated to show wetlands was the GBFM thematic map for Alaska. Here wetland areas predominated in the wet WL class, while in the dry WL class the 'uplands' class, considered as dry, was dominant. Similar results were obtained for the USGS vegetation map of the same area.

The WL class 'other' was introduced in order to address discrepancies found in comparison with the vegetation map of the Lena Delta [*Schneider et al.*, 2009]. The data set of *Muster et al.* [2012] shows that this area of the Lena Delta coincides with very low water fraction values, so that the influence of small water bodies can be excluded. The WL class 'other' represents only a small proportion of the final WL map (4%). It is characterized by very low backscatter, which occurs at very flat surfaces. Sandy soils (e.g. coastal areas) are therefore included in this class. Examples of this class can be found at Bunge Land on the Anzhu Islands in Russia or the northern part of the Russian Ayon Islands, which are characterized by sandy coastal areas. The Dewey Soper Bird Sanctuary on the western Baffin Islands in Canada consists of a large proportion of the WL class 'other'. According to the Annotated Ramsar List of Wetlands of International Importance - CANADA (http://www.ramsar.org/countries/canada?page = 5), it is 'an intertidal zone with a series of raised beaches and a marshy plain of mosses and sedges, dotted with shallow lakes and swamps, drained by many small, slow-flowing streams'. There are numerous comparable small patches of the WL class 'other' on the North Slope (Alaska) and around Kytalik (eastern Siberia), which can be matched to river beds and recently drained lakes.

In this context also, the characteristics of open water areas need to be discussed. In cases where open water fails to be masked out it is expected that the WL map will often show dry values due to high winter backscattering values. While frozen rivers mostly exhibit higher backscatter due to rough surfaces resulting from river ice that has been deformed, lakes can show high values due to double-bounce reflection off tubular bubbles and the icewater interface, which has a strong dielectric contrast (e.g. *Jeffries et al.* [1996]). Where the ice is frozen to the ground, low backscatter occurs because of the low dielectric contrast between ice and the underlying sediments, in which the signal is lost. Since only December data were used, the percentage of lakes that freeze to the ground is considered to be minimal and only occurs in shallow lakes [*Jeffries et al.*, 1996; *Duguay and Lafleur*, 2003;

Surdu et al., 2014]. Other effects that can lead to lower backscatter on ice are a smooth airice surface or an insufficient number of tubular bubbles [*Jeffries et al.*, 2013].

Since land-cover heterogeneity plays an important role in Arctic areas, ASAR Wide Swath as well as its follow-on sensor Sentinel-1 data provide the opportunity of improvement regarding its higher resolution (150 m). However, this data set is not as abundant in this area and does not provide the same density in its time series as the GM data set.

2.6 Conclusions

Despite a current need for a representation of spatial wetness patterns in Arctic regions, there are to date no satisfactory circumpolar products. This study demonstrated an easy way to use C-band SAR data in order to derive a circumpolar wetness classification map. By analysing minimum winter and summer backscatter values of Arctic vegetation, dependencies on the vegetation's wetness regime became apparent, allowing a simple hierarchical classification approach. A comparison with land-cover maps indicated the applicability of the WL map, which in consideration of the new C-band Sentinel-1 mission presents further capabilities.

Acknowledgements
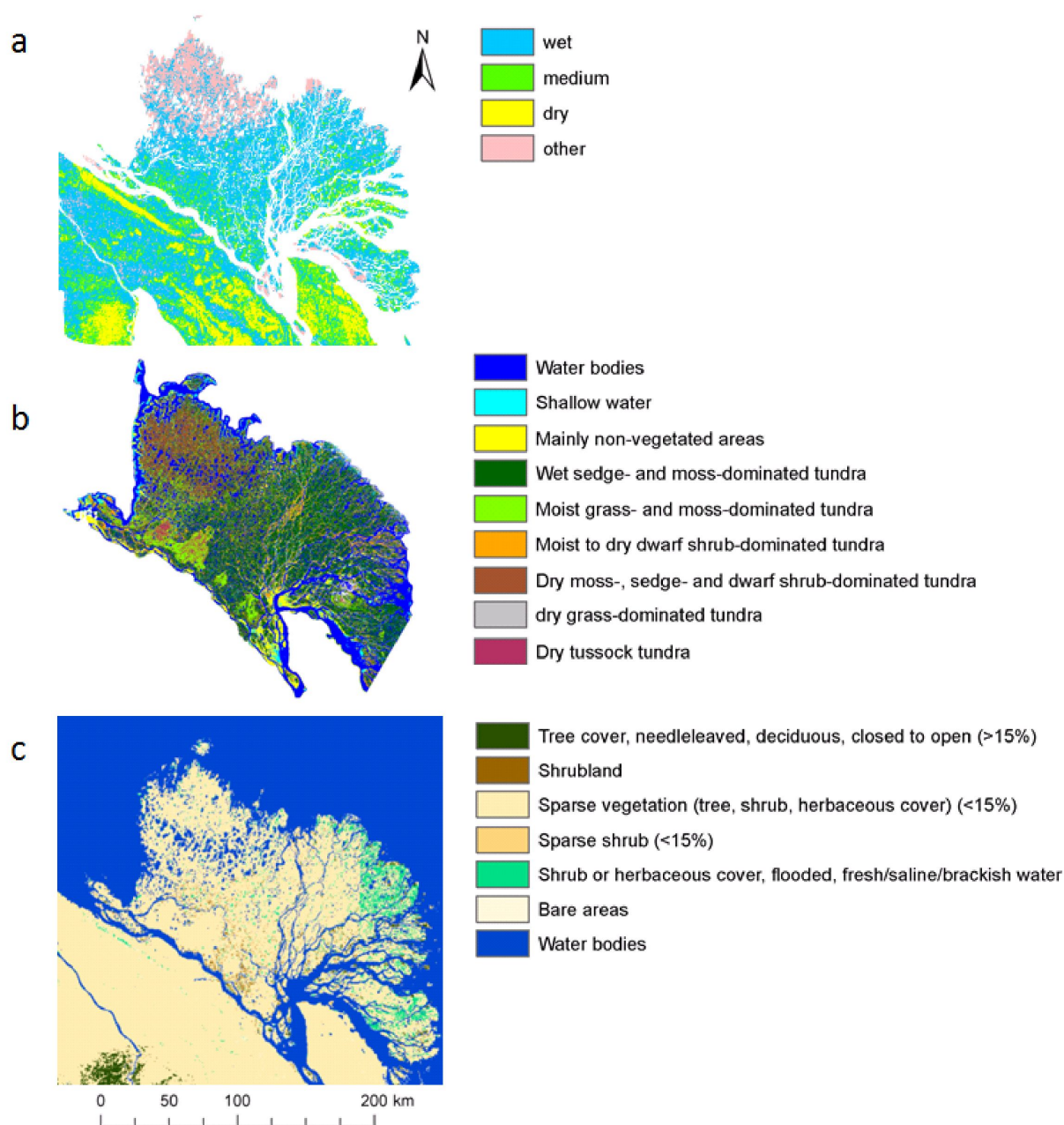
Figure 2.5: Comparison of the wetness level map (a) with the land-cover map of the Lena Delta (b, *Schneider et al.* [2009] and the CCI land cover map (c, *ESA* [2009]).
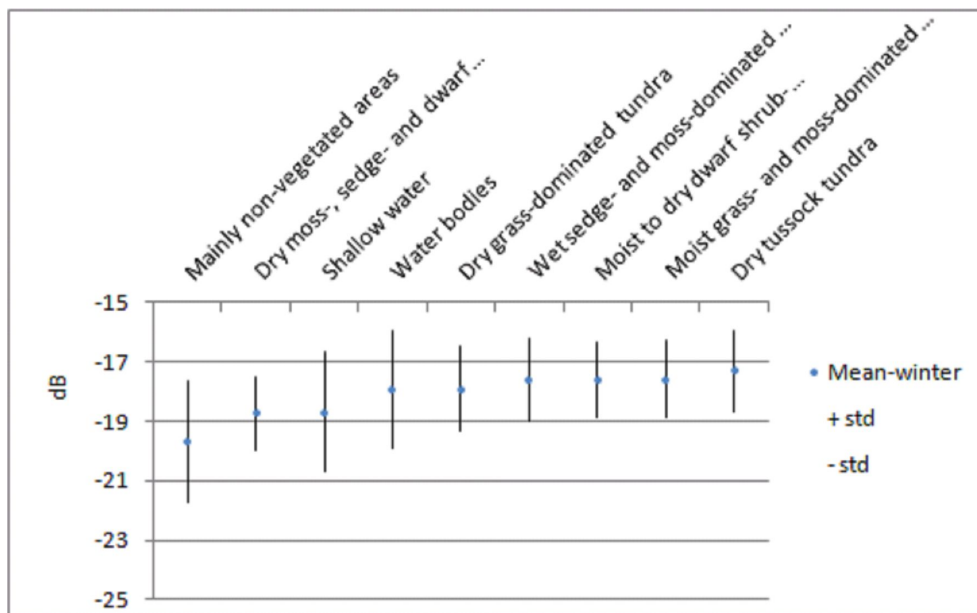
Figure 2.6: Mean values and standard deviations of $\sigma_{0,\text{wmin}}$ for the classes of the land-cover map of the Lena Delta by *Schneider et al.* [2009] (for complete class names see Figure 2.5).
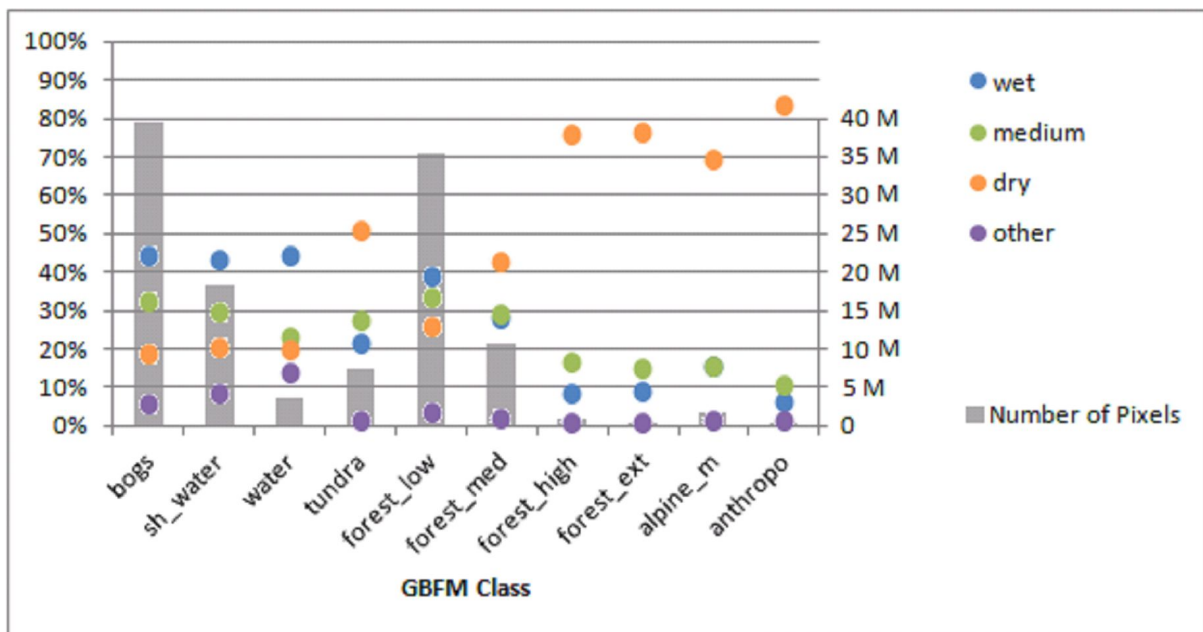
Figure 2.7: Percentage of wetness level class pixels within GBFM Siberia classes.
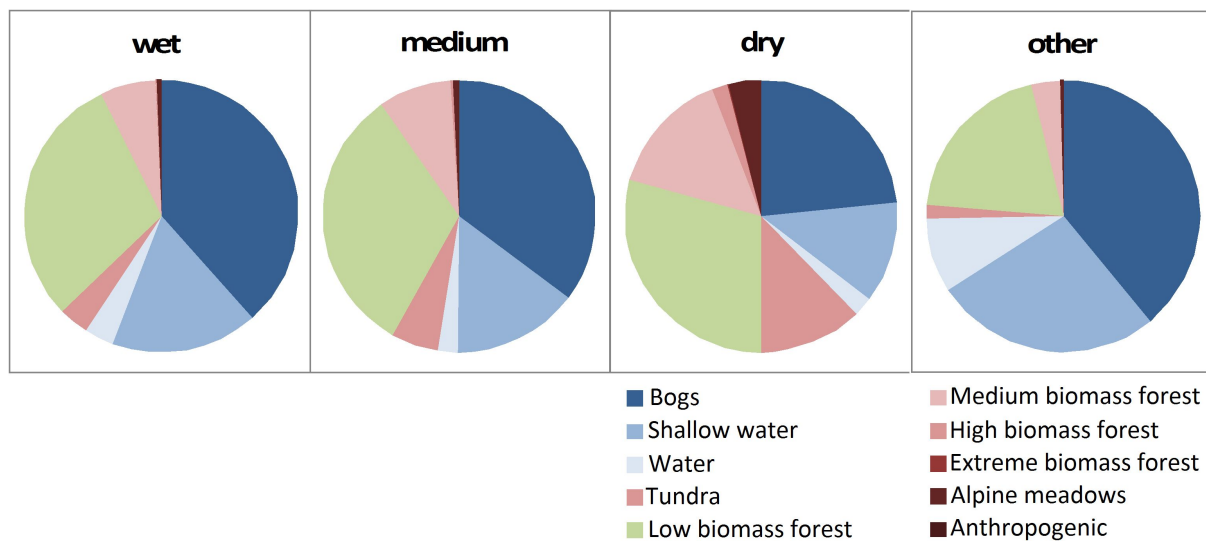
Figure 2.8: Percentage of GBFM Siberia class pixels within wetness level classes.
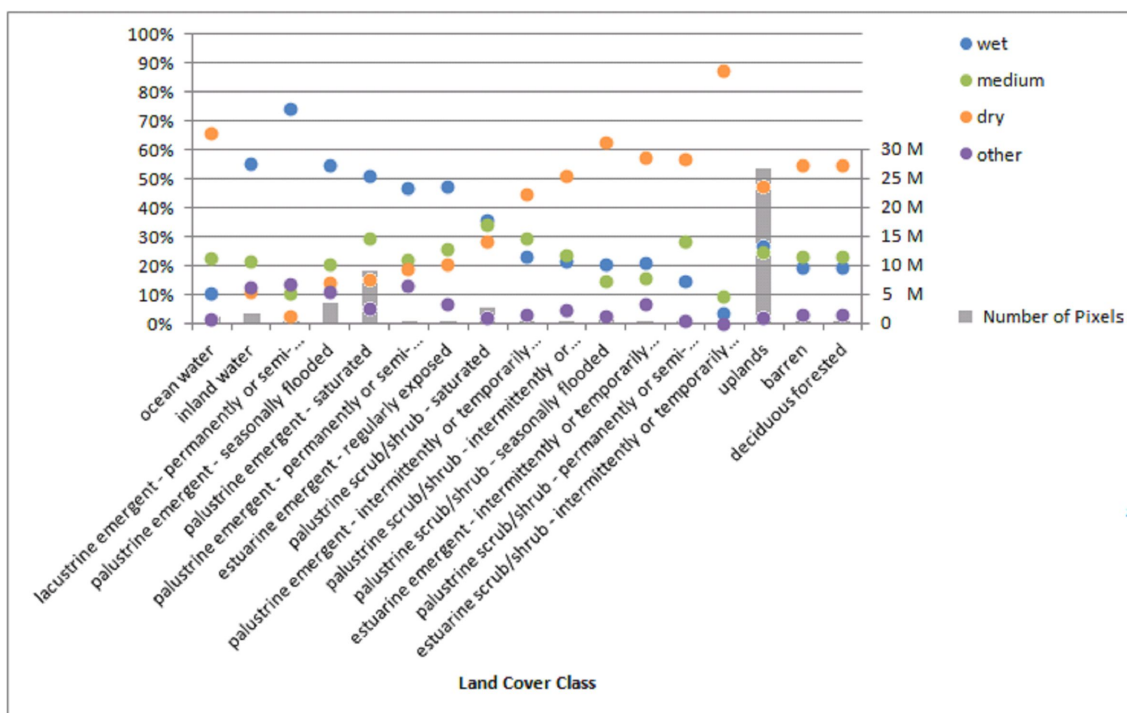
Figure 2.9: Percentage of wetness level class pixels within GBFM Alaska classes (for complete class names see Figure 2.10).

- ■ ocean water
- ■ inland water
- ■ lacustrine emergent - permanently or semi-permanently flooded
- ■ palustrine emergent - seasonally flooded
- ■ palustrine emergent - saturated
- ■ palustrine emergent - permanently or semi-permanently flooded
- ■ estuarine emergent - regularly exposed
- ■ palustrine scrub/shrub - saturated
- ■ palustrine emergent - intermittently or temporarily flooded
- ■ palustrine scrub/shrub - intermittently or temporarily flooded
- ■ palustrine scrub/shrub - seasonally flooded
- ■ estuarine emergent - intermittently or temporarily flooded
- ■ palustrine scrub/shrub - permanently or semi-permanently flooded
- ■ estuarine scrub/shrub - intermittently or temporarily flooded
- ■ uplands
- ■ barren
- ■ deciduous forested

Figure 2.10: Percentage of GBFM Alaska class pixels within wetness level classes.
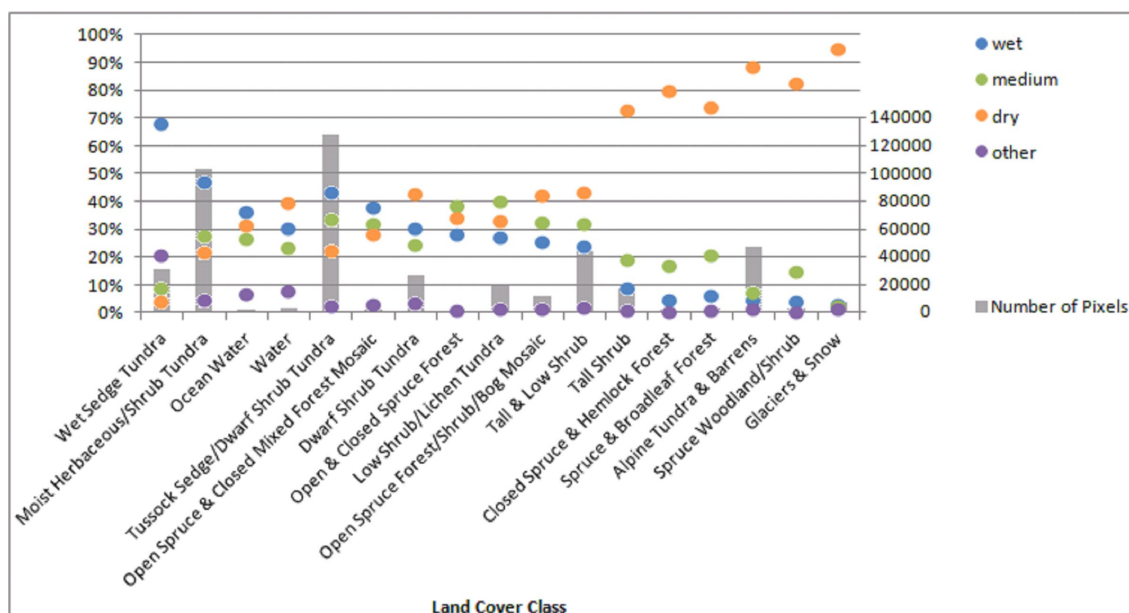
Figure 2.11: Percentage of wetness level class pixels within the (USGS) vegetation map of Alaska classes.

wet   **medium**   **dry**   **other**

- ■ Wet Sedge Tundra
- ■ Moist Herbaceous/Shrub Tundra
- ■ Ocean Water
- ■ Water
- ■ Tussock Sedge/Dwarf Shrub Tundra
- ■ Open Spruce & Closed Mixed Forest Mosaic
- ■ Dwarf Shrub Tundra
- ■ Open & Closed Spruce Forest
- ■ Low Shrub/Lichen Tundra

- ■ Open Spruce Forest/Shrub/Bog Mosaic
- ■ Tall & Low Shrub
- ■ Tall Shrub
- ■ Closed Spruce & Hemlock Forest
- ■ Spruce & Broadleaf Forest
- ■ Alpine Tundra & Barrens
- ■ Spruce Woodland/Shrub
- ■ Glaciers & Snow

Figure 2.12: Percentage of (USGS) vegetation map of Alaska class pixels within wetness level classes.
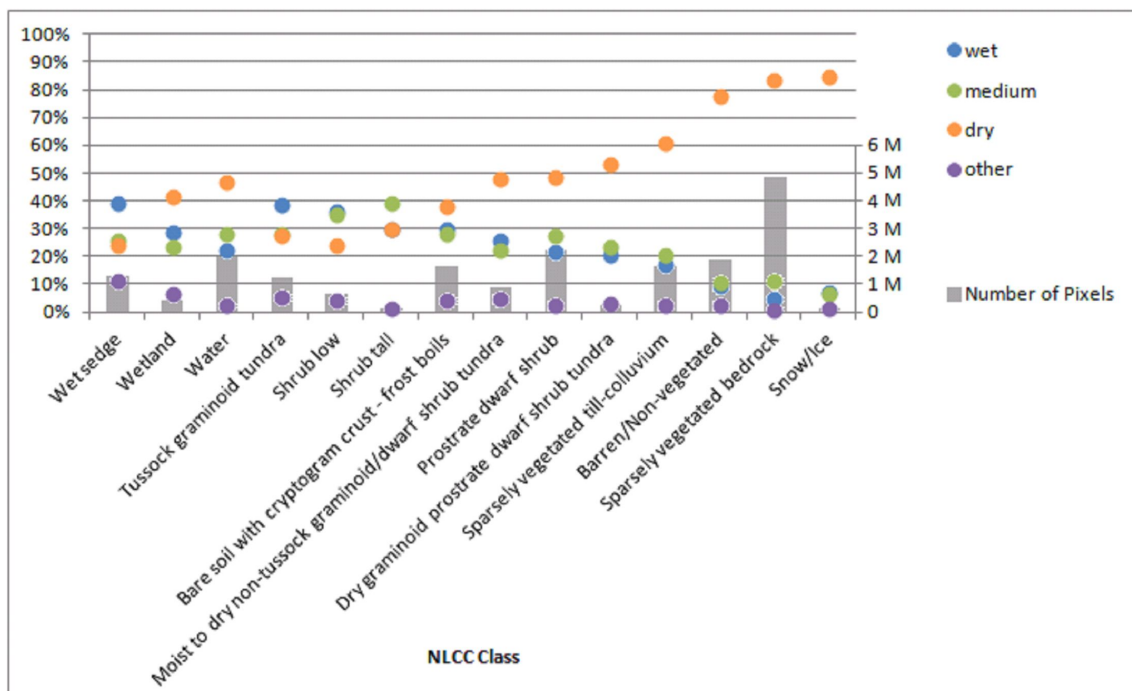
Figure 2.13: Percentage of wetness level class pixels within the NLCC classes.
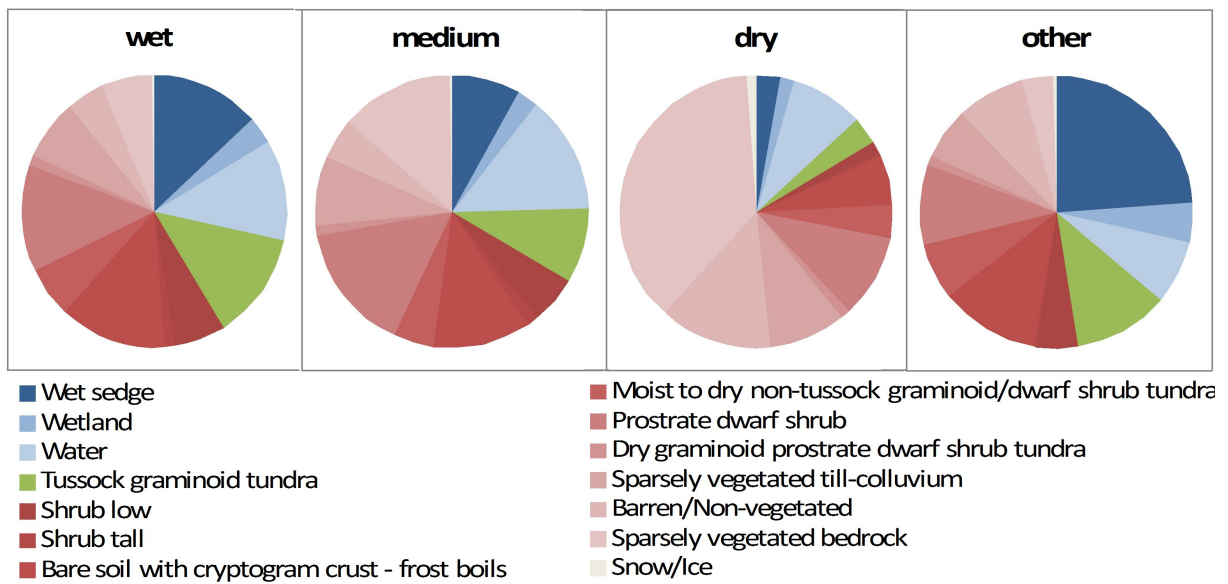
Figure 2.14: Percentage of NLCC class pixels within wetness level classes.

Chapter 3

Publication II

Active-layer thickness estimation from X-band SAR backscatter intensity

Widhalm, B.[1], A. Bartsch[1,2], M. Leibman[3,4], and A. Khomutov[3,4]

[1] Zentralanstalt für Meteorologie und Geodynamik, Division Data, Methods and Modelling, 1190 Vienna, Austria

[2] Vienna University of Technology, Department of Geodesy and Geoinformation, 1040 Vienna, Austria

[3] Earth Cryosphere Institute, Russian Academy of Sciences, Siberian Branch, Tyumen 625000, Russia

[4] Tyumen State University, Department of Cryosophy, Tyumen 625006, Russia

Abstract

The active layer above the permafrost, which seasonally thaws during summer is an important parameter for monitoring the state of permafrost. Its thickness is typically measured locally, but a range of methods, which utilize information from satellite data, exist. Mostly, the Normalized Difference Vegetation Index (NDVI) obtained from optical satellite data is used as proxy. The applicability has been demonstrated mostly for shallow depths of Active Layer Thickness (ALT) below approximately 70 cm. Some permafrost areas including central Yamal are, however, characterized by larger ALT. Surface properties including vegetation structure are also represented by microwave backscatter intensity. So far, the potential of such data for estimating ALT has not been explored. We therefore investigated the relationship between ALT and X-Band SAR backscatter of TerraSAR-X (averages for 10 x 10 m window) in order to examine the possibility of delineating ALT on a continuous and larger spatial coverage in this area and compare it to the already established method of using NDVI from Landsat (30 m). Our results show that the mutual dependency of ALT and TerraSAR-X backscatter on land cover types suggests a connection of both parameters. A range of 5 dB can be observed for an ALT range of 100 cm (40 - 140 cm) and an R^2 of 0.66 has been determined over the calibration sites. An increase of ALT with increasing backscatter can be determined. The RMSE over a comparably heterogeneous validation site with maximum ALT of >150 cm is 20 cm. Deviations are larger for measurement locations with mixed vegetation types (especially partial coverage by cryptogam crust) with respect to the spatial resolution of the satellite data.

3.1 Introduction

Permafrost is defined as soil or rock that remains at or below 0°C for two or more consecutive years [*Harris et al.*, 1988] and currently underlies some 25 % of the Earth's land surface [*Huggett*, 2007]. Due to global warming extensive areas where permafrost is presently within a degree or two below the melting point could be destabilized [*Smith*, 1990]. At global scale, increased ground temperatures could facilitate further climatic changes by releasing greenhouse gases that are currently sequestered in the upper layer of

permafrost by increasing the annual thaw depth [*Kane et al.*, 1991; *Gomersall and Hinkel*, 2001; *Shiklomanov and Nelson*, 1999; *Schaefer et al.*, 2011; *Schuur et al.*, 2015]. The top layer of ground subject to annual thawing and freezing in areas underlain by permafrost is defined as the active layer [*Permafrost Subcommittee, Associate Committee on Geotechnical Research*, 1988]. In this layer most ecological, hydrological and biochemical activities take place [*Kane et al.*, 1991; *Brown et al.*, 2000]. Furthermore it is an essential climate variable to monitor permafrost regions [*Schaefer et al.*, 2015], making it not only an important factor at regional but also global scale. The active layer thickness (ALT) is predominately controlled by ambient temperature, but is also influenced by insulation layers such as snow cover and vegetation, slope, drainage, soil type, organic layer thickness and water content [*Leibman*, 1998; *Shiklomanov and Nelson*, 1999; *Hinkel and Nelson*, 2003; *Kelley et al.*, 2004; *Melnikov et al.*, 2004; *Vasiliev et al.*, 2008]. Due to the interaction between these surface and subsurface factors that can be spatially highly variable, ALT may vary substantially over short lateral distances [*Shiklomanov and Nelson*, 1999; *Leibman et al.*, 2012].

Near-surface permafrost area is projected to decrease within the next century [*IPCC*, 2013]. Changes in active layer thickness have been already observed for Yamal [*Leibman et al.*, 2015], where active layer thickness spatial patterns are unknown outside of the sites with in situ measurements.

Analytical procedures exist to estimate ALT, such as the Stefan solution [*Harlan and Nixon*, 1978] or the Kudryavtsev equation. While the Stefan solution links the seasonal thaw depth to the accumulated surface thawing-degree days, the Kudryavtsev equation accounts for the effects of snow cover, vegetation, soil moisture, thermal properties, and regional climate [*Kudryavtsev et al.*, 1974; *Yershov*, 1998; *Shiklomanov and Nelson*, 1999]. These methods, although accurate, are labour intensive and limited in spatial coverage [*Gangodagamage et al.*, 2014].

While traditional in situ measuring methods like probing with metal rods are very inefficient at regional scale, remote sensing holds great potential to delineate ALT on a continuous and larger spatial coverage. ALT can be derived by empirical relationships between probe measurements and a physical attribute measurable by remote sensing [*Schaefer et al.*,

2015]. Investigations have been made using the Normalized Difference Vegetation Index (NDVI) [*McMichael et al.*, 1997; *Kelley et al.*, 2004], digital elevation data and land-cover classes [*Nelson et al.*, 1997; *Peddle and Franklin*, 1993]. Especially optical data have been used to retrieve vegetation characteristics (see Table 3.1). A combination with derivatives of digital elevation models has been shown to be of added value [*Peddle and Franklin*, 1993; *Leverington and Duguay*, 1996; *Gangodagamage et al.*, 2014]. Application of high resolution optical satellite data in combination with high resolution digital elevation data from airborne measurements have been shown to be useful for mapping ALT but are very limited in spatial extent. Subsurface thermal properties are also derived from landcover classes, but applicability has been demonstrated only for the permafrost transition zones so far [*Bartsch et al.*, 2016a].

Recently, subsidence rates have been used as input for modelling ALT [*Schaefer et al.*, 2015]. Synthetic Aperture Radar has been exploited using interferometric analyses (InSAR, provides seasonal ground subsidence) in combination with soil properties to estimate ALT without using empirical relationships with probing data [*Schaefer et al.*, 2015].

Most previous remote sensing approaches [*Leverington and Duguay*, 1996; *McMichael et al.*, 1997; *Sazonova and Romanovsky*, 2003; *Schaefer et al.*, 2015] have utilized data with spatial resolutions of 30 m and coarser and were conducted in areas with shallow ALT (less than approximately 70 cm, see Table 3.1). Many regions such as the Yamal peninsula are however characterized by a larger ALT range. Deeper active layers were modeled by analytical approaches [e.g., *Sazonova and Romanovsky*, 2003] or by incorporating only a few ALT classes [e.g., *Leverington and Duguay*, 1996]. For Yamal, previous tests indicate that ALT below 70 cm, 70 - 100 cm and above 100 cm can be distinguished using NDVI [*Leibman et al.*, 2015].

SAR backscatter intensity has so far not been investigated for ALT estimation. Radar backscatter at X-band is also related to vegetation coverage, especially shrubs [*Duguay et al.*, 2015], due to volume scattering, similarly to the NDVI. The microwave signal interacts with leafs in the shrub canopy due to the comparable short wavelength ($\sim$ 3 cm). Leaf size of willows often exceed this wavelength and stems can have significant larger diameters [*Widhalm et al.*, 2016]. Also vegetation water content may influence

the return signal, but no dedicated investigations for tundra species exist. The overall backscatter intensity of a certain surface area is also influenced by surface roughness with respect to the wavelength, as well as by soil moisture. A higher moisture content leads to a higher dielectric constant and therefore higher backscatter values and additionally a reduction in penetration depth. X-band investigations in tundra (Lena Delta) suggest that such variations can occur [*Zwieback et al.*, 2016], but results from *Antonova et al.* [2016b] showed no sensitivity to precipitation over the same area.

In this study we hypothesize that there is a relationship between local ALT and X-band measurements, based on the influence of ALT affecting features on backscatter strength. Like ALT, backscatter is dependent on vegetation cover. Furthermore shrubs, which can be monitored with X-band data, can be related to snow cover due to their characteristic of retaining snow [*Domine et al.*, 2016]. Moreover the terrain in this region is closely linked to drainage and water content which are influencing ALT. These characteristics are in turn influencing the predominant vegetation, which, including soil moisture, can be captured with microwave backscatter. We use in situ records from several sites in the proximity of a long-term monitoring site on Yamal and discuss the results with respect to previous approaches which use remotely sensed information as proxy for ALT.

3.2   Study area and datasets

3.2.1   The Vaskiny Dachi monitoring site

The Vaskiny Dachi research station (70°20′N, 68°51′E) was established in 1988 and is situated in the central Yamal Peninsula in a system of highly-dissected alluvial-lacustrine-marine plains and terraces. It is located within a region of continuous permafrost where tundra lakes and river flood plains are the most prominent landscape features [*Leibman et al.*, 2015]. Dense dwarf shrubs (Betula nana) are widespread on the watersheds. Well-drained hilltops are occupied by dwarf shrub-moss-lichen communities. On gentle poorly drained slopes, low shrubs and dwarf shrubs are well developed and mosses predominate. On convex tops and windy hill slopes, shrub-moss-lichen communities with spot-medallions are predominant. River valleys, thermocirques, and landslide cirques with thick snow cover are characterized by willow thickets. Sedge and sphagnum bogs and flat-topped polygonal

Reference	Remotely sensed data	ALT measurement	Resolution	Study area	ALT	Accuracy
Peddle and Franklin (1993)	SPOT imagery (land cover) and photogrammetric DEM	In situ soil probing at regular intervals throughout field sample sites of 60×60 m	20 m	Ruby Range, southwest Yukon Territory, Canada	Classes: <25 cm; 25–50 cm; >50 cm; no permafrost	79 % agreement for the four classes
Leverington and Duguay (1996)	Landsat Thematic Mapper (NDVI, land cover) and DEM data	Pit measurements supplemented by three ground-probing measurements at 5 m intervals in four directions at each site	30 m	Mayo region, central Yukon Basin, Canada	Classes: <70 cm; 70–150 cm; >150 cm	93 % agreement for the three ALT classes
McMichael et al. (1997)	Landsat Thematic Mapper and handheld radiometer (NDVI)	Median of five ground-probing measurements at each sample point	30 m	Prudhoe Bay and Happy Valley, North Slope, Alaska	Average: <35 cm	No relationship between NDVI and ALT on the Alaska North Slope in areas with little variation in relief. In areas where topography strongly controls the flow and redistribution of water, NDVI did account for approximately 40 % of the variability
Gangodagamage et al (2014)	Lidar (local slope and landscape curvature) and Worldview-2 (NDVI)	Probing along transects of diverse length and at various intervals	2 m	Barrow, Alaska	20–70 cm	$R^2 = 0.76$ and RMSE ± 4.4 cm
Schaefer et al. (2015)	Subsidence from multiannual Phased Array type L-band Synthetic Aperture Radar (PALSAR)	Average of calibrated ground-penetrating radar (GPR) measurements within each pixel ($\sim$40 traces per pixel); probe measurements at two CALM sites (1×1 km grid with 100 m interval, 10×10 m plot random point placement)	$\sim$30 m	Barrow, Alaska	Average: 30–40 cm; <40 cm in areas outside of drained lake basins	$\sim$76 % of the study area within uncertainty of the used ground-penetrating radar and probing data ($\sim$8 cm)

Table 3.1: Studies which used satellite data for determination of active layer thickness (ALT): type of satellite data, accuracy and active layer ranges
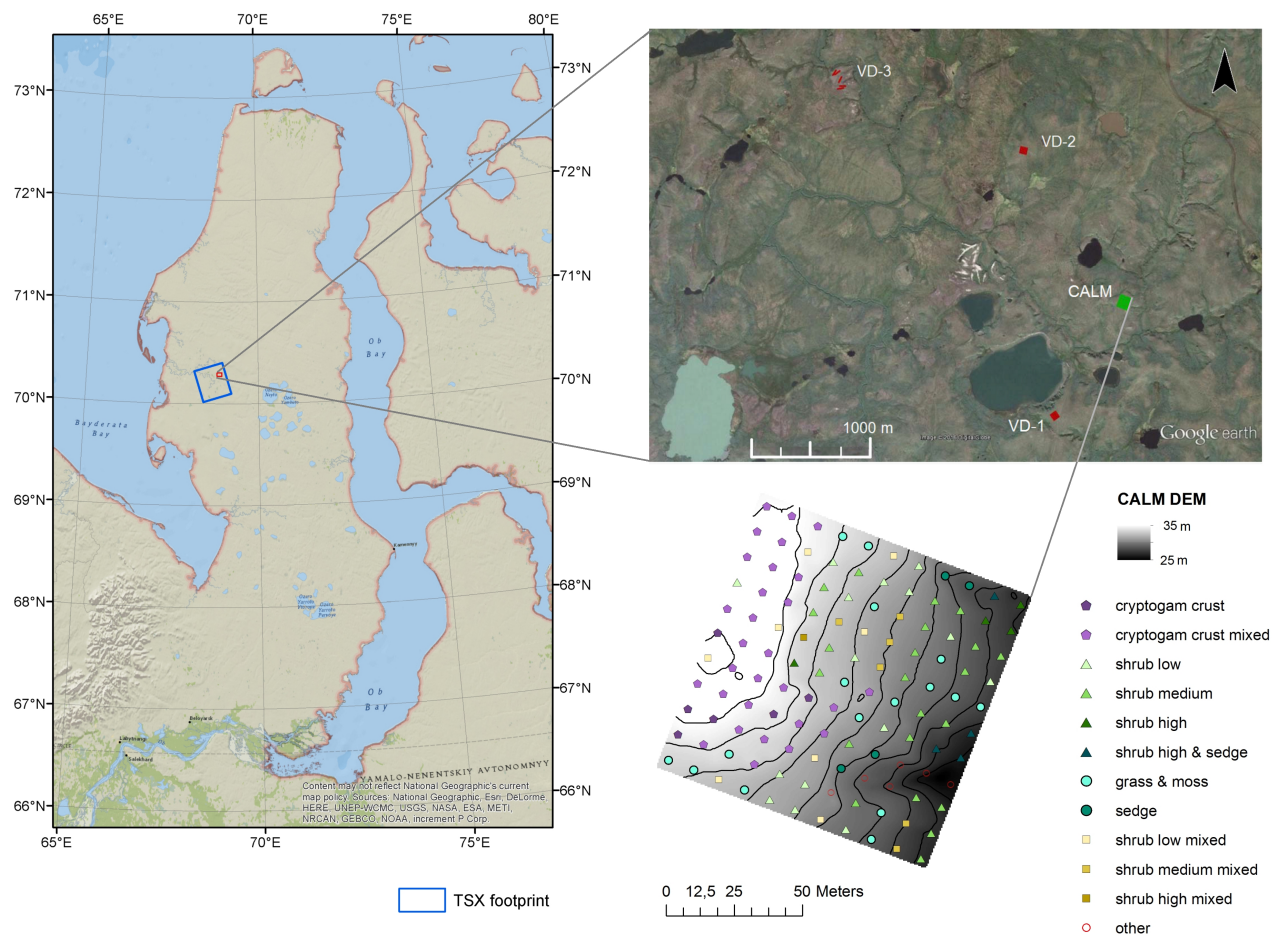
Figure 3.1: Location of the study area (with monitoring sites Vaskiny Dachi (VD) 1-3 and CALM gird) within the Yamal peninsula and CALM grid DEM with land cover information (Sources left: ArcMap Basemap: National Geographic, Esri, DeLorme, HERE, UNEP-WCMC, USGS, NASA, ESA, METI, NRCAN, GEBCO, NOAA, increment P Corp. Source top right: Google Earth, Image 2016 Digital Globe. Bottom right: DEM *Dvornikov et al.* [2016], land cover information from vegetation survey of August 2015)

peatlands are common on flat and concave (saddles) surfaces of watersheds and terraces, in the river valley bottoms, on low lake terraces and in other depressions [*Khomutov and Leibman*, 2014a].

The study area is characterized by continuous permafrost. ALT ranges between 40 cm in peat and up to 120 cm on sandy, poorly vegetated surfaces [*Melnikov et al.*, 2004; *Vasiliev et al.*, 2008; *Leibman et al.*, 2011, 2012]. There are extremes observed on high-center sandy polygons, which can be 11.5 m high and up to 10 m in diameter, with active layer exceeding 2 m. Spatial changes in ground temperature are controlled by the redistribution of snow which results from strong winds characteristic for tundra environments and the highly

dissected relief of Central Yamal [*Dvornikov et al.*, 2015]. Lowest ground temperature is characteristic for hilltops with sparse vegetation where snow is blown away. The warmest are areas with high willow shrubs, due to the retention of snow, found on slopes, in valleys and lake depressions. While the spatial distribution of ALT depends on lithology and surface covers, temporal fluctuations are controlled by ground temperature, summer air temperature and summer precipitation [*Leibman et al.*, 2015].

3.2.2   In situ measurements

In 1993 a Circumpolar Active Layer Monitoring (CALM) site was established at Vaskiny Dachy, placed on the top and slope of a highly dissected plain, affected by landslides, with sandy to clayey soils. The CALM program, designed to observe the response of the active layer and near-surface permafrost to climate change, currently incorporates more than 100 sites. The International Permafrost Association serves as the international facilitator for the CALM network, which is now part of the WMO Global Terrestrial Network for Permafrost (GTN-P) [*Brown et al.*, 2000].

Within the Greening of the Arctic (GOA) project of the International Polar Year (IPY), which was funded by NASA's Land-Cover Land-Use Change (LCLUC) program, three additional monitoring sites were established in the Vaskiny Dachi area [*Walker et al.*, 2009]. Study sites were established within areas with more or less homogeneous vegetation. The site Vaskiny Dachi-1 (VD-1) has clay soils and the vegetation is heavily grazed sedge, dwarf-shrub-moss tundra. Soils at Vaskiny Dachi-2 (VD-2) are a mix of sand and clay, its vegetation is heterogeneous, but dominated by dwarf birch, small reed grass and sedge, cowberries and mosses. At Vaskiny Dachi-3 (VD-3) the soils are sandy and the vegetation is a dry dwarf-shrub-lichen tundra [*Walker et al.*, 2009].

The ALT is measured by a metal probe according to CALM protocol. This involves a late season mechanical probing, in this case late August, when ALT is near its end-of-season maximum. A 1 cm diameter graduated steel rod is inserted into the soil to the depth of resistance to determine the depth of thaw [*Brown et al.*, 2000].

ALT is measured at a spacing of 10 m within the 100 x 100 m grid at the CALM site, resulting in 121 measuring points. The VD sites feature 5 transects respectively. At VD-1

and VD-2 these transects form grids of 50 x 50 m. Transects are 12.5 m apart and ALT is measured every 5 m, resulting in 55 measurement points per site. The transects at VD-3 are arranged to areas of homogeneous vegetation [*Walker et al.*, 2009]. The site of VD-3 features higher ALT values, most likely because of the present sandy soils, which yield a greater conductivity and water permeability (higher convective heat exchange). The CALM grid site is far more heterogeneous than the other VD sites and holds patches of dry cryptogam crust, grasses and mosses, low and high shrubs as well as some wet sedge spots. Cryptogam crust is encountered at the concave hilltop, while high shrubs were mostly located at the landslides (Figure 3.8). Here, ALT is locally higher due to high salinity of clayey deposits which contain no ice under negative temperature and do not resist to probing.

In August 2015, we carried out a dedicated vegetation survey of each CALM grid point, where we determined the dominant vegetation cover within a 3 x 3 m area (Figure 3.1). The following classes are distinguished: Cryptogam crust, low shrubs (<15 cm), medium shrubs (15 -30 cm), high shrubs (>30 cm), grass and moss as well as a class where sedges dominate and classes of mixed vegetation. Further information on vegetation has been collected outside of the ALT measurement sites in August 2014. Over 60 points were registered but only 36 of these points could be further used because of low homogeneity with respect to the spatial resolution of the satellite data. This survey included the most dominant classes of the region and therefore covered more types than can be found at the VD sites or the CALM grid: low shrubs (<20 cm), medium shrubs (20 -60 cm), high shrubs (>60 cm), Cryptogam crust, and a mixture of grasses and sedges.

Furthermore we conducted moisture measurements at the CALM grid. We used the Delta-T Wet Sensor with HH2 handheld to measure the moisture content of the top 5 cm at each grid point on three dates in August 2015.

3.2.3 X-band data

X-band data has so far been used to investigate surface deformations like thaw subsidence and frost heave [*Beck et al.*, 2015; *Zhang et al.*, 2016; *Wang et al.*, 2016], for monitoring tundra shrub growth [*Duguay et al.*, 2015] or dating drained thermokarst lake basins

[*Regmi et al.*, 2012] related to permafrost research.

Backscatter information from data of the TerraSAR-X mission have been used for this study. The digital elevation model available from the TanDEM-X mission has been used as auxiliary data set for TerraSAR-X data preprocessing.

The German national SAR-satellite system TerraSAR-X is based on a public-private-partnership agreement between the German Aerospace center DLR and EADS Astrium GmbH. It was launched in June 2007 and started its operational service at the beginning of 2008 [*DLR*, 2009]. The satellite flies in a sun-synchronous, dawn dusk orbit with an 11-day repeat period. TerraSAR-X features an advanced high-resolution X-Band Synthetic Aperture Radar with a centre frequency of 9.65 GHz corresponding to a wavelength of about 3.1 cm. TerraSAR-X operates in Spotlight-, Stripmap- and ScanSAR Mode with various polarizations. In this study HH (horizontally sent and horizontally received) polarized images of Stripmap mode were used, which image strips of 30 km width at 3 m resolution [*Werninghaus et al.*, 2004].

Six images from August 2014 and 2015 (three images per year) were obtained as SSC (Single Look Slant Range Complex) and have been acquired in the same ascending orbit and beam (incidence angle range 27.3° - 30.3°).

The TanDEM-X mission is an extension of the TerraSAR-X mission, coflying a second satellite of nearly identical capability in a close formation. This enables the acquisition of highly accurate cross- and along-track interferograms without the inherent accuracy limitations imposed by repeat-pass interferometry due to temporal decorrelation and atmospheric disturbances [*Krieger et al.*, 2007]. In this study the TanDEM-X Intermediate DEM (IDEM, $\sim$ 12 m pixel spacing, <10 m absolute horizontal and vertical accuracy) was used for terrain correction, which, compared to the final TanDEM-X DEM product, might have limitations with respect to product quality and completeness [*DLR*].

3.2.4 Landsat data

Landsat 8, launched in 2013, is a NASA (National Aeronautics and Space Administration) and USGS (Department of the Interior U.S. Geological Survey) collaboration, which extends the 40 year Landsat record. It carries two sensors, the Operational Land Imager

(OLI) and the Thermal Infrared Sensor (TIRS), which spectral bands remain comparable to the Landsat 7 ETM+ and operate in the visible, near-infrared, short wave and thermal infrared. Landsat 8 flies in a near-polar, sun-synchronous 705 km circular orbit and acquires data in 185 km swaths segmented into 185 km x 180 km scenes. For this study two Level 1 terrain-corrected (L1T) scenes of 22nd July 2014 and 10th August 2015 were obtained in order to calculate NDVI (spatial resolution 30 m) and compare the already established approach of using NDVI for ALT delineation to the in this study introduced approach of utilizing TerraSAR-X backscatter.

3.3 Methodology

In Microwave Remote Sensing the radar backscatter is dependent on sensor parameters like incidence angle, polarization and wavelength and also on geometric parameters such as surface roughness and vegetation structure, as well as soil properties. Shorter wavelengths do not penetrate as much as longer wavelengths into vegetation and soil, therefore short wavelengths like X-band rather yield information about the upper layers of vegetation [*Ulaby et al.*, 1982]. The assumption for this study is that surface roughness variations play a minor role regarding spatial backscatter differences across the study site. Backscatter increases with increasing vegetation height for X-band in tundra what originates from volume scattering and double bounce (leading to higher backscatter) rather than surface roughness [*Ullmann et al.*, 2014]. It can be also expected that soil moisture variations are not reflected in X-band measurements when vegetation cover is present. The assumption is that volume scattering and double bounce in vegetation is the main contributor to spatial differences in backscatter. Several studies exemplified the separability of tundra shrubs from their surroundings [*Ullmann et al.*, 2014; *Duguay et al.*, 2015]. In *Antonova et al.* [2016b] it is shown that X-band time series analysis allows a clear discrimination of major landscape elements in tundra regions.

The local vegetation patterns are influenced by terrain and soil moisture and also correlate with snow cover thickness, which are all ALT influencing factors [*Shiklomanov and Nelson*, 1999; *Gomersall and Hinkel*, 2001; *Kelley et al.*, 2004]. Areas with shrubs have higher snow cover, which prevents the ground from cooling in the winter. The ALT might be

therefore also higher than in the surrounding area. Based on results of previous studies which utilized the vegetation index NDVI (Table 3.1) and the mutual dependency of NDVI and radar backscatter on vegetation coverage, it is expected that a relationship between X-Band backscatter measurements and ALT is given. We compiled a data set based on TerraSAR-X which allows the investigation of this relationship. This included for SAR common pre-processing steps to account for variations due to viewing geometry.

Six TerraSAR-X images from August 2014 and 2015 were processed (three images per year). It is assumed that within this time stable phenological conditions can be expected. Utilising the software NEST (Next ESA SAR Toolbox) Range-Doppler Terrain Correction was performed with a TanDEM-X Intermediate DEM ($\sim$ 12 m resolution) in order to orthorectify the images and to compensate for distortions due to topographical variations and the tilt of the sensor. Images were processed to a pixel spacing of 2 m and a radiometric normalization was applied to account for incidence angle dependent sensitivity. The so called resulting σ_0 values were then converted into dB. The term backscatter refers in the following to these values, which represent the normalised measure of the radar return. SAR data are affected by so called speckle which is a noiselike effect. It can be understood as an interference phenomenon due to a number of scatterers within each resolution cell. The images were therefore further averaged over time and a spatial filter (average value of the cells in the neighbourhood was calculated: 5 x 5 cells - 10 m) was applied to subdue this noise.

Backscatter as well as NDVI values for the sites VD-1, VD-2 and VD-3 were extracted and compared to the mean ALT values of 2014 and 2015 of each measuring point. The relationship of backscatter values and ALT was examined by varying representations. Bloxplots for ALT classes and for backscatter classes are shown in Figure 3.4. ALT values were separated into 10 cm classes and the backscatter classes ranged 1 dB, allowing a representative number of sampling points per class (7 and 13 points minimum per class respectively). σ_0 values as well as NDVI values were additionally compared directly to ALT by scatterplots (Figure 3.5). Fitted linear functions were applied to characterise the relationship between TerraSAR-X backscatter and NDVI respectively and ALT values of the sites VD-1, VD-2 and VD-3. The coefficient of determination ($R^2 = 1 - \frac{\sum (y_i - f_i)^2}{\sum (y_i - \bar{y})^2}$,

the proportion of the variance in the dependent variable that is predictable from the independent variable) was calculated for the regression lines which involved all VD sites, as well as for regression lines for each VD site separately (Table 3.2). Validation has been undertaken using ALT measurements at the CALM grid. RMSE was calculated representing the modelled ALT (linear regression of all VD sites) versus the measured ALT at the CALM site. Moreover χ^2 was determined, which also accounts for observational uncertainties. An observational uncertainty of 4 cm was assumed for the probe measurements which has been investigated by *Leibman* [1998] for sandy soils (2 - 4 cm) in this region. The modelled and measured ALT values at the CALM grid were further compared by scatterplots depicting the different vegetation types (Figure 3.7) in order to investigate their impact. Backscatter statistics have been also derived for different vegetation classes from locations of the 2014 survey outside of the ALT measurement sites (Figure 3.2). These locations represent relatively homogeneous sites (with respect to TerraSAR-X spatial resolution). The ALT sites, especially the CALM grid, are comparably heterogeneous and therefor of limited applicability for determination of backscatter dependence on vegetation type. The relation of vegetation type and soil moisture was examined for the CALM grid using moisture measurements of August 2015 (Figure 3.3).

3.4   Results

The assumption that backscatter increases with increasing amount of vegetation could be confirmed for the Vaskiny Dachi area (Figure 3.2). There is a difference of about 2 dB between the median for shrubs less than 20 cm and those larger than 60 cm. σ_0 values for the grass/sedge class do however exceed these values. Cryptogam crust backscatter is at the same order of magnitude as shrubs between 20 and 60 cm height. Although the sparse vegetation at these areas consists mostly of lichen and volume scattering within is negligible, these spots often show higher surface roughness or even hummocks which may lead to a rise in backscatter amount. The boxplot of Figure 3.3 which shows the relationship between soil moisture and vegetation types at the CALM grid reveals that lowest soil moisture is encountered for areas with cryptogam crust, while higher shrubs and especially sedges dominate in areas of high soil moisture.
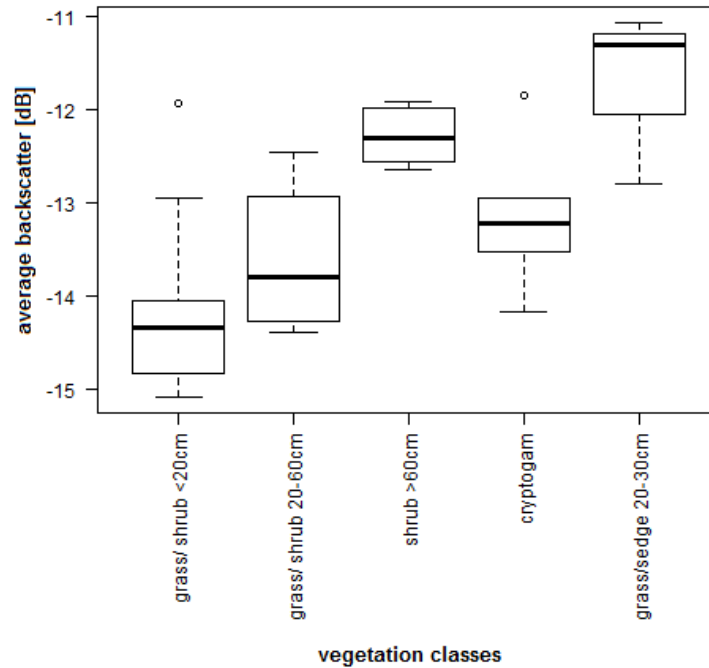
Figure 3.2: Boxplot for backscatter values of various vegetation types. The used points were recorded within a field campaign in 2014. Backscatter values were extracted from the temporally averaged and spatially filtered image of August 2014 and 2015 acquisitions.

Class statistics (Figure 3.4) indicate a relationship between σ_0 and larger thaw depths. Low backscatter values dominate in areas with low ALT and high backscatter values coincide with high ALT. However, the median σ_0 for shallow ALT does not decrease with decreasing ALT at the same rate as for deeper ALT. The scatterplots of the filtered σ_0 and ALT values of the sites VD-1 to VD-3 also indicate this correlation (see Figure 3.5). It also becomes apparent that the change in slope, that is visible in the boxplot of Figure 3.4, is caused by different backscatter values of the sites VD-1 and VD-2 (Figure 3.5). Nevertheless σ_0 increases generally with increasing ALT. The overall higher ALT values of VD-3 are reflected by their higher backscatter values. A range of 5 dB can be observed for an ALT range of 100 cm (40 - 140 cm).

A coefficient of determination of 0.66 was obtained for the linear regression of backscatter and ALT values (see Table 3.2). The mathematical form of the regression line is given in Figure 3.5. The standard error of the intercept is 14.00 and 0.96 for the slope respectively. R^2 for the individual VD sites showed highest values for VD-3 compared to VD-1 and VD-2, which both feature lower ALT values. The linear regression which incorporated all
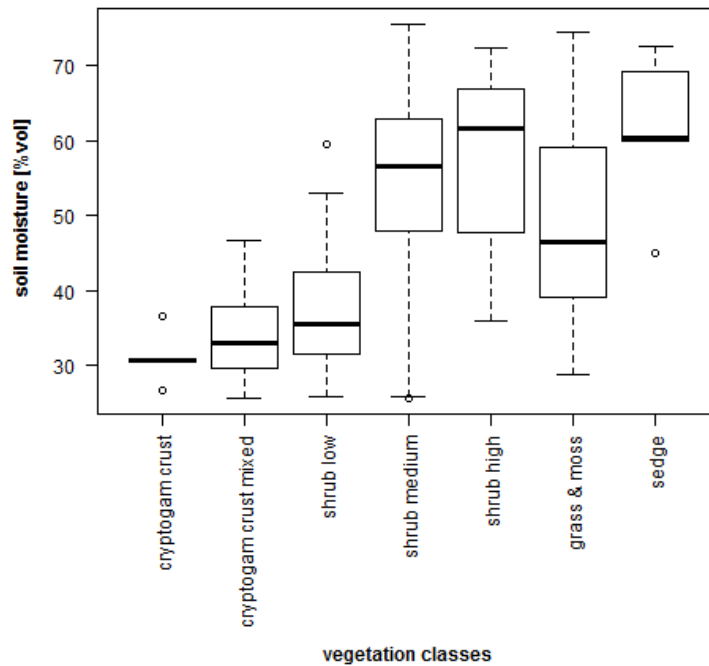
Figure 3.3: Boxplot for mean soil moisture values of three acquisition dates in late August 2015 for vegetation types at the CALM grid.

calibration sites (VD-1, VD-2 and VD-3) yielded an RMS error of 20 cm at the CALM grid site and 25 cm for χ^2. Some VD points showed a backscatter variability of more than 1 dB between the acquisitions of 2014 and 2015. An exclusion of these points would slightly increase the coefficients of determination, but no positive effect could be found with RMSE values at the CALM grid.

The found relationship between TerraSAR-X backscatter and ALT is not that pronounced at the CALM validation site as at the other plots. Especially a patch at the highest elevation of the CALM grid was expected to show higher ALT values according to the calculations from the satellite data (Figure 3.7 and Figure 3.6). There are also some spots with slightly higher ALT than predicted. This applies to ALT larger than 125 cm. With the exception of the area around the hilltop the patterns derived with TerraSAR-X however resemble those of the in situ measurements.

A deeper active layer can be found in areas with high shrubs as well as cryptogam crust at the CALM site (see Figure 3.6). Extremes of ALT can further be encountered at the clay-rich landslides with relatively sparse vegetation, classified as 'other' in Figure 3.6. Thinner active layers were encountered at zones with grass and moss or low shrubs

Dataset	R^2 (VD-1, 2 and 3)	RMSE (cm) (CALM)	χ^2 (cm) (CALM)	R^2 (VD-1)	R^2 (VD-2)	R^2 (VD-3)
TerraSAR-X	0.656	20	25	0.143	0.153	0.622
TerraSAR-X (exclusion of points with high variability	0.712	21	27	0.172	0.167	0.622
NDVI 22 July 2014	0.734	27	46	0.171	0.016	0.017
NDVI 10 August 2015	0.746	30	57	0.002	0.130	0.002

Table 3.2: R^2 between X-band backscatter and NDVI (22nd July 2014 and 10th August 2015) respectively and active layer thickness (ALT). R^2 has been calculated for all calibration sites combined (VD-1,2 and 3) and separately (ALT range for VD-1: 56 - 108 cm; VD-2: 45 - 102 cm; VD-3: 90 - 140 cm). RMSE values represent the modelled ALT (linear regression of sites VD-1, VD-2 and VD-3) versus the measured ALT at the CALM site. χ^2 statistics compare the modelled and measured ALT at the CALM site under consideration of observational uncertainties.

(see Figure 3.6). Residuals increase for depths larger than 125 cm, especially in case of dominance of cryptogam crusts.

In Figure 3.7 a map of the calculated ALT is given for the entire TerraSAR-X scene (open water bodies are masked out). Linear features are expected to be false values as they can be attributed to artificial objects. They show low as well as high ALT values depending on surface roughness and material (air strip and rail track respectively). Values across the scene range between 60 and 180 cm. ALT is higher in drained or partially drained lake basins.

Derived scatterplots of NDVI and ALT values also reveal a relationship within the observed NDVI range of 0.46 0.65 (Figure 3.5). The standard error of the intercept is 9.21 for 22nd July 2014 and 11.60 for 10th August 2015 and 15.80 and 20.21 for the slope respectively. Both NDVI images showed even larger coefficients of determination of about 0.73 - 0.75, than the TerraSAR-X approach (Table 3.2). The achieved RMSE at the validation site is however about 7 cm larger than when using the TerraSAR-X backscatter values. Furthermore, when using only site VD-3, which has the highest range and total thickness of the active layer, comparable to the values at the CALM grid, the linear regression for the backscatter values has a coefficient of determination of 0.622 while for NDVI values it is only 0.017 and 0.002 respectively (Figure 3.5). The NDVI derived ALT values for the CALM site range at most between 70 and 100 cm for 22nd July 2014 and between 60 and 110 cm for 10th August 2015, while measured values have a range of 60 - 150 cm.
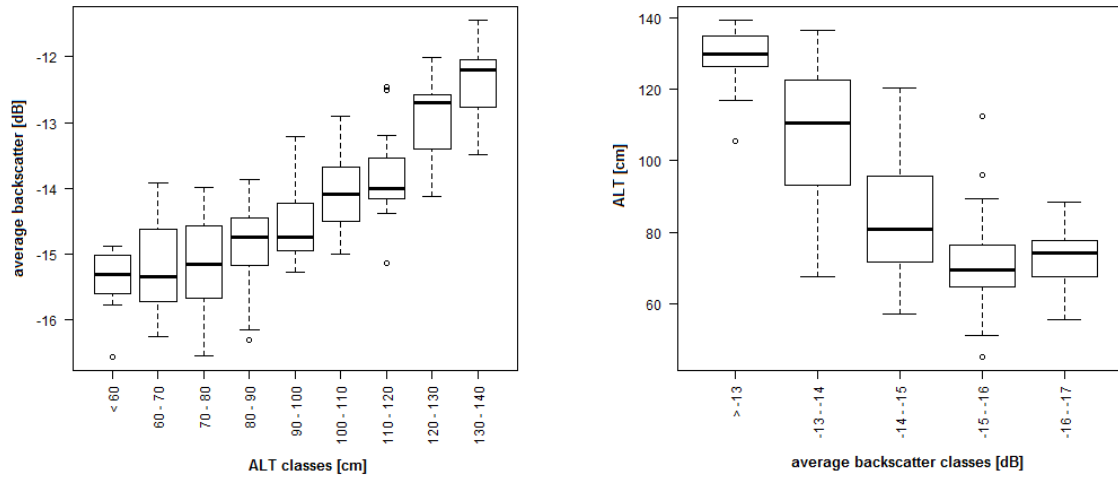
Figure 3.4: Boxplots showing median, minimum and maximum values, first and third quartile and outliers of the ALT and backscatter values of the sites VD-1, VD-2 and VD-3. Left: σ_0 statistics for Active Layer Thickness (ALT) classes (10 cm). Right: ALT statistics for backscatter classes (1 dB).

3.5 Discussion

The assumption that X-band backscatter variations result from mostly differences in volume scattering in vegetation over tundra does not seem to be valid for the selected sites. Radar backscatter is dependent on volume scattering, surface roughness and soil moisture. The influence of all these effects can be perceived in Figure 3.2. For shrubs a major contributor to backscatter is the volume scattering that takes place within the vegetation. A rise in volume indicated by shrub height clearly gives rise to backscatter amount. This effect is also described in *Duguay et al.* [2015], where areas with high shrubs show higher backscatter values. A pronounced relationship was however not found for X-band in HH by *Ullmann et al.* [2014] over the MacKenzie Delta. They applied a smaller spatial filter of 3 x 3 and used data from the end of the growing season (mostly September) when plant decay is already expected to take place. A season related reduction of leaves on shrubs could lead to a decrease in volume scattering and therefore lower backscatter values. The magnitude of backscatter for cryptogam crust, which predominantly occurs on sandy soils, can neither be attributed to volume scattering in vegetation nor to soil moisture (Figure 3.2 and 3.3). Surface roughness or partial interaction within the upper soil may lead to higher backscatter than for grass and low shrubs <20 cm.

High soil moisture is typical for the class segdes (Figure 3.3), giving rise to the backscatter
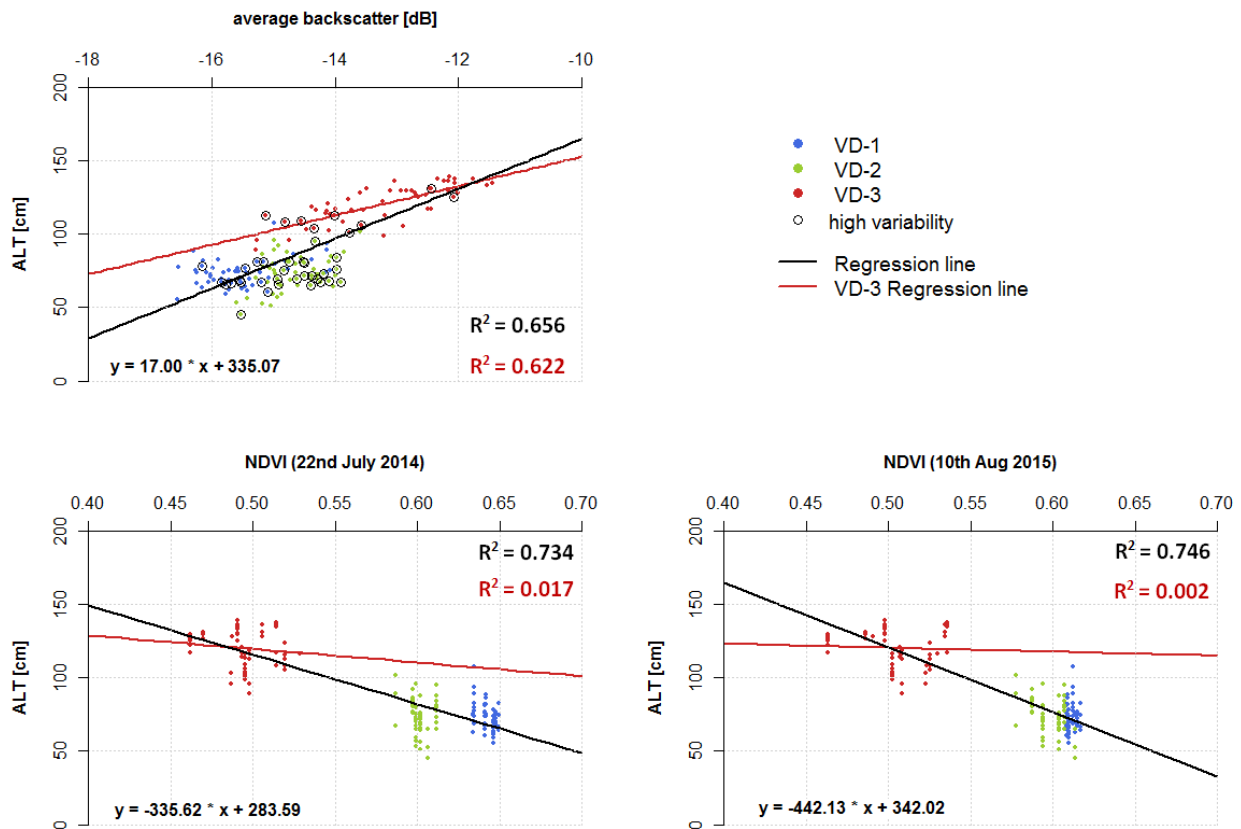
Figure 3.5: Upper Left: Comparison between σ_0 and Active Layer Thickness (ALT) values at the sites VD-1 to VD-3. Points with differences of more than 1 dB between 2014 and 2015 are marked by circles. Linear Regression for σ_0 and Active Layer Thickness (ALT) values of all sites in black and for site VD-3 in red. bottom: Comparison between NDVI (22nd July 2014 and 10th August 2015) and Active Layer Thickness (ALT) values at the sites VD-1 to VD-3. Linear Regression for NDVI and Active Layer Thickness (ALT) values of all sites in black and for site VD-3 in red.

amount. Additionally the so called double bounce effect, which may occur for sedges and grass in standing water, can lead to an increase of received backscatter (Figure 3.2).

Using backscatter intensity at only one polarization (as available for this study) does not allow to distinguish between surface and volume scattering. Polarimetric analyses (using other combinations of H and V polarizations) may help to distinguish the scattering mechanism contributions (see e.g. *Ullmann et al.* [2014]). Data acquired at different polarizations are however not available for the study site.

The above described influences on radar backscatter can be linked to ALT controlling factors. The effect of shrubs on ALT has been described contradictorily by different authors. On the one hand shrubs have been said to have a cooling effect due to shading in
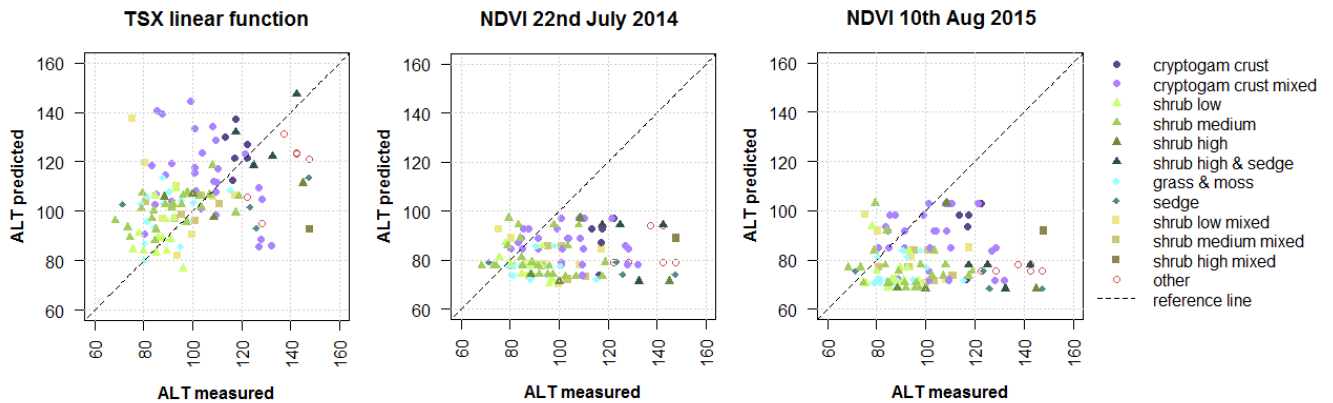
Figure 3.6: Comparison between predicted and measured ALT values at the CALM grid with differentiation between vegetation types for TerraSAR-X and NDVI approaches.

the summer [*Blok et al.*, 2010; *Lawrence and Swenson*, 2011; *Pearson et al.*, 2013], leading to shallower ALT. In other publications [*Domine et al.*, 2016; *Myers-Smith and Hik*, 2013] shrubs have been linked with ground warming due to the isolating effect of snow cover. Shrubs trap wind-blown snow and limit snow erosion by wind. It seems that the prevailing effect of cooling or warming may be caused by the length of winter or summer season. For the CALM site it can be shown that shrubs coincide with deeper ALT (Figure 3.6). However it needs to be noted that shrubs are here found on saline clay, which, as stated before, can lead to higher ALT values measured by probing. In clayey saline soils (with ALT values >130 cm at the CALM site) the freezing point is different from zero and probes can be inserted to greater depths [*Leibman*, 1998].

Soil moisture is another factor that influences microwave backscatter and ALT. It increases the backscatter amount due to the rise of the dielectric constant. It may also lead to higher ALT, caused by an increased heat flux and an enhanced conductive transfer of heat into subsurface layers [*Gross et al.*, 1990; *Shiklomanov et al.*, 2010]. For the Yamal region the measured moisture content is influenced strongly by lithology. While sandy soils are found to be dry, clayey saline soils often hamper infiltration and show higher soil moisture or even standing water. Although barren sandy areas are dryer, they have been shown to have maximal ALT [*Leibman et al.*, 2015] due to higher heat flux, increased by infiltration of rain water. Cryptogam crust is typically found on high centred sandy polygons in the study area. For these points the following restrictions of the used approach become
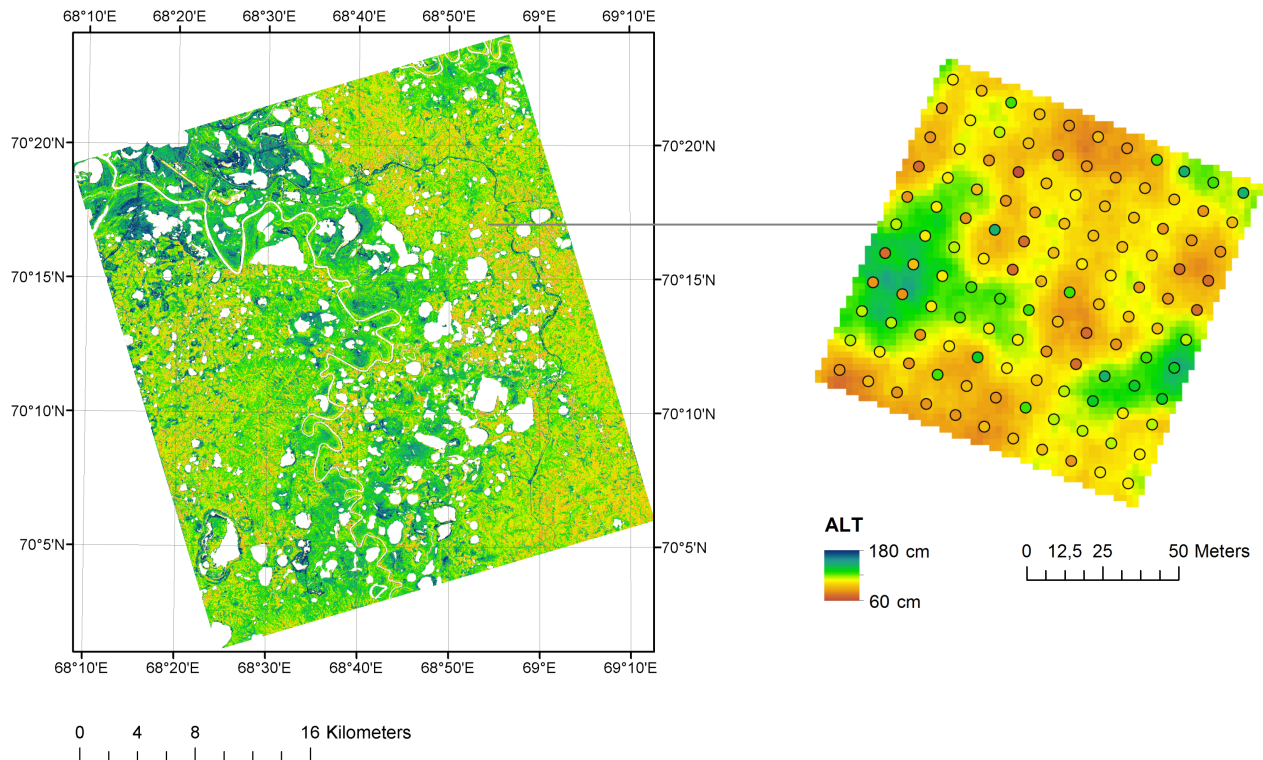
Figure 3.7: Left: Calculated ALT map for the entire TerraSAR-X scenes, based on TerraSAR-X backscatter values. Right: Calculated ALT map (background raster, based on X-band backscatter) for the CALM grid compared to in situ measurements (circles)

apparent. Most points for which the modelled ALT shows high deviations from the in situ data have or lie close to spots of cryptogam crust. The volume scattering for areas with cryptogam crusts is expected to be very low (as described in the Results section) but the recorded σ_0 is comparable to medium shrub heights which have a lower thaw depth. The higher σ_0 values could be due to higher surface roughness. The moisture content itself may also contribute to σ_0, however soil moisture values for areas with cryptogam crust have shown to be very low (see Figure 3.3). Heterogeneity regarding vegetation coverage may also contribute. Especially sites with mixed types show high deviations (see Figure 3.6). The redistribution of water and consequently also the occurring vegetation is controlled by lithology, but also by topography (see Figure 3.8), which has been shown useful in delineating ALT [*Peddle and Franklin*, 1993; *Leverington and Duguay*, 1996; *Gangodaga-mage et al.*, 2014]. Although we did not use topographic information in our study in order to derive ALT, it is indirectly introduced into our measurements through its effects
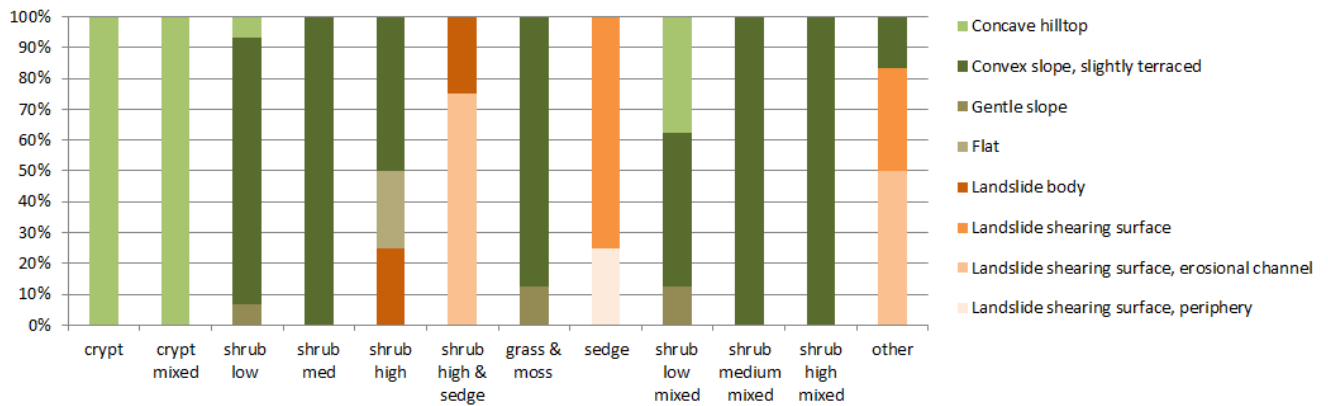
Figure 3.8: Comparison of topographic units (source CALM metadata, Earth Cryosphere Institute SB RAS) and vegetation type (survey of August 2015) at the CALM grid, illustrating the interrelation of certain topographic features and specific vegetation covers.

on vegetation and moisture. For future studies the potential of refining the backscatter approach by incorporating topographic information could be explored.

The comparison of the produced ALT map to the ALT measurements at the CALM grid showed that some points within the validation dataset from the CALM grid are not well represented by the map (Figure 3.7). These sites deviate also in the probe data. For instance for one of these points an ALT of >170 cm was measured in 2014, which is about almost double the values of the surrounding points, and in 2015 only 116 cm were registered. Such an extreme variability of ALT could be explained by an interface between a sandy active layer and a clayey permafrost at this location.

Regarding the delineated ALT map for the entire TerraSAR-X scene (Figure 3.7) it needs to be considered that neither the calibration data (VD sites), nor the validation site (CALM grid) included lowlands with extensive wetlands, as can be found in this region. Because of the lack of ALT measurements for these areas, the shown map is only representative for parts of the region, while lowlands would need further verification and could be masked out using a DEM. The higher ALT in drained lake basins does agree with findings of *Schaefer et al.* [2015] around Barrow. They, however, argue that their algorithm is actually overestimating ALT at these locations.

The comparison of Landsat 8 derived NDVI values and ALT revealed a negative correlation (see Figure 3.5), which is contrary to most studies of other regions [*Gangodagamage et al.*, 2014; *McMichael et al.*, 1997]. However *Leibman et al.* [2015] previously obtained similar

results for the Yamal region at the CALM grid. Results suggest that NDVI is higher for sites with grasses, mosses and sedges than for medium to high shrubs (Salix) although the used near infrared is influenced by plant cell structure and vegetation biomass. These shrubs do, however, coincide with very wet soils (Figure 3.3) and are growing within partially waterlogged depressions. The sensitivity of NDVI to water [*Raynolds and Walker*, 2016] might have an impact over these sites. Furthermore a difference between the training datasets becomes apparent. Both, VD-1 and VD-2, lie within a similarly lower ALT range, but especially the acquisition of 22nd July 2014 shows clearly higher NDVI values for VD-1 than for VD-2. This points to different vegetation types. A difference is also observed for the X-Band backscatter, where VD-1 shows slightly lower backscatter values than VD-2. The backscatter differences could be explained due to a slightly higher surface roughness, which is however not pronounced enough to have a sufficient influence on the sites snow cover or even ALT. Moreover vegetation at VD-2 is rather heterogeneous and also includes patches of sedges or reeds, which could increase the amount of backscatter. While VD-1 and to a small amount even VD-3 also shows sedge vegetation, these sandier sites show a different kind of grass (carex bigelowii instead of calamagrostis holmii). Moreover a clear difference between Landsat acquisitions of 22nd July 2014 and 10th August 2015 exists due to differences in vegetation and their respective phenological cycles [*Bratsch et al.*, 2016], which are in turn influenced by terrain features and consequent draining conditions.

The advantages and disadvantages of the new approach with respect to previous studies could be demonstrated by application of the NDVI approach over the same site and using the same training data set. Investigations presented in this paper showed that the introduced approach of using TerraSAR-X backscatter values to delineate ALT values is suitable to provide higher than 30 m resolution estimates over unsaturated soils with ALT ranging from 40 cm to 140 cm in areas outside of high centred sandy polygons. One previous study that was conducted within comparable ALT ranges used NDVI and land cover information respectively derived from Landsat data in combination with DEM data to derive three classes of ALT [*Leverington and Duguay*, 1996]. A 93% agreement rate for three different ALT classes was obtained. In difference to our study *Leverington and Duguay* used "best-estimate" ALT values from either a pit value, or the average of pit

and probe measurements, and fixed ALT classes. In our study we used measurements for single points from grid points within a 100 x 100 m raster of high heterogeneity. All but one measured ALT value fall into only one ALT class (70 - 150 cm) used by *Leverington and Duguay*. The given accuracy can therefore not be compared.

The used TerraSAR-X data have been acquired in stripmap mode which has a swath width of 30 km. This sensor can however also acquire data over 270 km when using the Wide ScanSAR mode (40 m resolution). This would allow the transfer of the approach to larger regions. The so far investigated incidence angle range is however very limited. Differences in the described backscatter-ALT relationship due to incidence angle effects would need to be considered.

3.6 Conclusions

The common dependency of ALT and X-band backscatter values (HH, approximately 30 degree incidence angle) on land cover types as well as the interrelation of terrain, vegetation, soil moisture and snow cover yields a correlation which can be used to derive ALT with an RMSE of 20 cm over a long term monitoring site on central Yamal. It can be shown that in general higher ALT values correspond with higher backscatter values for the tested ALT range of 40 - 140 cm. The accuracy is lower over sites with mixed vegetation types within the pixels. Especially contributions from areas with little vegetation (cryptogam crusts) alter the relationship between backscatter and ALT. Soil moisture and/or surface roughness are influencing the signal over these sites. Polarimetric SAR analyses which allows to distinguish different scattering mechanisms might be suitable to tackle these issues. This could however not be tested due to unavailability of such satellite data. Results indicate a better performance than NDVI for higher ALT, but investigations with higher spatial resolution optical data would be required for confirmation.

Author Contribution

Barbara Widhalm has performed all data analyses, collected moisture and vegetation information at the CALM site and compiled the manuscript. Annett Bartsch has been

contributing to the development of the concept of the approach as well as to the manuscript. Marina Leibmann and Artem Khomutov have collected the active layer measurements at the long term monitoring sites as well as the vegetation information at sites outside of the ALT monitoring sites and contributed to the interpretation and discussion of the results.

Acknowledgements

Chapter 4

Publication III

Simplified Normalization of C-Band Synthetic Aperture Radar Data for Terrestrial Applications in High Latitude Environments

Widhalm, B.[1], A. Bartsch[1,2], and Robert Goler[1]

[1] ZAMG-Zentralanstalt für Meteorologie und Geodynamik, Hohe Warte 38, 1190 Vienna, Austria

[2] b.geos, Industriestrasse 1, 2100 Korneuburg, Austria

Abstract

Synthetic aperture radar (SAR) applications often require normalization to a common incidence angle. Angular signatures of radar backscatter depend on surface roughness and vegetation cover, and thus differ, from location to location. Comprehensive reference datasets are therefore required in heterogeneous landscapes. Multiple acquisitions from overlapping orbits with sufficient incidence angle range are processed in order to obtain parameters of the location specific normalization function. We propose a simpler method for C-band data, using single scenes only. It requires stable dielectric properties (no variations of liquid water content). This method is therefore applicable for frozen conditions. Winter C-band data have been shown of high value for a number of applications in high latitudes before. In this paper we explore the relationship of incidence angle and Sentinel-1 backscatter across the tundra to boreal transition zone. A linear relationship (coefficient of determination $R^2 = 0.64$) can be found between backscatter and incidence angle dependence (slope of normalization function) as determined by multiple acquisitions on a pixel by pixel basis for typical land cover classes in these regions. This allows a simplified normalization and thus reduced processing effort for applications over larger areas.

4.1 Introduction

Radar backscatter intensity depends on sensor parameters like incidence angle, polarisation and wavelength, as well as on target parameters such as surface roughness, vegetation structure and dielectric properties [*Ulaby et al.*, 1982]. The incidence angle has a major effect on backscatter values of Synthetic Aperture Radar (SAR) acquisitions. It is therefore necessary to eliminate this effect and to normalize the scenes to a single incidence angle in order to achieve comparability of images with different acquisition geometry for many applications. Various approaches for angular normalization exist. Advanced approaches are based on histogram or frequency matching [*Mladenova et al.*, 2013], while many empirical approaches rely on fitting a first or second order polynomial to incidence angle and backscatter values [*Wickel et al.*, 2001; *Loew et al.*, 2006; *Pathe et al.*, 2009; *Baup et al.*, 2007; *Van Doninck et al.*, 2014; *Bartsch et al.*, 2017]. Previous studies [*Mäkynen et al.*, 2002;

Van Doninck et al., 2014] have pointed out that the relationship between incidence angle and backscatter can be considered as linear for a limited incidence angle range. *Mäkynen et al.* [2002] found that the incidence angle range from 19° to 46°, which approximately corresponds to the incidence angle range covered by Sentinel-1, is usually well described by a linear model. However, over sloped terrain, the encountered incidence angle range increases. For example, a terrain slope of 20° may increase an incidence angle range of 20–40° to 0–60° for which the linear approximation is not necessarily valid [*Van Doninck et al.*, 2014]. *Van Doninck et al.* [2014] further showed that the mean values of difference in R^2 (coefficient of determination) of quadratic and linear fits increase with terrain slope. The variation of backscatter with incidence angle depends on scattering mechanisms and therefore on surface variables such as surface roughness and vegetation [*Ulaby et al.*, 1982; *Frison and Mougin*, 1996; *Menges et al.*, 2001]. The dependence decreases with increasing surface roughness [*Mäkynen et al.*, 2002]. The regression line's intercept varies with liquid water content [*Pathe et al.*, 2009]. The parameters of a fitted linear model therefore vary with land cover type, and over time during unfrozen conditions. In order to establish a location specific model, a sufficient set of acquisitions with varying incidence angles (as available usually from overlapping orbits) are required. SAR data availability is, however, in many cases limited [*Bartsch et al.*, 2012] and parameter derivation demands a certain processing effort in addition. A simpler method for the determination of the parameters of the linear model is therefore required for applications over large regions.

By excluding the effects of liquid water content, backscatter only depends on surface roughness and vegetation structure. This can be achieved by using acquisitions under frozen conditions. Frozen surface backscatter information can be used for a variety of applications. In *Widhalm et al.* [2015], the minimum winter backscatter from Envisat Advanced Synthetic Aperture Radar (ASAR) data acquired in Global Mode (GM; 1 km resolution, C-band) was used for the derivation of surface roughness classes, which can be associated with different wetness levels typical for specific landcover types. It was shown that by using minimum winter backscatter values of the GM time series, vegetation physiognomy units of specific wetness regimes could be differentiated for the Arctic region north of the tree line. Further, *Bartsch et al.* [2016b] used GM frozen backscatter as a proxy for soil organic

carbon. A so called 'dry reference' is also essential for the retrieval of relative soil moisture from radar data [*Pathe et al.*, 2009], which can be derived using frozen conditions. In these studies a pixel based approach for normalization was chosen and the linear model derived for the Arctic studies [*Widhalm et al.*, 2015; *Bartsch et al.*, 2016b] based on an average of 46 ASAR GM acquisitions per location. ASAR GM does however only provide 1 km spatial resolution and higher spatial resolution is needed in order to capture the heterogeneity of Arctic environments [*Bartsch et al.*, 2016a]. It has been demonstrated that applications developed for GM can be transferred to data from ASAR operating in Wide Swath (WS) mode (150 m) and they can provide much higher detail and actual landscape patterns [*Bartsch et al.*, 2016b]. It is therefore expected that Sentinel-1, with a resolution of 93 m $\times$ 87 m (range $\times$ azimuth) in EW GRDM (Extra Wide Swath, Ground Range Detected Medium Resolution) mode is of further benefit. Higher spatial resolution maps do however increase the processing and data storage effort in case of the pixel based normalization procedure.

In this study we demonstrate the applicability of a simplified normalization approach for winter (frozen surface) data in Arctic regions. We analyze the C-band backscatter dependency on incidence angle of various Arctic vegetation types in order to derive a universal normalization function for this region. This normalization method is then applied to demonstrate the applicability of a Sentinel-1 derived frozen surface map (sampled to 40 m), as in the study of *Widhalm et al.* [2015] where Envisat ASAR data acquired in Global Mode (sampled to 500 m) was used.

4.2 Material

4.2.1 Sentinel-1

Sentinel-1 is an imaging radar mission which builds on ESAs ERS and Envisat instruments and thereby ensures continuity of C-band SAR data [*Attema et al.*, 2007; *Potin*, 2013; *Torres et al.*, 2012]. The mission is comprised of two satellites which fly in the same sun-synchronous, near-polar orbital plane with a 180° orbital phase difference. Sentinel-1A was launched on the 3rd of April 2014 and Sentinel-1B on the 25th of April 2016. Each satellite has a repeat cycle of 12 days resulting in a revisit time (ascending and descending) of three

days at the equator and less than one day in the Arctic. The SAR instrument operates at a centre frequency of 5.405 GHz and radiometric accuracy is specified to lie within 1 dB (3 σ) [*Potin*, 2013; *Torres et al.*, 2012]. Sentinel-1 operates in four exclusive imaging modes with different resolution and coverage. To avoid conflicts operation modes are pre-programmed. Over land, the predefined mode is Interferometric Wide swath (IW), and over sea-ice and polar zones or certain maritime areas, the Extra Wide swath (EW) mode may be used to achieve wider coverage and better revisit time at lower geometric and radiometric resolution. The data of this study has been acquired in EW mode which is the standard over the Arctic Ocean. Acquisitions extend into the neighboring land areas which are characterized by tundra or the transition zone to the boreal biome. At incidence angles of 19–47° EW covers wide swaths of 400 km at a spatial resolution of 20 × 40 m and utilizes the TOPSAR technique (Terrain Observation with Progressive Scans SAR) using five sub-swaths. EW supports dual polarisation. Building upon the previous study of *Widhalm et al.* [2015] which used Envisat ASAR GM HH data, we only use Sentinel-1 data acquired in HH polarization (horizontally transmitted and horizontally received). The data was obtained from the Sentinel data hubs as Level-1 Ground Range Detected Medium Resolution (GRDM) products, which consist of focused SAR data that has been detected, multilooked (mostly 6 × 2 looks) and projected to ground range using an Earth ellipsoid model [*Potin*, 2013]. Level-1 GRDM data in EW mode has a resolution of 93 × 87 m (range × azimuth) and a pixel spacing of 40 × 40 m. Differences in available number of tracks over a certain location arise due to the predefined mission observation scenario.

4.2.2   Envisat ASAR GM Frozen Surface Backscatter Dataset

Comparisons were made with products from the predecessor of Sentinel-1 in order to assess the results. The minimum winter backscatter product by *Widhalm et al.* [2015] is based on a seven year time series (2005–2011) of Envisat ASAR GM C-band data with 1 km resolution and is available for the entire terrestrial Arctic, north of the treeline. It is masked for lakes and glaciers based on GLWD [*Lehner and Döll*, 2004] and GlobCover [*Bicheron et al.*, 2008]. By comparing this frozen surface map to the Circumpolar Arctic Vegetation Map (CAVM, *Walker et al.* [2002], see Section 4.2.4) it could be shown that the roughness

and the vegetations volume scattering provides the main influence on backscatter in the Arctic region, where wetter areas result in a lower backscatter. The Arctic region above the treeline can be differentiated into the classes wet, medium, dry and other (which represents flat surfaces or sandy soils). Furthermore, the vegetation classes of the CAVM can be divided into different wetness classes which were used to delineate backscatter thresholds. Further investigations by *Bartsch et al.* [2016b] showed that this minimum winter backscatter dataset could also be applied as a proxy to estimate soil organic carbon within the upper meter.

4.2.3 Digital Elevation Models

The 30 arc second resolution DEM GETASSE30 was used as basis for normalization across most sites. Its spatial resolution is comparably coarse but consistent across the Arctic. In order to assess the impact on parameterization, a TanDEM-X elevation model with 12 m spatial resolution (approximately 0.4 arc seconds) representing the covered vegetation zones was used. The available dataset encompasses one tile in northern Alaska (see Figure 4.1). For the mostly mountainous site of Zackenberg an available DEM of 3 arc second resolution was used [*Santoro and Strozzi*, 2012].

4.2.4 Land Cover Data and Focus Regions

In order to analyze the land cover specific backscattering coefficient (σ^0) incidence angle dependence and to investigate the applicability of the derived Sentinel-1 frozen surface maps, land cover datasets representing different locations around the Arctic were used (see Figure 4.1). They comprise classifications of optical satellite data (Landsat, AVHRR). Several additional regions have been selected for assessment of the results (comparison to ASAR GM). They vary regarding heterogeneity (abundance of lakes), vegetation and soils. All regions are areas with past and ongoing research studies linked to land cover [*Bartsch et al.*, 2016a]. Topographic gradients and mean number of tracks are provided in Table 4.1.
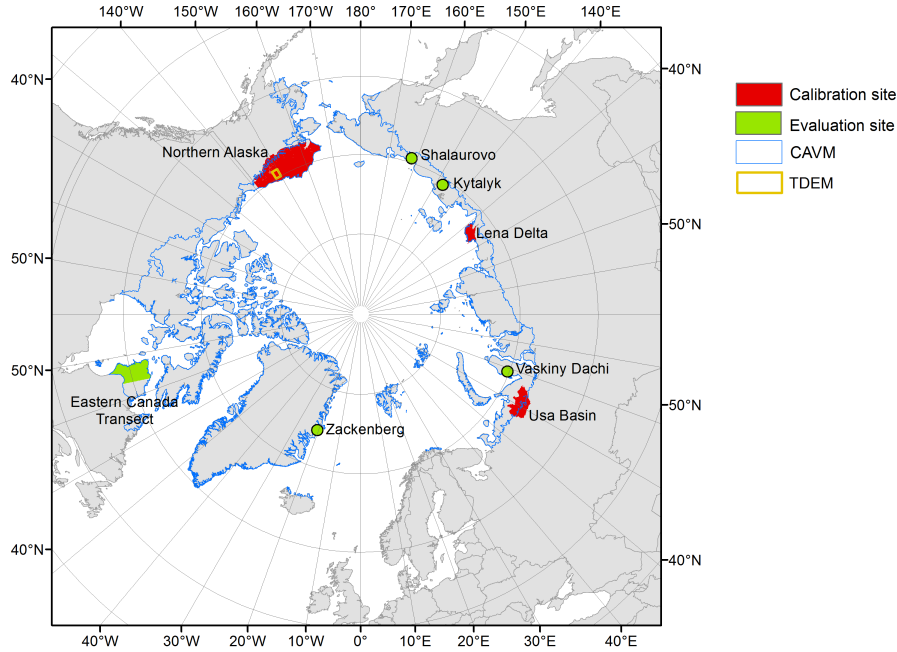
Figure 4.1: Overview of used calibration sites ([*Schneider et al.*, 2009; *Virtanen et al.*, 2004; *Jorgenson and Heiner*, 2003], Usa Basin site extent restricted due to available coverage of Sentinel-1 EW data) and evaluation sites (extent of Zackenberg, Shalaurovo and Kytalyk sites as described in *Bartsch et al.* [2016a], Eastern Canada Transect and Vaskiny Dachi extents as defined in the project DUE GlobPermafrost [*Bartsch et al.*, 2016c] and southern border of the Circumpolar Arctic Vegetation Map (CAVM *Walker et al.* [2002])) and extent of the CAVM and TanDEM-X DEM.

	$\bar{s}$ (°)	s_{max} (°)	$\bar{t}$	# Asc	# Desc	# Scenes
Usa Basin ⋆	0.9	22.8	7.7	10	9	84
Lena Delta ⋆	0.2	14.2	5.0	0	8	44
Northern Alaska ⋆ ◇	4.0	34.3	4.9	13	9	82
Zackenberg ●	6.0	31.8	11.7	11	2	66
Kytalyk	0.0	0.1	3.0	0	4	11
East Canada Transect	0.7	19.0	3.5	6	3	32
Vaskiny Dachi	0.3	1.8	10.8	7	7	90
Shalaurovo	0.9	2.8	3.0	0	3	15

Table 4.1: Mean ($\bar{s}$) and maximum (s_{max}) topographic gradients for calibration and evaluation sites based on the DEM GETASSE30 (resolution 30 arc seconds) and mean number of tracks per pixel ($\bar{t}$). Total number of ascending (# Asc) and descending tracks (# Desc) and total number of scenes per site (# Scenes). ⋆ indicates validation sites. ● for the Zackenberg site a higher resolution DEM (3 arc seconds) was eventually used [*Santoro and Strozzi*, 2012]. ◇ a TanDEM-X DEM (0.4 arc seconds) was additionally used for testing purposes within this region.

Lena Delta

The land cover map by *Schneider et al.* [2009] covers the Lena River Delta in Northern Siberia, the largest Arctic delta. The classification is based on three Landsat 7 Enhanced Thematic Mapper (ETM+) images of July 2000 and 2001 (30 m resolution). Nine land cover classes characterized by their vegetation, surface moisture, and topography are differentiated using supervised classification. Nearly one third of the total area of the Lena Delta is occupied by water bodies. Together with wet and moist land cover classes, the wetland classes amount to over 70% of the Lena Delta area.

Usa Basin

The land cover map by *Virtanen et al.* [2004] covers the catchment area of the River Usa in north-eastern European Russia. Its vegetation zones cover taiga to forest-tundra and tundra to alpine regions. A semi-supervised classification method was applied to a mosaic of spectrally adjusted Landsat TM5 images (30 m resolution, July 2007) from five different dates using relatively sparse ground reference data. Some post classification refinements were implemented using additional GIS data.

Ecosystems Map of Northern Alaska

The Ecosystems map of Northern Alaska by *Jorgenson and Heiner* [2003] (published 2003) is a map of local-scale ecosystems which combines vegetation structure from existing land cover maps with physiography, topography and bedrock characteristics. It covers Alaska north of the treeline and has a 30 m pixel resolution. The developed classification includes seven alpine, nine upland, five lowland, 10 riverine, four coastal, and one human-modified ecotypes.

Circumpolar Arctic Vegetation Map

The Circumpolar Arctic Vegetation Map (CAVM) is based on a false colour infrared image of 1993 and 1995 Advanced Very High Resolution Radiometer (AVHRR, 1 km resolution) data. The 1:7.5 M-scale CAVM is a GIS database which provides the first detailed circumpolar vegetation map of the Arctic tundra. It is derived by manual

photo interpretation and infers vegetation information from expert knowledge of plant communities in relation to climate, parent material and topographic factors [*Walker et al.*, 2002]. The CAVM is currently the only available circumpolar vegetation map, which provides sufficient and consistent thematic content for Arctic regions [*Bartsch et al.*, 2016a].

Evaluation Sites

The landscape of the Zackenberg study site in North East Greenland is mountainous with a broad, flat central valley. Water saturated areas are dominated by fens and gentle slopes are covered in grasslands. Drier patches of the valley are dominated by heath vegetation. Vegetation becomes sparser at higher elevations or is completely absent [*Palmtag et al.*, 2015].

The Kytalyk site lies within the North East Siberian tundra. The site is characterized by three geomorphological units: preglacial Yedoma ice-complex remnants, alas lowlands, and a river floodplain. Alas is a location specific term for thermokarst depressions in Yakutia. The area of the Yedoma remnants is dominated by well-drained tussock and non-tussock tundra. The alas plain is characterized by low-centered polygons, where wet Sphagnum and sedge fen are covering the polygon centers and dwarf shrub fens vegetate the dry elevated polygon rims and irregular frost mounds. The river floodplain holds areas overgrown by Salix bushes (up to 2 m high) and sparsely vegetated sediments [*Siewert et al.*, 2015].

The Vaskiny Dachi research station in the center of the Yamal Peninsula is located in a landscape of highly-dissected alluvial-lacustrine-marine plains and terraces dominated by tundra lakes and river flood plains [*Leibman et al.*, 2015]. The watersheds are characterized by dense dwarf shrubs. Dwarf shrub-moss-lichen communities occupy the well-drained hilltops and willow thickets can be found in river valleys or landslide cirques. Furthermore sedge and sphagnum bogs can be found in river valley bottoms and other depressions [*Khomutov and Leibman*, 2014a].

The Shalaurovo study site in North East Siberia is located in the southern tundra. Well drained upland vegetation is characterized by shrubby tussock moss tundra, while gentle sloped areas are dominated by shrubby grass tundra. Creeks and depressions are vegetated

by willow moss communities and sedge moss fens [*Palmtag et al.*, 2015].

The Eastern Canada Transect is characterized by herbaceous Arctic tundra in the most northern part and shrubby Arctic tundra down to the northern tree line [*Quebec Ministry of Natural Resources*, 2003]. The shrub tundra features lichens, birch and willow shrubs, while the herbaceous tundra is characterized by grass and some willow and heath shrubs [*Lemieux et al.*, 2016]. The landscape is dominated by an abundance of lakes and rivers and vast areas of rugged terrain [*Hachem et al.*, 2009].

4.3 Methodology

The backscattering coefficient σ^0 is strongly influenced by the incidence angle. Since σ^0 incidence angle dependence is controlled by surface parameters like topography, soil surface roughness and vegetation cover [*Ulaby et al.*, 1982; *Frison and Mougin*, 1996], different land cover types exhibit varying σ^0 angular signatures. Due to the increasing influence of the incidence angle with decreasing surface roughness, the angular variations of σ^0 are more pronounced for sparse vegetation and bare surfaces [*Mougin et al.*, 1995].

Higher soil moisture causes a rise in backscatter amount due to its influence on the dielectric properties [*Woodhouse*, 2006]. As described in Section 4.2.2, in Arctic regions backscatter is dominated by the influence of surface roughness and vegetation structure rather than dielectric properties. Frozen ground has backscatter values similar to dry soils. By using winter acquisitions the values only depend on surface roughness, vegetation and snow cover, and the influence of soil moisture can be omitted. The influence of dry snow on C-band radar data can be neglected (e.g., *Bergstedt et al.* [2018]). The assumption is that specific land cover types in the Arctic, as usually determined by optical data in local studies, exhibit a characteristic backscatter level (limited range) under frozen conditions. We processed Sentinel-1 EW GRDM data of selected Arctic regions (see Figure 4.1) to examine σ^0 angular signatures of Sentinel-1 across the Arctic. To enable a comparison to previously used normalization methods applied in *Widhalm et al.* [2015], we processed the data for the month December (2014, 2015 and 2016). It has been shown in many studies that the ground can be identified as frozen with radar data in high latitudes during this period (e.g., [*Naeimi et al.*, 2012; *Bergstedt and Bartsch*, 2017; *Bergstedt et al.*,

2018]). ESA's Sentinel Application Platform (SNAP 5.0) was used for processing. The data was calibrated, terrain corrected and sampled to a resolution of 40 m using the Range-Doppler Terrain Correction and the DEM GETASSE30 (resolution 30 arc seconds; see Figure 4.2). For the mountainous Zackenberg site an available higher resolution local DEM was used. In order to validate the applicability of the 30 arc second DEM GETASSE30 in combination with the higher resolution Sentinel-1 data, we compared regression results obtained from data incorporating GETASSE30 and the high resolution DEM (12 m spatial resolution) based on TanDEM-X. The test was performed over a subsection (148°W–150°W, 69°N–70°N) within the Northern Alaska study site, where a sufficient range of different vegetation types existed. To exclude border noise, areas of 85 pixels in width have been removed at the edges.

In a first step, the standard pixel based local incidence angle (LIA) linear relationship derived from the multi-annual record (with overlapping orbits) was determined for selected sites. This is referred to in the following as the 'pixel based approach'.

In a second step, the dependence of σ^0 on incidence angle variations for the Arctic land cover types was investigated. We analyzed σ^0 (in dB) and local incidence angle for land cover classes of all three Arctic land cover maps used for calibration (Lena Delta, Usa Basin and Northern Alaska; in total 56 samples). They represent a range of land cover classes, flat to moderate terrain and areas with 4.9 to 7.7 mean number of tracks per pixel (Table 4.1). The latter allows for coverage of varying incidence angles in the samples. The EW data was resampled to the 30 m resolution of the landcover maps. Furthermore we separated the land cover classes into groups of estimated vegetation height (see Table 4.2) and examined the scatter of slope and σ^0 values at 30° incidence angle for these groups of vegetation height. We fitted linear functions to the data of each land cover class (backscatter versus local incidence angle) and inferred a function, which could then further be used to normalize the data to a reference angle of 30°:

$$\sigma^0(30°) = \sigma^0(\theta) - k * (\theta - 30°) \tag{4.1}$$

where θ is the local incidence angle and k the slope derived by the delineated function. This method is referred to as the 'slope approach'.

Landcover Class	k	d	R^2	Height	Merged Class
Usa Basin					
Spruce forest	−0.08	−8.81	0.11	high	Forest
Pine forest	−0.16	−7.82	0.22	high	Forest
Mixed forest	−0.09	−8.67	0.12	high	Forest
young stands	−0.09	−8.54	0.11	high	
Willow-complexes	−0.12	−8.16	0.17	high	
Meadows	−0.12	−7.58	0.19	medium	
Bog shrubland	−0.12	−8.39	0.17	medium	
Open bogs	−0.14	−8.45	0.21	low	wet sedge/wetland
Wetlands	−0.16	−8.05	0.24	low	wet sedge/wetland
Shrub-moss tundra	−0.14	−8.96	0.22	medium	low/ dwarf shrub tundra
Dwarf birch tundra	−0.13	−9.19	0.21	medium	low/ dwarf shrub tundra
Shrub-lichen tundra	−0.16	−8.78	0.25	medium	low/ dwarf shrub tundra
dry tundra with some bare peat	−0.16	−8.77	0.27	low	
sparse alpine tundra	−0.12	−8.83	0.12	other	
bare land	−0.07	−8.79	0.03	other	
anthropogenic	−0.13	−7.25	0.09	other	
human impacted tundra-shrublands	−0.10	−9.47	0.15	other	
Northern Alaska					
Coastal Barrens	−0.24	−8.78	0.27	low	non-vegetated/coastal
Coastal Wet Sedge Tundra	−0.23	−8.37	0.31	low	wet sedge/wetland
Coastal Grass & Dwarf Shrub Tundra	−0.22	−7.76	0.31	medium	low/ dwarf shrub tundra
Riverine Dryas Dwarf Shrub Tundra	−0.08	−8.72	0.08	medium	low/ dwarf shrub tundra
Riverine Barrens	−0.18	−6.67	0.17	other	
Riverine Low Willow Shrub	−0.17	−6.20	0.29	medium	low/ dwarf shrub tundra
Riverine Moist Sedge Shrub	−0.18	−7.48	0.24	medium	moist sedge/shrub
Riverine Wet Sedge Tundra	−0.21	−7.17	0.25	low	wet sedge/wetland
Riverine Spruce-Balsam Poplar Forest	−0.17	−6.01	0.31	high	Forest
Riverine Balsam Poplar Forest	−0.16	−5.83	0.38	high	Forest
Riverine Spruce Forest	−0.07	−8.85	0.07	high	Forest
Riverine Tall Alder-Willow Scrub	−0.10	−7.66	0.14	medium	
Lowland Wet Sedge Tundra	−0.24	−6.70	0.40	low	wet sedge/wetland
Lowland Moist Sedge Tundra	−0.23	−6.52	0.46	low	moist sedge/shrub
Lowland Low Birch-Willow Shrub	−0.15	−8.34	0.23	medium	low/ dwarf shrub tundra
Lowland Spruce Forest	−0.17	−5.91	0.43	high	Forest
Upland Birch-Aspen Forest	−0.08	−8.14	0.08	high	Forest
Upland Tussock Tundra	−0.18	−7.38	0.37	medium	tussock tundra
Upland Dryas Dwarf Shrub Tundra	−0.13	−7.65	0.10	medium	low/ dwarf shrub tundra
Upland Shrubby Tussock Tundra	−0.15	−8.32	0.26	medium	tussock tundra
Upland Low Birch-Willow Shrub	−0.12	−8.85	0.15	medium	low/ dwarf shrub tundra
Upland Moist Sedge Shrub	−0.13	−8.80	0.15	medium	moist sedge/shrub
Upland Birch-Aspen-Spruce Forest	−0.07	−8.82	0.07	high	Forest
Upland Spruce Forest	−0.09	−8.18	0.11	high	Forest
Upland Tall Alder Shrub	−0.07	−8.18	0.07	medium	
Alpine Carbonate Barrens	−0.06	−5.73	0.04	other	
Alpine Mafic Barrens	−0.14	−5.13	0.18	other	
Alpine Non-Carbonate Dryas Dwarf Shrub	−0.09	−8.39	0.07	medium	
Alpine Carbonate Dryas Dwarf Shrub	−0.07	−6.44	0.04	medium	
Alpine Mafic Dryas Dwarf Shrub	−0.14	−5.40	0.19	medium	
Lena Delta					
Mainly non-vegetated areas	−0.30	−6.84	0.44	low	non-vegetated/coastal
Dry moss-, sedge-, and dwarf shrub-dominated tundra	−0.23	−7.74	0.51	low	
Wet, sedge- and moss-dominated tundra	−0.20	−7.93	0.37	low	wet sedge/wetland
Dry, grass-dominated tundra	−0.21	−7.61	0.37	low	
Moist grass- and moss-dominated tundra	−0.19	−7.85	0.46	low	moist sedge/shrub
Moist to dry dwarf shrub-dominated tundra	−0.20	−7.34	0.39	medium	moist sedge/shrub
Dry tussock tundra	−0.19	−7.68	0.46	medium	

Table 4.2: Regression parameters (k-slope and d-intercept), height characterization and merged classes of land cover classes used for slope function derivation.
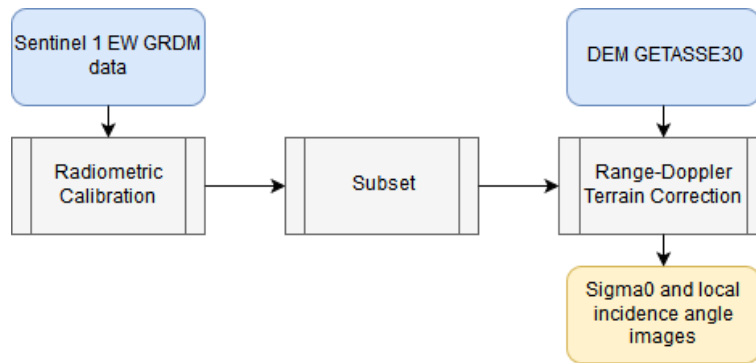
Figure 4.2: Flowchart of the performed pre-processing steps.

The pixel and slope approach were eventually compared in order to test the validity of the new method. The test is performed over the Usa basin area as well as on central Yamal, an area outside of the calibration region. The backscatter minimum was calculated in both cases from all available images of Sentinel-1A of December 2016 in accordance with potential applications. Coverage at the Vaskiny Dachi site was 24 to 30 images and at the Usa site 18 to 24 images.

Additionally, we investigated the applicability of a Sentinel-1 frozen surface map derived from slope function normalized data. Based on *Widhalm et al.* [2015], we calculated the minimum and lower 10th percentile of the normalized Sentinel-1 time series. Data from single and multiple years are assessed in order to evaluate the impact of effects such as rain on snow. We compared our results to the ASAR GM map [*Widhalm et al.*, 2015] and applied the same coarse water body masking. The comparison to the circumpolar vegetation database used in *Widhalm et al.* [2015] was made over selected regions including the evaluation sites (see Section 4.2.4) as well as the calibration regions.

4.4 Results

4.4.1 Normalization

We calculated the regression lines for σ^0 and incidence angle for all 56 land cover classes of our calibration sites (Lena Delta, Usa Basin and Northern Alaska). Figure 4.3 shows classes of all three sites which have been combined into six common classes for visualization purposes. The spread is most pronounced for the forest class, where classes of different tree species are combined. As expected forests show lowest dependency on incidence angle and

highest σ^0 values, while non-vegetated or plain coastal areas exhibit great variations with incidence angle and very low σ^0 values. The dependency on vegetation height can be seen in Figure 4.4. It can be exemplified that classes of shorter vegetation are characterized by high absolute slope values and low backscatter, while for taller vegetation the opposite applies. For the Lena Delta the incidence angle dependency was more pronounced than for the Usa Basin (see Figure 4.4). Absolute slope values are higher in the Lena Delta with an extreme value of -0.3 for mainly non-vegetated areas (see Table 4.2). These higher absolute slope values are associated with lower backscatter values. σ^0 values are higher in the Usa Basin area, which comprises various forest classes. For example, spruce forest exhibits a slope value of -0.08. As the site of Northern Alaska covers flat coastal areas as well as forest regions, slope and σ^0 values are widely spread with high backscatter values and minimal absolute slope values for alpine areas, and low backscatter and maximal absolute slope values for flat coastal regions. The test with the higher spatial resolution TanDEM-X DEM over the North Slope gave similar results. Mean and maximum topographic gradients were $0.8°$ and $9.9°$ for GETASSE30 and $1.7°$ and $48.9°$ for the high resolution DEM. The resulting regression lines showed a low RMS difference of 0.004 (2% of the total range) for slope values and 0.2 (5% of the total range) for intercept values. Consequently, it was assumed that errors of diverging incidence angles, due to a coarser DEM, are negligible in this case and that the derived parameters are valid for moderate terrain (see Figure 4.5). A linear relation between slope and backscatter is apparent (Figure 4.4). The R^2 between k and σ^0_{30} is 0.64. We therefore delineate the following equation to calculate the slope based on given backscatter and local incidence angle values:

$$k = (\sigma^0(\theta) + 8.618)/(\theta - 5.978) \qquad (4.2)$$

with θ being the local incidence angle and k the slope.

We then compared the results of the slope function based normalization to those of the 'pixel based approach' where slope values have been calculated for each pixel separately based on a time series considering multiple tracks. Figure 4.6 shows the results for two regions. The minimum images of the available time series show good agreements for both approaches with mean differences of -0.1 dB for the Vaskiny Dachi site. Some disagreements can be found in the Usa Basin area in mountainous regions (Eastern part)
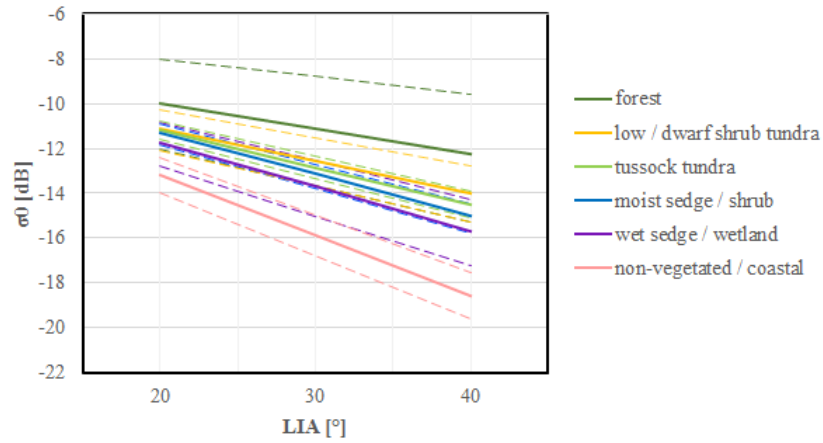
Figure 4.3: Regression lines for σ^0 and local incidence angles of various vegetation types. Regression lines have been derived from data of land cover classes of the sites Lena Delta, Usa Basin and Northern Alaska. The results of all sites have been merged into six combined classes. 1st and 3rd quartile lines are depicted as dashed lines.
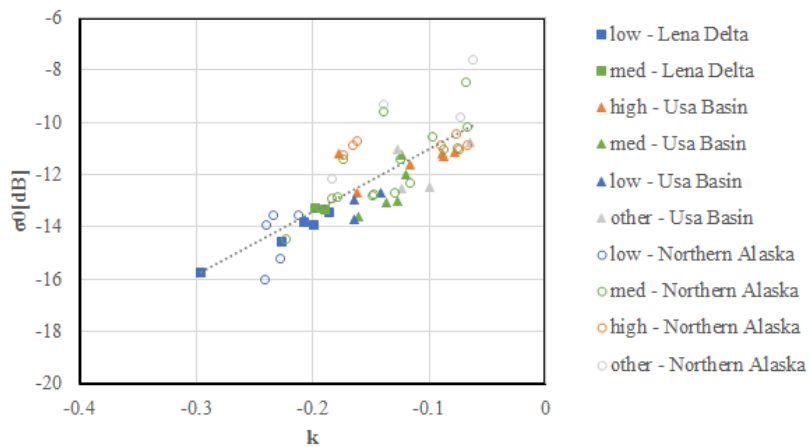
Figure 4.4: Scatterplot of slope and σ^0 values at 30° incidence angle for the sites Lena Delta, Usa Basin and Northern Alaska (depicted in different shapes), with differentiation of approximate vegetation height of land cover classes (depicted in different colors).
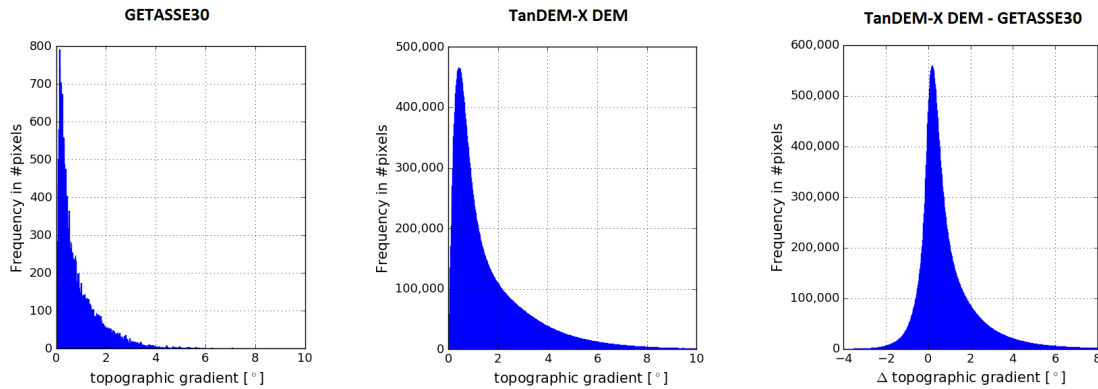
Figure 4.5: Histograms of topographic gradients for GETASSE30 and TanDEM-X DEM of the same area (see Figure 4.1) and histogram of differences in topographic gradient for TanDEM-X DEM-GETASSE30.

with differences of more than 40 dB .

4.4.2 Sentinel-1 Frozen Surface Backscatter Statistics

As the normalization with the slope function seemed to sufficiently match the results of the established pixel based approach, we further investigated the applicability of a Sentinel-1 based frozen surface map using slope function normalized images. When comparing minimum winter images as used for the map delineation in *Widhalm et al.* [2015], it became apparent that the results seemed to be dependent on the number of data sets that were used in the calculation of the minimum backscatter image. Using a higher number of datasets leads to lower minimum backscatter images. This effect could be reduced by using the 10th percentile instead of the minimum (see Figure 4.7). The difference between the minimum images of one and three years is 1.14 dB, while when using the percentile the difference reduces to 0.34 dB.

A comparison with the Circumpolar Arctic Vegetation Map (CAVM), which was also used to delineate the thresholds in *Widhalm et al.* [2015], clearly showed lower values for wet classes than for drier ones within each region (Figure 4.8). Nevertheless, a common threshold that could be applied over all areas could not be derived, due to inconsistencies especially within the moist classes, where different regions showed varying median values for the same CAVM classes. Furthermore dry classes were very scarce within the selected sites with a negligibly low sample size.

Comparing our Sentinel-1 frozen ground percentile and minimum backscatter maps to the
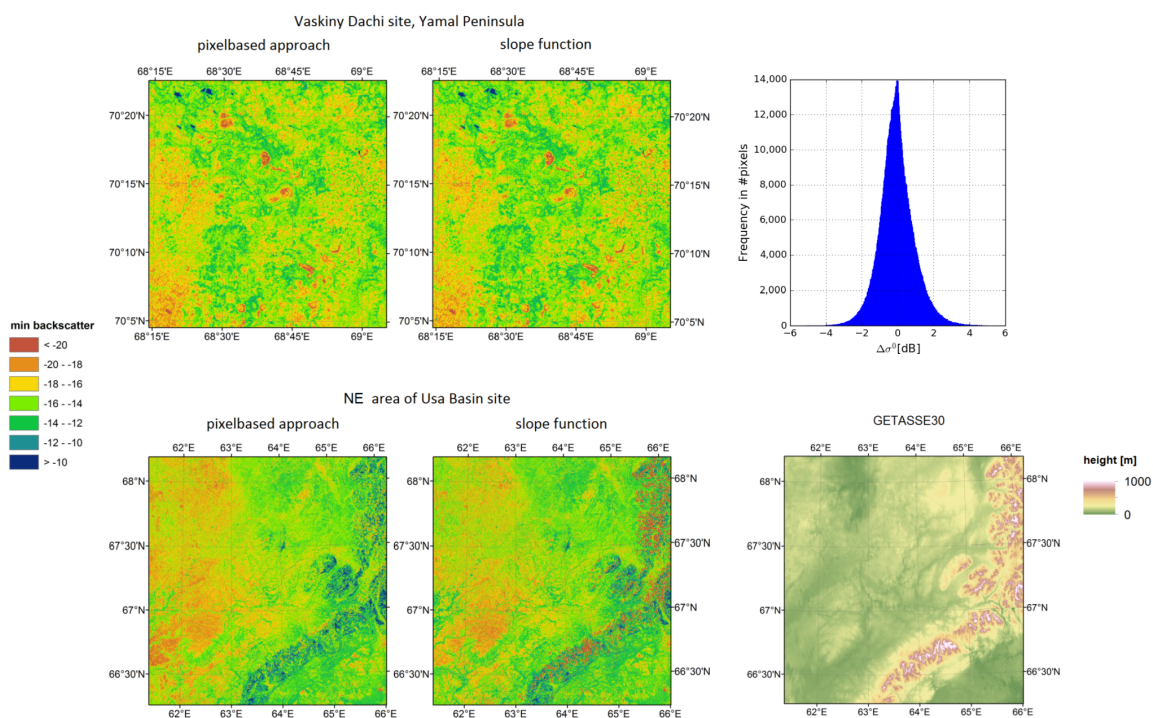
Figure 4.6: Comparison of minimum backscatter images of a timeseries derived from pixelbased normalization (left) versus normalization with slope function (middle) for two different areas (top: region surrounding the Vaskiny Dachi field station on central Yamal; bottom: region surrounding Vorkuta at the northeast Usa Basin site); top right: Histogram for difference of pixel-based minus slope function-based normalization approach (mean = −0.1 dB, std = 1.0 dB); bottom right: DEM GETASSE30 of northeast Usa Basin site.
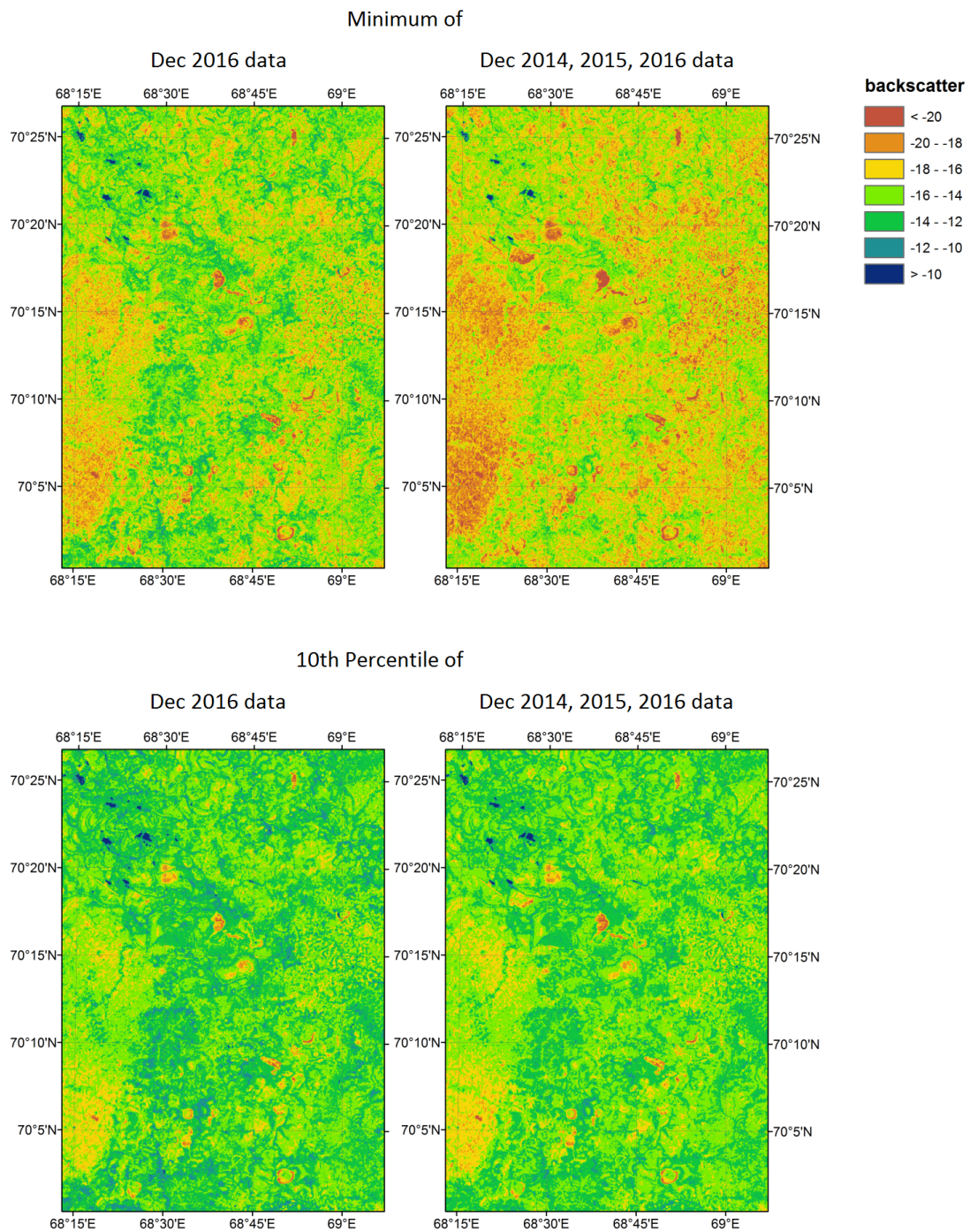
Figure 4.7: Top: minimum backscatter and bottom: 10th percentile of the December 2016 timeseries (left) and December 2016, 2015 and 2016 timeseries (right) of the area surrounding the Vaskiny Dachi field station on central Yamal.
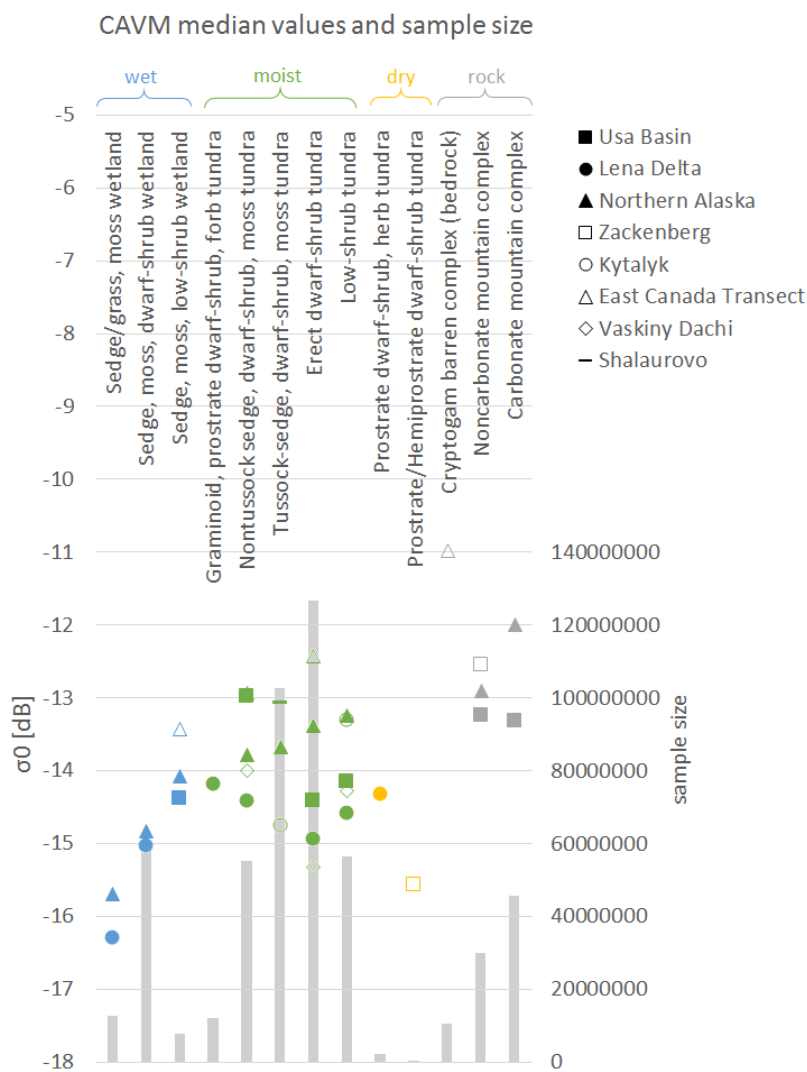
Figure 4.8: Median values of the 10th percentile maps for CAVM (Circumpolar Arctic Vegetation Map) classes of various study regions. CAVM classes are classified as wet, moist, dry and rock (moisture classes according to *CAVM Team* [2003]). The sample size of each class, combined for all regions, is displayed by bars.
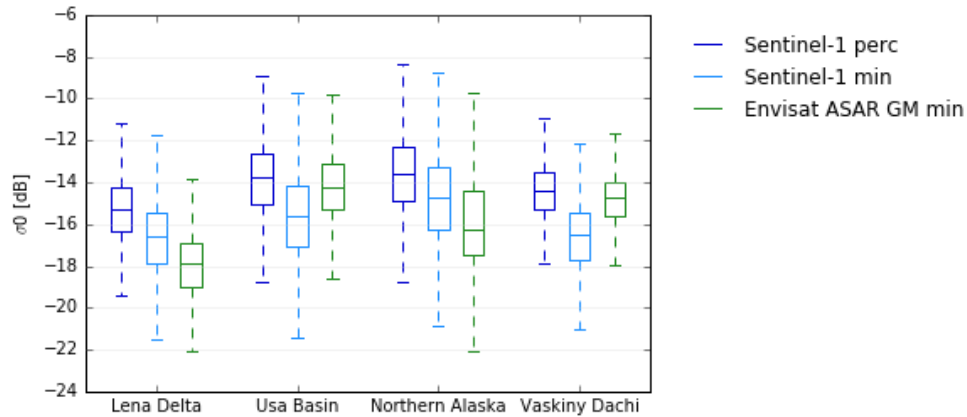
Figure 4.9: Boxplots of the 10th percentile (perc) and minimum (min) maps of Sentinel 1 and of the minimum maps of Envisat ASAR GM for the sites Lena Delta, Usa Basin, Northern Alaska and Vaskiny Dachi.

minimum backscatter maps of Envisat ASAR GM reveals that differences vary depending on study site (see Figure 4.9). We calculated differences between median values of Envisat ASAR GM minimum maps and Sentinel-1 percentile maps for each site. The differences range from 0.4 to 2.5 dB with higher values for Sentinel-1. The Lena Delta and Northern Alaska site both show higher differences, while at the Usa Basin site Sentinel-1 values match those of Envisat ASAR GM to a greater extent. Median backscatter values for Sentinel-1 percentile maps are similar for Northern Alaska and Usa Basin with -13.4 dB and -13.8 dB respectively. However, Envisat ASAR GM median values are much lower for Northern Alaska with -15.9 dB compared to -14.2 dB at the Usa Basin. The lowest Sentinel-1 and Envisat ASAR GM values were found in the Lena Delta (-14.8 dB and -17.2 dB).

4.5 Discussion

4.5.1 Normalization

The analysis of σ^0 and local incidence angle scatterplots of various land cover classes illustrates an adequate linear dependence for the existing incidence angle range in most cases. R^2 values shown in Table 4.2 are naturally lower for smaller slopes. Although the relationship between backscatter and incidence angle were naturally not linear [*Ulaby et al.*, 1982], previous studies affirm our findings and show the applicability of a linear

fit for certain incidence angle ranges [*Frison and Mougin*, 1996; *Mäkynen et al.*, 2002; *Van Doninck et al.*, 2014]. In Figure 4.3 the effect of different vegetation and land cover types on angular signatures is apparent. This is explained by its dependence on scattering mechanisms, and consequently, surface variables such as surface roughness and vegetation [*Ulaby et al.*, 1982; *Frison and Mougin*, 1996; *Menges et al.*, 2001]. The comparison between plain coastal regions, like the Lena Delta and northern parts of the Alaska site, and areas with higher vegetation such as the Usa Basin site and forested zones of the Alaska site, clearly showed a higher influence of incidence angle with classes of lower vegetation and smoother surfaces. As incidence angle dependence increases with decreasing surface roughness [*Mäkynen et al.*, 2002], it is no surprise to find the highest absolute slope values and therefore highest angular dependence for coastal barrens in Alaska and mainly non-vegetated areas like sandbanks in the Lena Delta.

Since surface roughness and vegetation cover not only influence the backscatters dependence on incidence angle, but also the backscatter amount itself [*Ulaby et al.*, 1982], higher absolute slope values are mostly found for land cover classes with lower backscatter values. Since we only used winter data in this study and frozen soils show similar backscatter values to dry soils, the effect of soil moisture on backscatter can be excluded [*Naeimi et al.*, 2012; *Bergstedt and Bartsch*, 2017; *Bergstedt et al.*, 2018]. Therefore with constant sensor parameters, like frequency and polarization, variations in backscatter amount can only be caused by surface roughness and vegetation structure, which remain constant over winter. Due to these mutual dependencies, a linear relationship between σ^0 at a constant local incidence angle, and slope could be derived (see Figure 4.4). In Figure 4.4 again the influence of vegetation height becomes apparent, with low vegetation classes showing low backscatter values in combination with high absolute slope values in contrast to higher vegetation.

Equation (4.2) permits the slope to be calculated for each pixel and each image depending on backscatter amount and local incidence angle. As is done in previous normalization approaches [*Gauthier et al.*, 1998; *Pathe et al.*, 2009; *Van Doninck et al.*, 2014], the acquisitions can be normalized to a common incidence angle by utilizing Equation (4.1). We calculated minimum backscatter images using slope function normalized images of

December 2016. We then compared them to results where the normalization that has been performed using the pixel based approach of employing slope values, which were calculated based on the backscatter and incidence angle time series for each individual pixel. The results revealed hardly any differences for the Vaskiny Dachi site in the central Yamal Peninsula, which is characterized by a gentle relief. However, some deviations were apparent for another site. This second area, which is located around the city Vorkuta at the Usa River, includes the northern part of the Ural mountains. In these mountainous locations distinct differences could be found. As *Van Doninck et al.* [2014] pointed out, in the case of steep slopes, the incidence angle range exceeds that for which the linear approach of the angular dependence is valid. Steep slopes could be found within the sites of Usa Basin at the bordering Ural mountains, for the Brooks Range in Northern Alaska and the mountainous Zackenberg site. Due to the use of the coarser resolution DEM GETASSE30, misregistrations may have occurred for mountainous regions. However, as a linear normalization approach is not suitable for these areas, results can be expected to be erroneous independent on the DEM's resolution.

4.5.2 Sentinel-1 Frozen Surface Backscatter Statistics

Changes in snow structure can cause backscatter to increase during winter in C-band [*Naeimi et al.*, 2012]. To avoid this influence, as well as exclude rain on snow events [*Forbes et al.*, 2016], the minimum winter backscatter from Envisat ASAR GM was calculated in *Widhalm et al.* [2015]. To test the applicability of a Sentinel-1 frozen surface map based on *Widhalm et al.* [2015], we calculated the minimum backscatter images of December time series of slope function normalized images. Investigations revealed a dependency of minimum backscatter values on the number of scenes used in the calculation, with the values clearly decreasing when more scenes from different years were incorporated. This may be caused by the speckled nature of SAR images, whereby an interference caused by numerous scatterers within each resolution cell induces a noise-like effect. Alternatively, the coarse spatial resolution elevation model implemented here for co-registration and slope retrieval may also introduce noise. By using the 10th percentile rather than the minimum, resulting outliers could be avoided, leading to a more stable product, which is less affected by the

number of scenes used in the calculation.

The land cover maps used in this research cover a wide range of years. Changes may have occurred over this time period, like for instance in areas of gas and oil extraction [*Kumpula et al.*, 2012]. This leads to an increase of urban settlements and locally double bounce effects, respectively, which are currently not considered. These areas may need to be treated separately before further application.

A comparison of our Sentinel-1 frozen ground maps to those of Envisat ASAR GM reveals differences between study sites . As we used the 10th percentile for our Sentinel-1 product instead of the minimum, higher backscatter values than for Envisat ASAR GM were expected. However, a constant offset was not apparent. The inconsistent differences could have many causes. For one, the used timespan is not the same for both sensors (2005–2011 for Envisat ASAR GM and 2014–2016 for Sentinel-1) , which could lead to differences related to events such as rain on snow, which do not occur in all winters and regions, and in irregular intervals [*Bartsch*, 2010]. Furthermore the amount of data used in the calculation varies from site to site. While this influence was reduced for the Sentinel-1 product by utilizing the percentile, an effect due to data coverage cannot be excluded for the Envisat ASAR GM maps. However, the Envisat ASAR GM coverage of the Usa Basin site is similar to that of the Northern Alaska region and therefore may not explain the discrepancies. Deviations specifically found for the Alaskan North Slope occurred across different vegetation types and also included the lowland areas.

Some undesired effects during the radiometric calibration of Sentinel-1 data with the SNAP toolbox are apparent. Different results were obtained when only a subset of the scene was processed. We therefore always used the whole scene in the calibration process, however influences due to calibration cannot be estimated. There may also be differences regarding the calibration for ASAR GM datasets, which covered often much larger areas than Sentinel-1 scenes, extending far into the Arctic Ocean. The abundance of small lakes in many Arctic regions may influence the results. While a multitude of small water bodies (with floating ice and therefore high backscatter in December) may be too small to be detected as in the coarser Envisat ASAR GM maps, they can be distinguished for Sentinel-1.

The percentile images of calibration and evaluation sites were compared to the CAVM, which is currently the only available consistent circumpolar land cover map with sufficient thematic content [*Bartsch et al.*, 2016a]. The CAVM team [*CAVM Team*, 2003] identified three different moisture levels for certain vegetation physiognomic units of the CAVM. It can therefore be used for the SAR-based classification approach [*Widhalm et al.*, 2015]. In fact, all tested sites indicated lower median values for wetter areas (see Figure 4.8). However, comparisons between sites indicated issues determining a global threshold between classes. Values of similar classes were lower in the Lena Delta than for the Usa Basin or Northern Alaska. Even the median value of the dry class Prostrate dwarf-shrub, herb tundra in the Lena Delta were lower than some wet or moist classes of the Northern Alaska site. This may result from landscape heterogeneity which is pronounced in the Lena Delta [*Muster et al.*, 2012; *Schneider et al.*, 2009]. Furthermore the differences in sample size must be considered, which varies from site to site (see Table 4.3). The CAVM is based on satellite data with a spatial resolution of only about 1 km. Specifically the moist classes consist of wetter and drier patches. Averaging represents the dominating effect only. Dry CAVM classes are underrepresented in the selected areas (0.5% of samples) and results therefore do not allow for conclusions on the suitability of the threshold method to derive wetness levels from the Sentinel-1 data. Furthermore, the introduced normalization method may not be applicable for lake ice, as the slope is derived depending on backscatter amount. For lake ice, backscatter strongly depends on whether the lake is frozen to the bottom or if the ice is floating, leading to essential backscatter differences, while the slope remains largely unchanged.

The normalization approach may be also suitable to aid soil moisture retrieval. The slope does not change with variations in soil moisture as long as roughness and volume scattering are constant (e.g., [*Pathe et al.*, 2009]). Slope values derived from winter data may therefore be applicable to normalize data independent of acquisition time. Variations of backscatter due to phenology is expected to be limited in tundra regions at C-band but may need to be considered.

	Usa Basin	Lena Delta	Northern Alaska	Zacken-Berg	Kytalyk	East Canada Transect	Vaskiny Dachi	Shalau-Rovo
Sedge/grass, moss wetland		5493	7395					
Sedge, moss, dwarf-shrub wetland		17,904	40,384					
Sedge, moss, low-shrub wetland	4517		1579			1633		
Graminoid, prostrate dwarf-shrub, forb tundra		12,147						
Nontussock sedge, dwarf-shrub, moss tundra	687	117	32,445			21,720	165	
Tussock-sedge, dwarf-shrub, moss tundra			102,517		27			90
Erect dwarf-shrub tundra	9381	2744	34,711		27	79,630	189	
Low-shrub tundra	37,354	2038	16,099				904	
Prostrate dwarf-shrub, herb tundra		2418						
Prostrate/Hemiprostrate dwarf-shrub tundra				35				
Cryptogam barren complex (bedrock)						10,551		
Noncarbonate mountain complex	701		29,372	92				
Carbonate mountain complex	2193		43,613					

Table 4.3: Sample size as depicted in Figure 4.8 (divided by 1000), distinguished by region (Figure 4.1). CAVM classes are classified as wet (blue), moist (green), dry (yellow) and rock (grey; moisture classes according to *CAVM Team* [2003]).

4.6 Conclusions

Normalization of SAR data to a common incidence angle is required for many applications, but this is challenging in heterogeneous landscapes with varying angular dependencies. The analyses of angular signatures of winter C-band backscatter of Arctic land cover types revealed a linear relationship between the incidence angle dependencies of σ^0 and σ^0 itself, which can be exploited for normalization. Images normalized using this new approach showed good agreements with results processed on a common pixel by pixel based approach which requires processing of many scenes acquired from different orbits. However, deviations were found in mountainous regions, where the assumed linear relationship was no longer valid due to an increase in incidence angle range. Although the simplified normalization approach is valid for tundra and the transition zone to boreal forest, the use of multiple acquisitions (and statistics such as use of percentiles) may be beneficial for applications in order to account for other effects (such as rain on snow and speckle).

By comparing the results of Sentinel-1, normalized by the new slope function, and Envisat ASAR GM results, normalized on a pixel by pixel basis, some site specific offsets became apparent, which could not be explained explicitly with the available reference data. They may result from scale and thematic content differences. Nevertheless, the benefit of using higher resolution SAR data can be expected in these heterogeneous landscapes, making less computationally intensive normalization approaches, like the one presented in this

paper, essential.

Acknowledgements

Author Contribution

B.W. developed the concept of the study, conducted all data processing and analysis, the literature research, designed the figures and wrote the majority of the manuscript. A.B. contributed to the concept development of the study, the development of the methodology, the interpretation of the results and writing of the manuscript. R.G. has contributed to the revision of the manuscript.

Chapter 5

Additional Publication A

Site Scale Wetness Classification of Tundra Regions with C-Band SAR Satellite Data

Widhalm, B.[1,2], A. Bartsch[1,2,3], M.B. Siewert[4], G. Hugelius[4], B. Elberling[5], M. Leibman[6] and Y. Dvornikov[6]

[1] ZAMG, Hohe Warte 38, 1190 Wien, Austria

[2] Austrian Polar Research Institute, Althanstrae 14, 1090 Wien, Austria

[3] Vienna University of Technology, Gusshausstrasse 27-29, 1040 Wien, Austria

[4] Stockholm University, SE-106 91 Stockholm, Sweden

[5] University of Copenhagen, ster Voldgade 10, DK-1350 Copenhagen K, Denmark

[6] Russian Academy of Science, Earth Cryosphere Institute, Malygin Street 86, Tyumen 625000, Russia

Abstract

A circumpolar representative and consistent wetland map is required for a range of applications including modelling of permafrost properties as well as upscaling of carbon fluxes and pools. Synthetic Aperture Radar (SAR) data has already been shown to be suitable for wetland mapping, especially C-band ASAR GM data (1 km resolution). A circumpolar wetness classification map has been introduced in a previous study [*Widhalm et al.*, 2015]. With heterogeneity being a major challenge in the Arctic, higher spatial resolution products than GM are essential. In this study we therefore investigate the potential of this approach at site scale using ENVISAT ASAR WS data ($\sim$120 m resolution). These higher resolution ASAR WS maps have been produced for study sites representing different settings throughout the Arctic and compared to high resolution land cover maps. It can be shown that a medium resolution C-band SAR based wetness level map can be derived for tundra regions where no scattering due to tree trunks hampers the used method.

5.1 Introduction

A circumpolar representative and consistent wetland map is required for a range of applications spanning from upscaling of carbon fluxes and pools to climate modelling and wildlife habitat assessments. Currently available datasets lack sufficient accuracy and/or thematic detail in many regions of the Arctic.

A novel wetness level map has been described using Circumpolar ENVISAT ASAR GM backscatter (1km resolution, 500 m nominal resolution) data by *Widhalm et al.* [2015]. The data has been explored in subarctic and Arctic environments with special emphasis on spatial wetness patterns. It could be found that winter minimum backscatter values reflect vegetation physiognomy units of certain wetness regimes north of the tree line (as defined in *Walker et al.* [2005]). Low winter backscatter values are mostly found in areas vegetated by plant communities typically for wet regions in the tundra biome, due to low roughness and low volume scattering caused by the predominant vegetation and soils.

Flux studies often distinguish between three classes: dry, mixed and wet [*Parmentier*
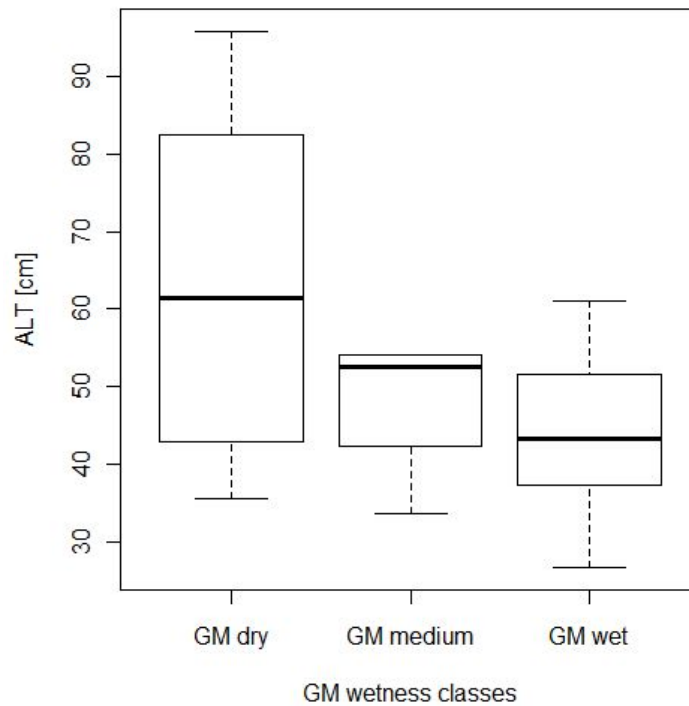
Figure 5.1: Active layer thickness (ALT) boxplot for CALM sites (Circumpolar Active Layer Monitoring, source: http://gtnp.arcticportal.org) for each ASAR GM derived wetness class north of the treeline (Figure 5.2).

et al., 2011]. It could be shown by *Widhalm et al.* [2015] that the ENVISAT ASAR GM derived wetness classes ('dry', 'medium', 'wet' and 'other', which is characterized by very low backscatter found at flat surfaced or sandy soils) are related to wetland classes of conventional vegetation maps, indicating its applicability. These wetness levels correspond also to active layer thickness north of the treeline (Figure 5.1).

In the Arctic heterogeneity is a major challenge. Hence higher resolution maps are required to face these challenges. We therefore test the introduced approach at site scale for ENVISAT ASAR WS data (∼120 m resolution, nominal resolution 75 m). We produced WS wetland maps and compare them to land cover maps or to in situ wetness observations for four different sites throughout the Arctic.
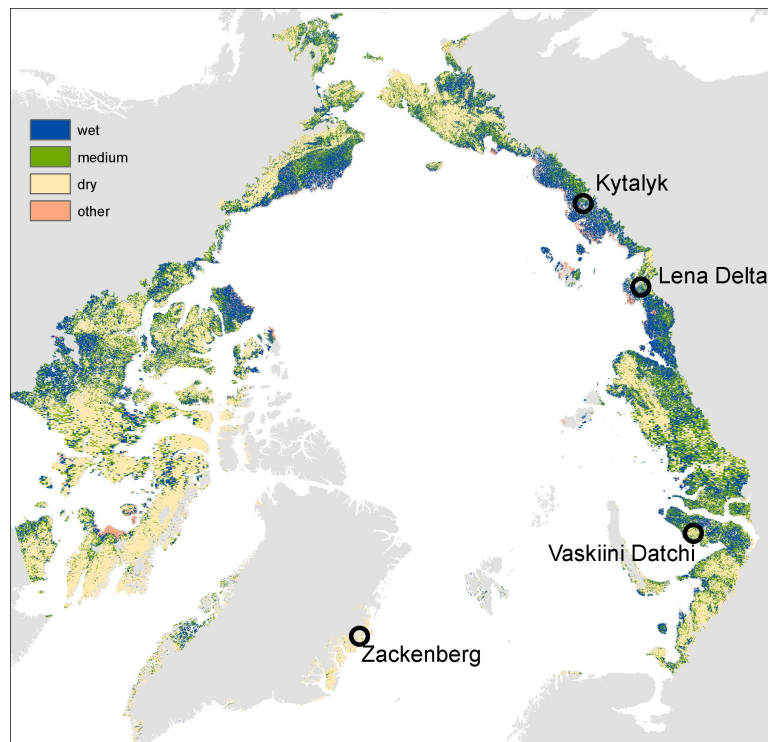
Figure 5.2: Location of study sites and ASAR GM wetness levels from *Widhalm et al.* [2015]

5.2 Data sets

5.2.1 Envisat ASAR

The Advanced Synthetic Aperture Radar (ASAR) instrument on board ESA's ENVISAT satellite operated in C-band (5.3 GHz) in five mutually exclusive modes with varying temporal and spatial resolution from 30 m to 1 km, from 2002 to spring 2012. Wide Swath (WS) and Global Monitoring Mode (GM) are ScanSAR Modes which provide images with a swath width of 405 km and incidence angles from 15° to 45°. While GM has a low resolution of 1 km, WS offers medium resolution images of ∼120 m resolution [*ESA*, 2004; *Closa et al.*, 2003]. In this study GM and WS data in HH polarisation was used.

5.2.2 Kytalyk land cover map

Kytalyk (70°49' N, 147°29' E, elevation 11m above sea level) is located in the NE Siberian tundra within the Sakha (Yakutia) Republic, Russia (Figure 5.2). The area is marked by three geomorphological units, which are Yedoma (permafrost) remnants, an alas (thermokarst depressions) plain, and a river floodplain. The alas plain is dominated by

low-centered polygons, whichs centers are covered by Sphagnum and sedge fen, while the dry elevated polygon rims and irregular frost mounds are covered by dwarf shrub fens. The land surface on the Yedoma remnants is characterized by well-drained tussock and nontussock tundra. The river floodplain is overgrown by 2 m high Salix bushes.

For the Kytalyk land cover map by *Siewert et al.* [2015], a GeoEye-1 (DigitalGlobe, 19 August 2010) satellite image covering 49 km^2 was used. The image has a 2 m nominal resolution and four spectral bands (blue, green, red, and near infrared). A supervised maximum likelihood classifier (ENVI 5.0, Boulder, Colorado) was used with the same probability for all classes. The study area was classified according to different land cover types identified in the field and classes were assigned according to different tundra types adapted from the CAVM classification system [*Walker et al.*, 2005]. Areas affected by cloud cover or cloud shadows, covering 7% of the entire study area, were masked out [*Siewert et al.*, 2015].

5.2.3 Zackenberg land cover map

The Zackenberg study site corresponds to the area surrounding the Zackenberg Research Station in NE Greenland (74°28'N, 20°34'W). The landscape is mountainous with a broad, flat central valley, where at least five major plant communities can be identified, which are closely related to differences in water availability. From the hilltops towards the depressions, there is an increase in soil water content from dry at the hilltops to wet conditions in the bottom of the depression [*Elberling et al.*, 2008]. Water saturated fen areas, wet to moist grasslands, heath vegetation in drier microhabitats, snowbed patches with long-persisting snow cover, scarce heath on dry and wind-exposed places, and areas of sparse or absent vegetation above 200-400 m elevation.

The land cover map by *Palmtag et al.* [2015] has a spatial resolution of 5 m resampled to 10 m x 10 m. The maximum-likelihood classification was carried out in ENVI 4.2 and based on an aerial hyperspectral HyMap campaign from 8 August 2000 and ground-truthing in the field during July 2005 [*Palmtag et al.*, 2015].

5.2.4 Lena Delta

The Lena River Delta, situated in Northern Siberia (72.0-73.8° N, 122.0-129.5° E), is the largest Arctic delta and covers 29,000 km^2. It is characterised by a network of small and large rivers and channels, and more than 1000 islands. The Lena Delta can be divided into three geomorphologically different terraces and active floodplain levels [*Are and Reimnitz*, 2000; *Schwamborn et al.*, 2002]. It is covered by tundra vegetation of various types. Major components are grasses, sedges, mosses, lichens, herbs, and dwarf shrubs [*Kutzbach et al.*, 2004].

The land cover map by *Schneider et al.* [2009] is based on three Landsat-7 Enhanced Thematic Mapper (ETM+) satellite images (acquisition dates 27 July 2000 and 26 July 2001) which were resampled to 30 m x 30 m pixels. A supervised classification was conducted using the minimum distance algorithm. Nine land cover classes characterised by their vegetation, surface moisture, and topography could be defined. The composition and distribution of non-water cover classes strongly varies for the three main river terraces. Whereas the first and the third terrace are dominated by moist to wet classes, the second terrace is dominated by classes indicating mainly dry conditions [*Schneider et al.*, 2009].

5.2.5 Vaskiny Dachi

The Vaskiny Dachi study area on the Yamal Peninsula in northwest Siberia is a hilly plain with narrow watersheds. It is dissected by narrow river valleys and gullies and located in a moss and lichen-dominated tundra [*Khomutov and Leibman*, 2014b].
In summer 2014 over 60 field points were recorded including position, wetness and vegetation information.

5.3 Methodology

For each of the study sites ASAR WS data was processed for at least one December acquisition of five years each (2007 - 2011). The software NEST (Next ESA SAR Toolbox) was used for Range-Doppler Terrain Correction using a circumpolar digital elevation model [*Santoro and Strozzi*, 2012] of 3" resolution (product of the DUE Permafrost project).
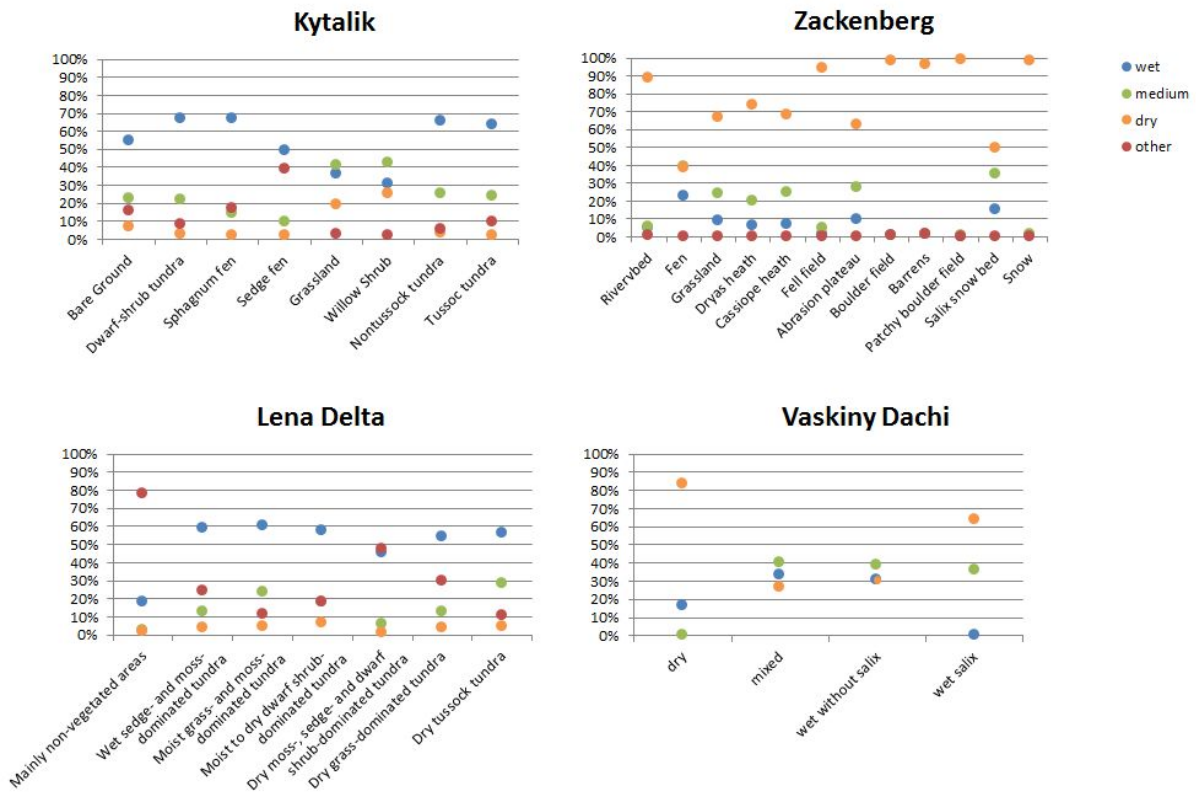
Figure 5.3: Percentage of WS wetness class pixels within site scale land cover maps and field points

Minimum backscatter values were calculated like in the study by *Widhalm et al.* [2015]. The resulting WS minimum backscatter images were then compared to the GM minimum backscatter image. Unlike the GM dataset, the WS data has not been corrected for the influence of local incidence angle. The lack of normalisation and the reduced number of processed data leads to offsets between the WS and GM dataset. These offsets have been quantified, corrected and thresholds applied as in *Widhalm et al.* [2015] to derive the classes 'dry', 'medium', 'wet' and 'other'.

For validation purposes the obtained WS wetness maps were then compared to the above described land cover maps and field points by extracting fractions of WS wetness class pixels within the land cover classes and field point classes. Furthermore the WS wetness maps were also compared to the GM product of *Widhalm et al.* [2015] in order to investigate scale differences.
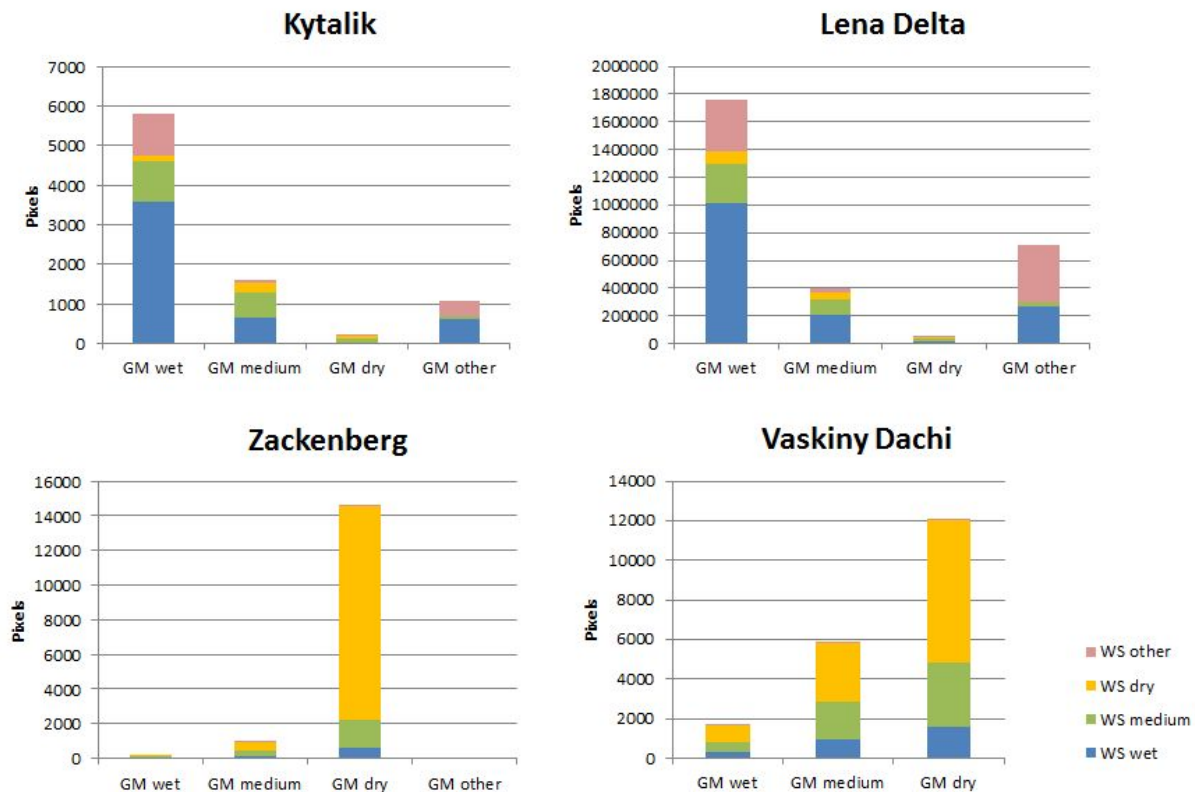
Figure 5.4: Number of WS wetness class pixels within GM wetness classes.

5.4 Results

The comparison of the WS wetness maps to the site scale land cover maps (see Figure 5.3) showed, that for Kytalik wet fen and dwarf-shrub classes corresponded to at least 50% of the class 'wet'. The grassland class related to about 40% of medium and 'wet' class pixels respectively.

Dry nontussock and tussock classes however did not match well with the WS wetness map showing over 60% 'wet' pixels. Similar results were achieved for the Lena Delta where wet land cover classes showed about 60% 'wet' pixels, but also dry classes experienced a percentage of 'wet' pixels of about 50. The Zackenberg study site features overall more dry pixels with the highest amount of 'wet' pixels (over 20%) in the water saturated fen class. The Vaskiny Dachi area showed highest percentages of 'dry' pixels at dry ground points, similar amounts of 'dry','medium', and 'wet' pixels at points with mixed wetness conditions and at wet points, which didn't feature dense salix cover. Wet points with dominant salix vegetation were mostly classified as 'dry'.

By comparing the WS to the GM wetness product (see Figure 5.4) it becomes apparent, that the percentage of 'wet' WS pixels decreases and the fraction of 'dry' WS pixel increases from wet to dry GM classes. However the overall corresponding WS classes do not necessarily prevail within each respective GM class. Especially the medium class consists of a mixture of all other classes (but with the sum of wet and medium >50%) in WS.

5.5 Discussion

5.5.1 Landcover comparison

The WS derived wet class dominates within the landcover types fen and sedge tundra. A rather high percentage of the wet class is found for dry landcover types (incl. tussock) at the Lena Delta as well as the Kytalyk site. Both sites are however wetland dominated and the proportion of the dry classes rather small. The classification as wetland might be also caused by the land cover heterogeneity.

Wet salix sites are classified as dry at the Vaskiny Dachi study site. The salix vegetation has there stem diameters of more than 5 cm and heights over 1.5 m (see Figure 5.5), which often feature higher soil moisture. Volume scattering leads to higher backscatter in these regions which are therefore wrongly classified as dry area. Most dry validation points that were correctly classified as 'dry' featured rough hummocky surfaces, which again lead to higher backscatter.

5.5.2 ASAR GM and WS comparison

Although the comparison of WS and GM wetness products showed that WS classes did not necessarily dominate within their respective GM counterparts, an increase of 'dry' and decrease of 'wet' WS pixels could be observed for 'wet' to 'dry' GM classes. The differences between the sites regarding their wetness (Figure 5.1) can be clearly captured across scales (Figure 5.4).

Figure 5.5: Salix vegetation at Vaskiny Dachy study site with lens cap (diameter 5.6 cm) as scale.

5.6 Conclusions

It could be shown that a medium resolution C-band SAR based wetness level map can be derived for tundra regions. Deviations were encountered for land cover types which are not exclusive for one wetness state. Furthermore the method is not applicable for regions where scattering due to tree trunks may occur.

Acknowledgements

Chapter 6

Additional Publication B

Classification of tundra regions with polarimetric TerraSAR-X data

Widhalm, B.[1], A. Bartsch[1,2], Achim Roth[3], and M. Leibman[4,5]

in press

[1] ZAMG - Zentralanstalt für Meteorologie und Geodynamik, Austria

[2] b.geos, Austria

[3] DLR - Deutsches Zentrum für Luft- und Raumfahrt, Germany

[4] Earth Cryosphere Institute, Tyumen Scientific Center, Russian Academy of Sciences, Siberian Branch, Russia

[5] University of Tyumen, Cryosophy Department, Russia

Abstract

Permafrost is an essential element of the cryosphere, which will be strongly affected by global warming. Although permafrost cannot be measured directly with remote sensing, many permafrost features are observable. Polarimetric information can be used in this context. Polarimetric data of TerraSAR-X is the basis for a local landcover classification presented here, which reflects different scattering mechanisms. The resulting classification aims on the identification of process areas and periglacial features such as thaw slumps (bare wet surfaces) and thaw lakes as well as wetland areas.

6.1   Introduction

Permafrost is a key element of the Cryosphere that will be strongly affected by a warming climate. It is therefore essential to monitor the permafrost state and to map the impacts of degradation and potential natural hazards on the ground [*Westermann et al.*, 2015a]. Permafrost cannot be directly detected from space, but many surface features of permafrost terrains and typical periglacial landforms are observable [*Trofaier et al.*, 2017]. This is addressed within the framework of the ESA DUE GlobPermafrost project. Earth Observation (EO) products are developed, validated and implemented to support research communities and international organisations in their work on better understanding permafrost.

In this study we present the delineation of permafrost land surface features derived from polarimetric TerraSAR-X data (HH/VV polarisation) within the GlobPermafrost project. It has been shown in a range of studies [*Ullmann et al.*, 2014; *Banks et al.*, 2013, 2014] that fully polarimetic information can be of high value for characterization of tundra surfaces. Such data are however mostly unavailable. More frequently acquired is dual pol information. The so called Kennaugh parameters can be derived from such data [*Schmitt et al.*, 2015]. Different scattering mechanisms can be separated. This plays a role for identification of disturbed tundra with ongoing permafrost degradation. These features are usually very small and can barely be detected with medium resolution data such as Landsat or Sentinel. X-band SAR data are available with higher spatial resolution. The aim of our investigation is to evaluate the potential of dual polarization X-band data for

Site	Date	Mode	Mean LIA
Vaskiny Dachi	27.08.2016	SpotLight	47.8°
Mackenzie Delta	11.08.2013	StripMap	31.6°
Herschel Island	27.08.2016	StripMap	23.4°

Table 6.1: Specifications of used TerraSAR-X calibration data (LIA local incidence angle)

identification of typical features of tundra landscapes. Special emphasis is on transferability of the classification approach across sites by accounting for different viewing geometries.

6.2   Data and study areas

Our analyses is based on the interpretation of polarimetric TerraSAR-X data (HH/VV polarisation). TerraSAR-X is a German national Synthetic Aperture Radar (SAR) satellite system with an 11-day repeat period. This high resolution X-band SAR has a center frequency of 9.65 GHz, corresponding to a wavelength of about 3.1 cm. 22 acquisitions from seven sites across the Arctic have been available. Three of the seven sites have been used for calibration. All sites are so called 'cold spots' which are locations where permafrost in situ monitoring has been taking place for many years or where field stations are currently established. In total 50 'cold spots' have been proposed to WMO Polar Space Task Group as focus areas for future monitoring by satellite data [*Bartsch et al.*, 2014]. Ground truth data have been collected during field campaigns in 2014, 2015 and 2016 on central Yamal, an area where landslides and lakes are very common and well documented [*Leibman et al.*, 2015].

In addition, Sentinel-2 NDVI images with 20 m spatial resolution have been used in the evaluation process. These NDVI images were derived from cloud masked Sentinel-2 data and represent mean values of July and August data of 2016 and 2017.

6.3   Methodology

All acquisitions have been orthorectified using Tandem-X elevation data and Kennaugh-elements retrieved. The scene from Vaskiny Dachi was acquired in SpotLight mode and processed to a nominal spatial resolution of 2.5m. All other scenes were of StripMap mode and sampled to 5m. In order to account for incidence angle dependent variations of the

TerraSAR-X data, the thresholds were derived as a function of the local incidence angle, which differed for each calibration scene (see Table 6.1).

The following Kennaugh-elements [*Schmitt et al.*, 2015]] were incorporated within the classification: total intensity of HH and VV (k0), ratio of even and odd bounce (k3) and ratio between HH and VV intensity (k4). For the delineation of class thresholds we derived probability density functions (pdfs; Figure 6.5) of sample polygons of each Kennaugh-element for the following three study sites:

Vaskiny Dachi on central Yamal in West Siberia (see Figure 6.2), Mackenzie Delta and Herschel Island in Northwest Canada. Sample polygons were defined based on field data, published maps and high resolution optical data. The following classes were to be differentiated: water, wetlands, bare surfaces (including e.g. thaw slumps), tundra, and other (including emerging vegetation, arctophila) (Figure 6.1).

Based on the pdfs it was decided which Kennaugh-element was best suited for the delineation of each landcover class. Thresholds were derived for each study site separately due to inherent differences caused by varying incidence angles. Incidence angle effects were compensated by delineating a linear function between incidence angle and threshold value. Landsurface feature maps were eventually calculated for all seven 'cold spot' sites. For each classification result NDVI mean values were calculated for every class and compared. Further validation was performed for the Vaskiny Dachi study site. A water classification derived from Sentinel-2 based on the 'fmask' algorithm [*Zhu et al.*, 2015] was compared to the water class. The class 'bare surface' was verified with three further known thaw slumps, whose polygons were extracted from a Sentinel-2 image. Furthermore the classified map was compared to field data collected in 2014.

6.4   Results and Discussion

The analyses of the polarimetric TerraSAR-X images revealed low backscatter values caused by specular reflection for both HH and VV images for water bodies under windless conditions. The class 'bare surface' featured high values for both polarisations similarly. The wetland class showed higher HH than VV backscatter values while the opposite mostly applied for the class 'other'.
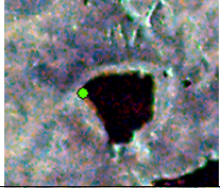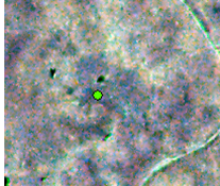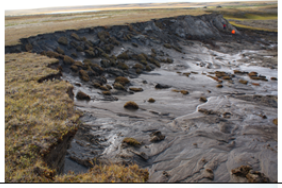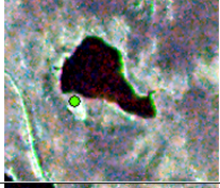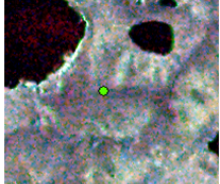
Figure 6.1: Landsurface feature classes with respective field photographs and HH and VV backscatter composite image (red: VV; green: k0, blue: HH; green circle indicates location of field photograph)

We analyzed the distributions of the pdfs (Figure 6.5) and the separability of different landcover classes for the Kennaugh-elements. Due to very low intensity values of water we derived the water class from the k0 parameter. Wetlands showed high values for the ratio between HH and VV intensity and were therefore delineated from the parameter k4. Bare wet surfaces like thermocirques or thaw slumps, which featured high total intensities and a low ratio value of even and odd bounce were consequently derived from a combination of k0 and k3. The remaining area was defined as tundra with the exception for regions with low k4 values, which were classified as other.

The analysis of the water class showed that 84% of the water class derived in Sentinel-2 were classified correctly for the Vaskiny Dachi study site (see Table 6.2). 6% were classified as tundra and other respectively. These discrepancies may arise from seasonal variances in water body extent as for the Sentinel-2 classification the maximal extent was used. Therefore also only less than 1% of the Sentinel-2 land area was classified as water with

class	water (S2)	no water (S2)
water	84.1%	0.6%
other	6.4%	13.3%
wetland	2.3%	11.5%
bare surface	0.9%	2.8%
tundra	6.4%	71.8%

Table 6.2: Comparison of polarimetric classification results at the Vaskiny Dachi study site with Sentinel-2 (S2) derived water classification.

class	# 1	# 2	# 3	# 1-3
other	0.0%	0.8%	0.9%	0.7%
wetland	0.9%	50.8%	45.8%	38.7%
bare surface	95.7%	23.2%	35.7%	42.5%
tundra	3.4%	25.2%	17.6%	18.2%

Table 6.3: Percentage of landcover classes contained within validation thaw slumps (corresponding to 'bare surface' class).

TerraSAR-X. For other sites the accuracy of the water classification may not be as high. Windy conditions hamper the correct classification of water bodies.

Evaluation of the bare surface class with three additional thaw slumps showed varying results, depending on site (see Table 6.3). For one site 96% of the thaw slump were classified correctly, while the worst result showed 23% correct classification and 51% wetland. All three sites combined featured 42% correct classification, 39% wetland and 18% tundra. This may result from the coarser resolution reference data (10m) as well as already re-established vegetation. These landslides were initiated already in 2012.

The comparison with field sample point data showed a correct classification of 76% of tundra points, while 19% were wrongly classified as wetland. Field points of wet regions were classified with 38% as wetland and 46% as tundra. Dryer tundra and wet areas are usually mixed within very short distances [*Widhalm et al.*, 2017] . There are also different types of wetlands which have not been distinguished at this stage.

6.5   Conclusions

Dual polarimetric X-band SAR derived Kennaugh data can provide classes with different scattering mechanisms in permafrost environments with very high spatial resolution.

Challenges include validation data collection which is appropriate regarding scale and up to date. The different incidence angle relationships of the investigated landcover types need to be considered for classification in order to ensure transferability. A remaining issue is windy conditions which cause roughening of water surfaces which cannot be distinguished using solely VV and HH as well as the diversity of wetland types in this environment.

Acknowledgements
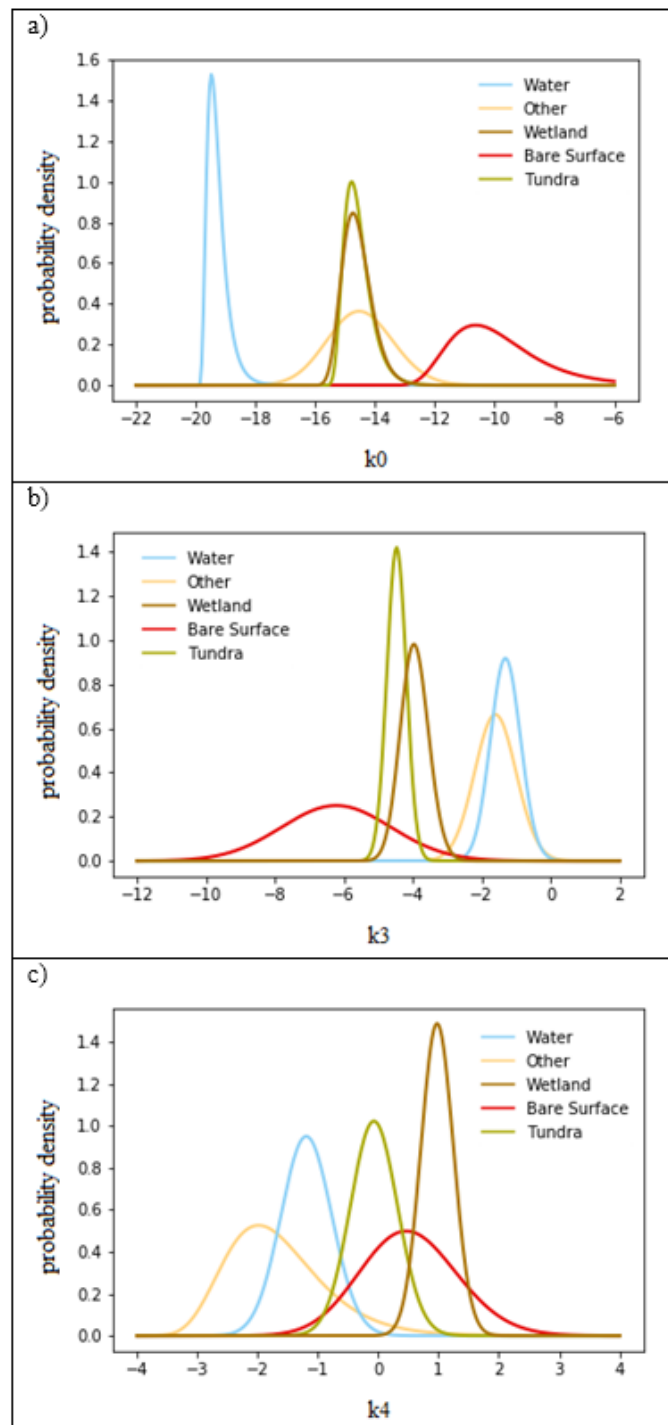
Figure 6.2: Probability density functions of landcover sample polygons for the Kennaugh-elements k0 (total intensity of HH and VV, figure a)), k3 (ratio of even and odd bounce, figure b)) and k4 (ratio between HH and VV intensity, figure c)), Vaskiny Dachi.
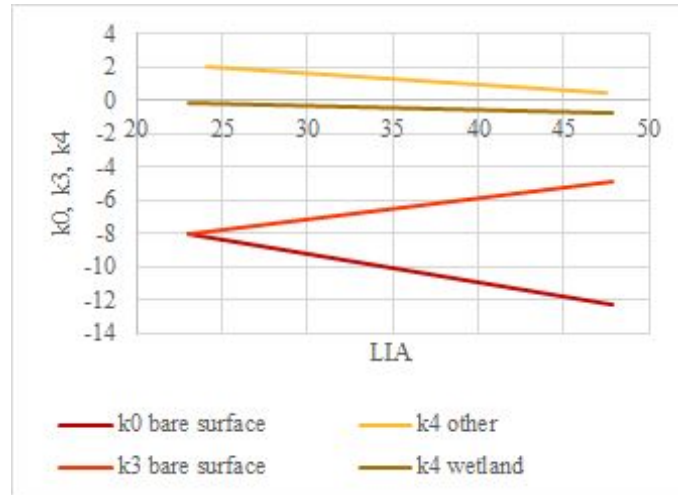
Figure 6.3: Linear functions between local incidence angle (LIA) and threshold values.
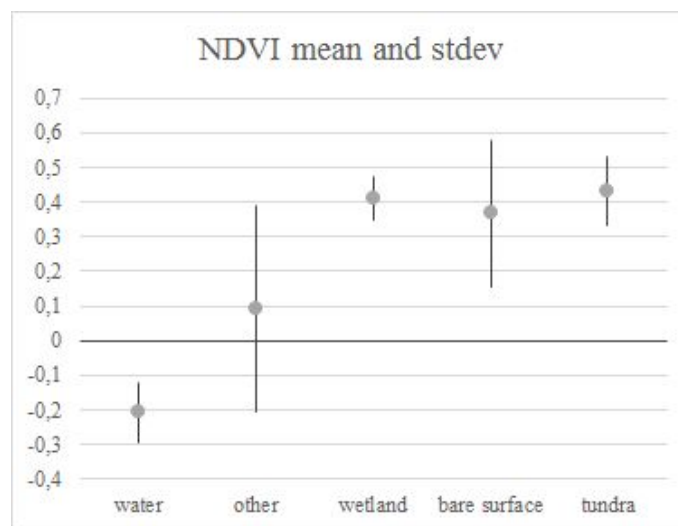
Figure 6.4: Mean and standard deviation of Sentinel-2 NDVI values for each landcover class for all processed sites.
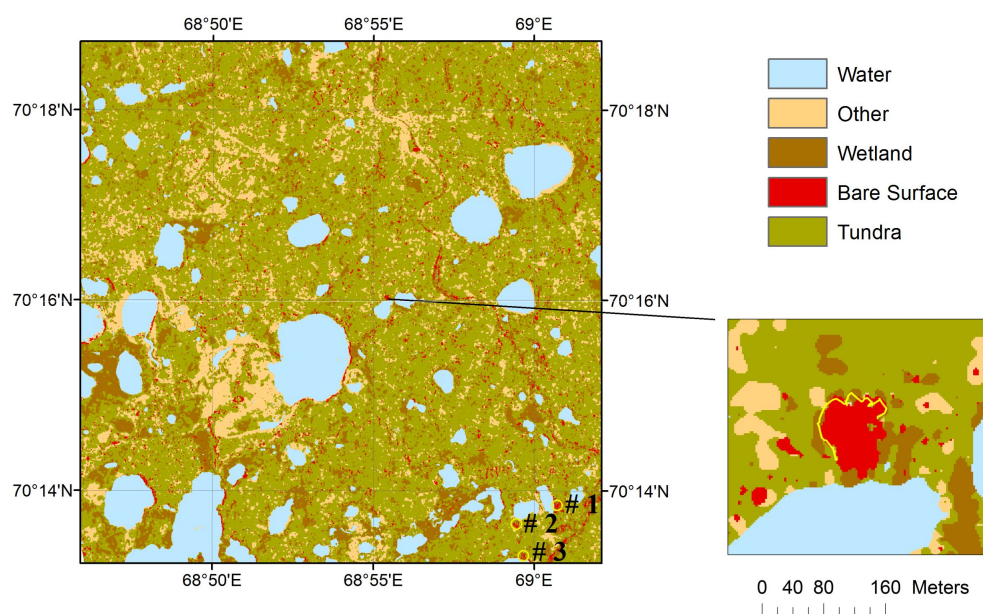
Figure 6.5: Landcover classification of Vaskiny Dachi study site area on central Yamal and subset of thaw slump with measured border (GPS) in yellow. Validation thaw slumps as specified in table 5 marked with yellow circles and numbers in south-east corner.

Bibliography

Alvarez-Mozos, J., J. Casali, M. Gonzalez-Audicana, and N. Verhoest, Correlation between ground measured soil moisture and RADARSAT-1 derived backscatter coefficient over an agricultural catchment of Navarre (North of Spain), *Biosystems Engineering*, *92*(1), 119–133, 2005.

Antonova, S., C. Duguay, A. Kääb, B. Heim, M. Langer, S. Westermann, and J. Boike, Monitoring ice phenology and bedfast ice in lakes of the Lena River Delta using TerraSAR-X backscatter and coherence time series, *Remote Sensing*, *8*, doi: 10.3390/rs8110903, 2016a.

Antonova, S., A. Kääb, B. Heim, M. Langer, and J. Boike, Spatio-temporal variability of X-band radar backscatter and coherence over the Lena River Delta, Siberia, *Remote Sensing of Environment*, *182*, 169–191, doi: 10.1016/j.rse.2016.05.003, 2016b.

Antonova, S., H. Sudhaus, T. Strozzi, S. Zwieback, A. Kääb, B. Heim, M. Langer, N. Bornemann, and J. Boike, Thaw subsidence of a Yedoma landscape in northern Siberia, measured in situ and estimated from TerraSAR-X interferometry, *Remote Sensing*, *10*, doi: 10.3390/rs10040494, 2018.

Are, F., and E. Reimnitz, An overview of the Lena Delta setting: Geology, tectonics, geomorphology, and hydrology, *Journal of Coastal Research*, *16*(4), 1083–1093, 2000.

Attema, E., et al., Sentinel-1: The radar mission for GMES operational land and sea services, *ESA Bulletin*, *131*, 10–17, 2007.

Banks, S., T. Ullmann, A. Roth, A. Schmitt, S. Dech, and D. King, Classification of Arctic coastal land covers with polarimetric SAR data, in *2013 IEEE Radar Conference (RadarCon13)*, pp. 1–6, doi: 10.1109/RADAR.2013.6586059, 2013.

Banks, S. N., D. J. King, A. Merzouki, and J. Duffe, Characterizing scattering behaviour and assessing potential for classification of Arctic shore and near-shore land covers with fine quad-pol RADARSAT-2 data, *Canadian Journal of Remote Sensing*, *40*(4), 291–314, doi: 10.1080/07038992.2014.979487, 2014.

Bartsch, A., Ten years of SeaWinds on QuikSCAT for snow applications, *Remote Sensing*, *2*, 1142–1156, doi: 10.3390/rs2041142, 2010.

Bartsch, A., C. Pathe, W. Wagner, and K. Scipal, Detection of permanent open water surfaces in central Siberia with ENVISAT ASAR wide swath data with special emphasis on the estimation of methane fluxes from tundra wetlands, *Hydrology Research*, *39*(2), 89–100, 2008.

Bartsch, A., W. Wagner, K. Scipal, C. Pathe, D. Sabel, and P. Wolski, Global monitoring of wetlands - the value of ENVISAT ASAR global mode, *Journal of Environmental Management*, *90*, 2226–2233, 2009.

Bartsch, A., D. Sabel, W. Wagner, and S.-E. Park, Considerations for derivation and use of soil moisture data from active microwave satellites at high altitudes, in *IEEE International Geoscience and Remote Sensing Symposium 2011*, 2011.

Bartsch, A., A.Trofaier, G. Hayman, D. Sabel, S. Schlaffer, D. Clark, and E. Blyth, Detection of open water dynamics with ENVISAT ASAR in support of land surface modelling at high latitudes, *Biogeosciences*, *9*, 703–714, 2012.

Bartsch, A., A. Höfler, C. Kroisleitner, and A. M. Trofaier, Land cover mapping in northern high latitude permafrost regions with satellite data: Achievements and remaining challenges, *Remote Sensing*, *8*(12), 979, doi: 10.3390/rs8120979, 2016a.

Bartsch, A., B. Widhalm, P. Kuhry, G. Hugelius, J. Palmtag, and M. B. Siewert, Can C-band synthetic aperture radar be used to estimate soil organic carbon storage in tundra?, *Biogeosciences*, *13*, 5453–5470, doi: 10.5194/bg-13-5453-2016, 2016b.

Bartsch, A., G. Pointner, M. O. Leibman, Y. A. Dvornikov, A. V. Khomutov, and A. M. Trofaier, Circumpolar mapping of ground-fast lake ice, *Front. Earth Sci.*, *5*, doi: 10.3389/feart.2017.00012, 2017.

Bartsch, A., et al., *Requirements for monitoring of permafrost in polar regions - A community white paper in response to the WMO Polar Space Task Group (PSTG)*, hdl:10013/ epic.45648.d001, 4th ed., 2014.

Bartsch, A., et al., Globpermafrost - how space-based earth observation supports understanding of permafrost., *Proceedings of the ESA Living Planet Symposium 2016*, p. 6, 2016c.

Baup, F., E. Mougin, P. Hiernaux, A. Lopes, P. D. Rosnay, and I. Chenerie, Radar signatures of Sahelian surfaces in Mali using ENVISAT-ASAR data, *IEEE Transactions on Geoscience and Remote Sensing*, *45*(7), 2354 – 2363, doi: 10.1109/TGRS.2007.893824, 2007.

Beck, I., R. Ludwig, M. Bernier, T. Strozzi, and J. Boike, Vertical movements of frost mounds in subarctic permafrost regions analyzed using geodetic survey and satellite interferometry, *Earth Surface Dynamics*, *3*, 409–421, doi: 10.5194/esurf-3-409-2015, 2015.

Bergstedt, H., and A. Bartsch, Surface state across scales; temporal and spatial patterns in land surface freeze/thaw dynamics, *Geosciences*, *7*, doi: 10.3390/geosciences7030065, 2017.

Bergstedt, H., S. Zwieback, A. Bartsch, and M. Leibman, Dependence of C-band backscatter on ground temperature, air temperature and snow depth in Arctic permafrost regions, *Remote Sensing*, *10*(142), doi: 10.3390/rs10010142, 2018.

Bicheron, P., P. Defourny, C. Brockmann, L. Schouten, C. Vancutsem, M. Huc, and S. Bontemps, Globcover: Products description and validation report, *Tech. rep.*, MEDI-ASFrance, Toulouse, 2008.

Blok, D., M. M. P. D. Heijmans, G. Schaepman-Strub, A. V. Kononov, T. C. Maximov, and F. Berendse, Shrub expansion may reduce summer permafrost thaw in Siberian tundra, *Global Change Biology*, *16*(4), 1296–1305, doi: 10.1111/j.1365-2486.2009.02110.x, 2010.

Bratsch, S., H. Epstein, M. Buchhorn, and D. Walker, Differentiating among four Arctic tundra plant communities at Ivotuk, Alaska using field spectroscopy, *Remote Sensing*, *8*(51), doi: 10.3390/rs8010051, 2016.

Brown, J., O. Ferrians Jr., J. Heginbottom, and E. Melnikov, US Geological Survey Circum-Pacific Map, 1997.

Brown, J., K. M. Hinkel, and F. E. Nelson, The circumpolar active layer monitoring (CALM) program: Research designs and initial results, *Polar Geography*, *24*(3), doi: 10.1080/10889370009377698, 2000.

CAVM Team, Circumpolar Arctic Vegetation Map. (1:7,500,000 scale), Conservation of Arctic Flora and Fauna (CAFF) Map No. 1., U.S. Fish and Wildlife Service, Anchorage, Alaska, 2003.

Chen, F., H. Lin, W. Zhou, T. Hong, and G. Wang, Surface deformation detected by ALOS PALSAR small baseline SAR interferometry over permafrost environment of Beiluhe section, Tibet Plateau, China, *Remote Sensing of Environment*, *138*, 10–18, 2013.

Closa, J., B. Rosich, and A. Monti-Guarnieri, The ASAR wide swath mode products, in *IEEE International Geoscience and Remote Sensing Symposium 2003*, vol. 2, pp. 1118–1120, IEEE, 2003.

DLR, TanDEM-X: Grround segment, DEM products specification document.

DLR, TerraSAR-X Missiom, brochure, 2009.

Domine, F., M. Barrere, and S. Morin, The growth of shrubs on high Arctic tundra at Bylot Island: impact on snow physical properties and permafrost thermal regime, *Biogeosciences Discussions*, doi: 10.5194/bg-2016-3, 2016.

Duguay, C., T. Zhang, D. Leverington, and V. Romanovsky, *Satellite Remote Sensing of Permafrost and Seasonally Frozen Ground*, pp. 91–118, American Geophysical Union (AGU), doi: 10.1029/163GM06, 2013.

Duguay, C. R., and P. M. Lafleur, Determining depth and ice thickness of shallow sub-Arctic lakes using space-borne optical and SAR data, *Int. J. Remote Sens.*, *24*(3), 475–489, 2003.

Duguay, Y., M. Bernier, E. Lévesque, and B. Tremblay, Potential of C and X band SAR for

shrub growth monitoring in sub-Arctic environments, *Remote Sensing*, *7*(7), 9410–9430, doi: 10.3390/rs70709410, 2015.

Durden, S. L., Z. S. Haddad, L. A. Morrissey, and G. P. Livingston, Classification of radar imagery over boreal regions for methane exchange studies, *International Journal of Remote Sensing*, *17*(6), 1267–1273, doi: 10.1080/01431169608949086, 1996.

Dvornikov, Y., A. Khomutov, D. Mullanurov, K. Ermokhina, A. Gubarkov, and M. Leibman, GIS and field data based modelling of snow water equivalent in shrub tundra, *Fennia*, *193*(1), 53–65, doi: 10.11143/46363, 2015.

Dvornikov, Y., et al., Geodatabase and WebGIS project for long-term permafrost monitoring at the Vaskiny Dachi research station, Yamal, Russia, *Polarforschung*, *85*(5), 107–115, doi: 10.2312/polfor.2016.007, 2016.

Elberling, B., et al., Soil and plant community-characteristics and dynamics at Zackenberg, *Advances in Ecological Research*, *40*, doi: 10.1016/S0065-2504(07)00010-4, 2008.

Engman, E., *Soil Moisture*, pp. 197–216, Berlin: Springer, 2000.

ESA, *ENVISAT ASAR Product Handbook*, European Space Agency, 2004.

ESA, ESA Climate Change Initiative description, EOP-SEP/TN/ 0030-09/SP, technical note, *Tech. rep.*, 2009.

Forbes, B. C., et al., Sea ice, rain-on-snow and tundra reindeer nomadism in Arctic Russia, *Biology Letters*, (12), doi: 10.1098/rsbl.2016.0466, 2016.

Frison, P.-L., and E. Mougin, Use of ERS-1 wind scatterometer data over land surfaces, *IEEE Geoscience and Remote Sensing Society*, *34*(2), 550 – 560, doi: 10.1109/36.485131, 1996.

Gangodagamage, C., et al., Extrapolating active layer thickness measurements across Arctic polygonal terrain using LiDAR and NDVI data sets, *Water Resources Research*, *50*, 6339–6357, doi: 10.1002/2013WR014283, 2014.

Gauthier, Y., M. Bernier, and J.-P. Fortin, Aspect and incidence angle sensitivity in ERS-1 SAR data, *International Journal of Remote Sensing*, *19*(10), 2001– 2006, doi: 10.1080/014311698215117, 1998.

Gomersall, C. E., and K. M. Hinkel, Estimating the variability of active-layer thaw depth in two physiographic regions of northern Alaska, *Geographical Analysis*, *33*(2), 141–155, 2001.

Gross, M. F., M. A. Hardisky, J. A. Doolittle, and V. Klemas, Relationships among depth to frozen soil, soil wetness, and vegetation type and biomass in tundra near Bethel, Alaska, U.S.A., *Arctic and Alpine Research*, *22*(3), 275–282, doi: 10.1080/00040851.1990. 12002791, 1990.

Grosse, G., et al., Vulnerability of high-latitude soil organic carbon in North America to disturbance, *Journal of Geophysical Research Biogeosciences*, *116*, 2011.

Hachem, S., M. Allard, and C. Duguay, Using the MODIS land surface temperature product for mapping permafrost: an application to northern Québec and Labrador, Canada, *Permafrost and Periglacial Processes*, *20*, doi: 10.1002/ppp.672, 2009.

Harlan, R., and J. F. Nixon, *Geotechnical engineering for cold regions*, chap. Ground thermal regime, pp. 103–163, McGraw-Hill Book Co., New York, N.Y., United States, 1978.

Harris, S., H. French, J. Heginbottom, G. Johnston, B. Ladanyi, D. Sego, and R. van Everdingen, Glossary of permafrost and related ground-ice terms, *National Research Council of Canada, Ottawa. Technical Memorandum 142*, 1988.

Hinkel, K. M., and F. E. Nelson, Spatial and temporal patterns of active-layer thickness at Circumpolar Active-Layer Monitoring (CALM) sites in Northern Alaska, 1995-2000, *Journal of Geophysical Research*, *108*(D2), doi: 10.1029/2001JD000927, 2003.

Högström, E., A. M. Trofaier, I. Gouttevin, and A. Bartsch, Assessing seasonal backscatter variations with respect to uncertainties in soil moisture retrieval in Siberian tundra regions, *Remote Sensing*, *6*, 8718–8738, doi: 10.3390/rs6098718, 2014.

Huggett, R. J., *Fundamentals of Geomorphology*, 2 ed., Routledge, 2007.

IPCC, *Climate Change 2013: The Physical Science Basis. Contribution of Working Group I to the Fifth Assessment Report of the Intergovernmental Panel on Climate Change*, 996 pp., Cambridge University Press, Cambridge, United Kingdom and New York, NY, USA, doi: 10.1017/CBO9781107415324, 2013.

Jeffries, M., K. Morris, and G. Liston, A method to determine lake depth and water availability on the North Slope of Alaska with spaceborne imaging radar and numerical ice growth modelling, *ARCTIC*, *49*(4), 367–374, doi: 10.14430/arctic1212, 1996.

Jeffries, M. O., M. Kim, and K. Nickolai, *Ice Characteristics and Processes, and Remote Sensing of Frozen Rivers and Lakes*, pp. 63–90, American Geophysical Union (AGU), doi: 10.1029/163GM05, 2013.

Jones, B., G. Grosse, K. M. Hinkel, C. Arp, S. Walker, R. Beck, and J. P. Galloway, Assessment of pingo distribution and morphometry using an IfSAR derived digital surface model, western Arctic Coastal Plain, Northern Alaska, *Geomorphology*, *138*, 1–14, 2012.

Jones, B. M., G. Grosse, C. D. Arp, M. C. Jones, A. K. M. Walter, and V. E. Romanovsky, Modern thermokarst lake dynamics in the continuous permafrost zone, northern Seward Peninsula, Alaska, *Journal of Geophysical Research: Biogeosciences*, *116*(G2), doi: 10.1029/2011JG001666, 2011.

Jorgenson, M. T., and M. Heiner, Ecosystems of Northern Alaska. Unpublished 1:2.5 million-scale map produced by ABR, Inc., 2003.

Kane, D. L., L. D. Hinzman, and J. Zarling, Thermal response of the active layer to climatic warming in a permafrost environment, *Cold Regions Science and Technology*, *19*(2), doi: 10.1016/0165-232X(91)90002-X, 1991.

Kelley, A. M., H. E. Epstein, and D. A. Walker, Role of vegetation and climate in permafrost active layer depth in arctic tundra of northern Alaska and Canada, *Journal of Glaciology and Climatology*, *26*, 269–273, 2004.

Kerr, Y. H., P. Waldteufel, J. P. Wigneron, J. Martinuzzi, J. Font, and M. Berger, Soil moisture retrieval from space: the Soil Moisture and Ocean Salinity (SMOS)

mission, *IEEE Transactions on Geoscience and Remote Sensing*, *39*(8), 1729–1735, doi: 10.1109/36.942551, 2001.

Khomutov, A., and M. Leibman, *Landslides in Cold Regions in the Context of Climate Change*, chap. Assessment of Landslide Hazards in a Typical Tundra of Central Yamal, Russia, pp. 271–290, Springer International Publishing, doi: 10.1007/978-3-319-00867-7_ 20, 2014a.

Khomutov, A., and M. Leibman, *Assessment of Landslide Hazards in a Typical Tundra of Central Yamal, Russia*, pp. 271–290, Springer International Publishing, Cham, doi: 10.1007/978-3-319-00867-7_20, 2014b.

Koven, C. D., B. Ringeval, P. Friedlingstein, P. Ciais, P. Cadule, D. Khvorostyanov, G. Krinner, and C. Tarnocai, Permafrost carbon-climate feedbacks accelerate global warming, *Proceedings of the National Academy of Sciences*, *108*(36), 14,769–14,774, doi: 10.1073/pnas.1103910108, 2011.

Krankina, O. N., D. Pflugmacher, D. J. Hayes, A. D. McGuire, M. C. Hansen, T. Häme, V. Elsakov, and P. Nelson, *Vegetation Cover in the Eurasian Arctic: Distribution, Monitoring, and Role in Carbon Cycling*, pp. 79–108, Springer Netherlands, Dordrecht, doi: 10.1007/978-90-481-9118-5_5, 2011.

Krieger, G., A. Moreira, H. Fiedler, I. Hajnsek, M. Werner, M. Younis, and M. Zink, TanDEM-X: A satellite formation for high-resolution SAR interferometry, *IEEE Trans. Geosci. Remote Sens.*, *45*(11), doi: 10.1109/TGRS.2007.900693, 2007.

Kropacek, J., and G. D. Grandi, Wetlands mapping in Siberia by classification of the GBFM radar mosaic using backscatter and terrain topographic features, in *Proceedings of the Conference GlobWetland: Looking at Wetlands from Space*, edited by H. Lacoste, ESA Publications Division, 2006.

Kudryavtsev, V. A., L. Garagulia, K. A. Kondratyeva, and V. G. Melamed, Fundamentals of frost forecasting in geological engineering investigations, Nauka, Moscow. Draft translation 606, Cold Regions Research And Engineering Lab Hanover N H, 1974.

Kumpula, T., B. C. Forbes, F. Stammler, and N. Meschtyb, Dynamics of a coupled system: Multi-resolution remote sensing in assessing social-ecological responses during 25 years of gas field development in Arctic Russia, *Remote Sensing*, *4*, 1046–1068, 2012.

Kutzbach, L., D. Wagner, and E.-M. Pfeiffer, Effect of microrelief and vegetation on methane emission from wet polygonal tundra, Lena Delta, Northern Siberia, *Biogeochemistry*, *69*(3), doi: 10.1023/B:BIOG.0000031053.81520.db, 2004.

Lawrence, D. M., and S. C. Swenson, Permafrost response to increasing Arctic shrub abundance depends on the relative influence of shrubs on local soil cooling versus large-scale climate warming, *Environmental Research Letters*, *6*(4), doi: 10.1088/1748-9326/6/4/045504, 2011.

Lehner, B., and P. Döll, Development and validation of a global database of lakes, reservoirs and wetlands, *Journal of Hydrology*, *296*, 1–22, 2004.

Leibman, M., N. Moskalenko, P. Orekhov, A. Khomutov, I. Gameev, O. Khitun, D. Walker, and H. Epstein, *Polar cryosphere of water and land*, chap. Interrelation of cryogenic and biotic components of geosystems in cryolithozone of West Siberia on the Transect "Yamal", pp. 171–192, Paulsen Publisher, Moscow, 2011.

Leibman, M., A. Khomutov, P. Orekhov, O. Khitun, H. Epstein, G. Frost, and D. Walker, Gradient of seasonal thaw depth along the yamal transect, in *Proceedings of the tenth international conference on permafrost; translation of Russian contributions*, vol. 10(2), edited by V. Melnikov, D. Drozdov, and V. Romanovksy, pp. 237–242, 2012.

Leibman, M., A. Khomutov, A. Gubarkov, D. Mullanurov, and Y. Dvornikov, The research station "Vaskiny Dachi" Central Yamal, West Siberia, Russia - A review of 25 years of permafrost studies, *Fennia*, *193*(1), 3–30, doi: 10.11143/45201, 2015.

Leibman, M. O., Thaw depth measurements in marine sailne sandy and clayey deposits of Yamal peninsula, Russia: procedure and interpretation of results, in *PERMAFROST - Seventh International Conference (Proceedings), Yellowknife (Canada), Collection Nordicana*, 55, pp. 635–639, 1998.

Lemieux, J.-M., R. Fortier, M.-C. Talbot-Poulin, J. Molson, R. Therrien, M. Ouellet, D. Banville, M. Coch, and R. Murray, Groundwater occurrence in cold environments: examples from Nunavik, Canada, *Hydrology Journal*, *24*, 1497–1513, doi: 10.1007/s10040-016-1411-1, 2016.

Leverington, D. W., and C. R. Duguay, Evaluation of three supervised classifiers in mapping "depth to late-summer frozen ground," Central Yukon Territory, *Canadian Journal of Remote Sensing*, *22*(2), doi: 10.1080/07038992.1996.10874650, 1996.

Liu, L., T. Zhang, and J. Wahr, InSAR measurements of surface deformation over permafrost on the North Slope of Alaska, *Journal of Geophysical Research*, *115*, doi: 10.1029/2009JF001547, 2010.

Liu, L., E. E. Jafarov, K. M. Schaefer, B. M. Jones, H. A. Zebker, C. A. Williams, J. Rogan, and T. Zhang, InSAR detects increase in surface subsidence caused by an Arctic tundra fire, *Geophysical Research Letters*, *41*(11), 3906–3913, doi: 10.1002/2014GL060533, 2014.

Loew, A., R. Ludwig, and W. Mauser, Derivation of surface soil moisture from ENVISAT ASAR wide swath and image mode data in agricultural areas, *IEEE Transactions on Geoscience and Remote Sensing*, *44*(4), 889 – 899, doi: 10.1109/TGRS.2005.863858, 2006.

Mäkynen, M. P., A. T. Manninen, M. H. Similä, J. A. Karvonen, and M. T. Hallikainen, Incidence angle dependence of the statistical properties of C-band HH-polarization backscattering signatures of the Baltic sea ice, *IEEE Geoscience and Remote Sensing Society*, *40*(12), 2593 – 2605, doi: 10.1109/TGRS.2002.806991, 2002.

McMichael, C. E., A. S. Hope, D. A. Stow, and J. B. Fleming, The relation between active layer depth and a spectral vegetation index in arctic tundra landscapes of the North Slope of Alaska, *International Journal of Remote Sensing*, *18*(11), doi: 10.1080/014311697217666, 1997.

Melnikov, E. S., M. O. Leibman, N. G. Moskalenko, and A. A. Vasiliev, Active-layer monitoring in the cryolithozone of West Siberia, *Polar Geography*, *28*(4), 267–285, doi: 10.1080/789610206, 2004.

Menges, C. H., J. J. V. Zyl, G. J. E. Hill, and W. Ahmad, A procedure for the correction of the effect of variation in incidence angle on AIRSAR data, *International Journal of Remote Sensing*, *22*(5), 829– 841, doi: 10.1080/01431160051060264, 2001.

Mladenova, I. E., T. J. Jackson, R. Bindlish, and S. Hensley, Incidence angle normalization of radar backscatter data, *IEEE Transactions on Geoscience and Remote Sensing*, *51*(3), 1791 – 1804, doi: 10.1109/TGRS.2012.2205264, 2013.

Moran, M. S., D. C. Hymer, J. Qi, and E. E. Sano, Soil moisture evaluation using multi-temporal synthetic aperture radar (SAR) in semiarid rangeland, *Agricultural and Forest Meteorology*, *105*(1), 69 – 80, doi: https://doi.org/10.1016/S0168-1923(00)00189-1, 2000.

Morrissey, L. A., S. L. Durden, G. P. Livingston, J. A. Stearn, and L. S. Guild, Differentiating methane source areas in Arctic environments with multitemporal ERS-1 SAR data, *IEEE Transactions on Geoscience and Remote Sensing*, *34*(3), 667–673, 1996.

Mougin, E., A. Lopes, P. L. Frison, and C. Proisy, Preliminary analysis of ERS-1 wind scatterometer data over land surfaces, *International Journal of Remote Sensing*, *16*(2), 391–398, doi: 10.1080/01431169508954406, 1995.

Muster, S., M. Langer, B. Heim, S. Westermann, and J. Boike, Subpixel heterogeneity of ice-wedge polygonal tundra: a multi-scale analysis of land cover and evapotranspiration in the Lena River Delta, Siberia, *Tellus B: Chemical and Physical Meteorology*, *64*, doi: 10.3402/tellusb.v64i0.17301, 2012.

Muster, S., M. Langer, B. Heim, S. Westermann, and J. Boike, Landsat subpixel water cover of Lena River Delta, Siberia, with link to ESRI grid files, PANGAEA, doi: 10.1594/ PANGAEA.786926, in supplement to: Muster, S et al. (2012): Subpixel heterogeneity of ice-wedge polygonal tundra: a multi-scale analysis of land cover and evapotranspiration in the Lena River Delta, Siberia. Tellus Series B-Chemical and Physical Meteorology, 64, 17301, https://doi.org/10.3402/tellusb.v64i0.17301, 2012.

Muster, S., B. Heim, A. Abnizova, and J. Boike, Water body distributions across scales: A remote sensing based comparison of three Arctic tundra wetlands, *Remote Sensing*, pp. 1498–1523, doi: 10.3390/rs5041498, 2013.

Myers-Smith, I. H., and D. S. Hik, Shrub canopies influence soil temperatures but not nutrient dynamics: An experimental test of tundra snow-shrub interactions, *Ecology and Evolution*, *3*(11), 3683–3700, doi: 10.1002/ece3.710, 2013.

Naeimi, V., Z. Bartalis, and W. Wagner, ASCAT soil moisture: An assessment of the data quality and consistency with the ERS scatterometer heritage, *Journal of Hydrometeorology*, *10*, 555–563, 2009a.

Naeimi, V., K. Scipal, Z. Bartalis, S. Hasenauer, and W. Wagner, An improved soil moisture retrieval algorithm for ERS and METOP scatterometer observations, *IEEE Transactions on Geoscience and Remote Sensing*, 2009b.

Naeimi, V., C. Paulik, A. Bartsch, W. Wagner, R. Kidd, J. Boike, and K. Elger, ASCAT Surface State Flag (SSF): Extracting information on surface freeze/thaw conditions from backscatter data using an empirical threshold-analysis algorithm, *IEEE Transactions on Geoscience and Remote Sensing*, *50*(7), 2566 – 2582, doi: 10.1109/TGRS.2011.2177667, 2012.

Nelson, F. E., N. I. Shiklomanov, G. R. Mueller, K. M. Hinkel, D. A. Walker, and J. G. Bockheim, Estimating active-layer thickness over a large region: Kuparuk river basin, alaska, u.s.a., *Arctic and Alpine Research*, *29*(4), doi: 10.2307/1551985, 1997.

Njoku, E., AMSR-E/Aqua daily l3 surface soil moisture, interpretive parameters, & QC EASE-Grids, version 2, Boulder, Colorado USA. NASA National Snow and Ice Data Center Distributed Active Archive Center, doi: 10.5067/AMSR-E/AE_LAND3.002., 2004.

Olthof, I., R. Latifovic, and D. Pouliot, Development of a circa 2000 land cover map of northern Canada at 30 m resolution from Landsat, *Canadian Journal of Remote Sensing*, *35*(2), 152–165, doi: 10.5589/m09-007, 2009.

Ottlé, C., J. Lescure, F. Maignan, B. Poulter, T. Wang, and N. Delbart, Use of various remote sensing land cover products for plant functional type mapping over Siberia, *Earth System Science Data*, *5*(2), 331–348, doi: 10.5194/essd-5-331-2013, 2013.

Palmtag, J., G. Hugelius, N. Lashchinskiy, M. P. Tamstorf, A. Richter, B. Elberling, and P. Kuhry, Storage, landscape distribution, and burial history of soil organic matter in contrasting areas of continuous permafrost, *Arctic Antarctic and Alpine Research*, *47*(1), 71–88, doi: 10.1657/AAAR0014-027, 2015.

Park, S.-E., A. Bartsch, D. Sabel, W. Wagner, V. Naeimi, and Y. Yamaguchi, Monitoring Freeze/Thaw cycles using ENVISAT ASAR global mode, *Remote Sensing of Environment*, *115*, 3457–3467, 2011.

Parmentier, F. J. W., J. van Huissteden, M. K. van der Molen, G. Schaepman-Strub, S. A. Karsanaev, T. C. Maximov, and A. J. Dolman, Spatial and temporal dynamics in eddy covariance observations of methane fluxes at a tundra site in northeastern Siberia, *Journal of Geophysical Research*, *116*(G3), doi: 10.1029/2010JG001637, 2011.

Pathe, C., W. Wagner, D. Sabel, M. Doubkova, and J. B. Basara, Using ENVISAT ASAR global mode data for surface soil moisture retrieval over Oklahoma, USA, *IEEE Transactions on Geoscience and Remote Sensing*, *47*(2), 468–480, doi: 10.1109/TGRS.2008.2004711, 2009.

Pearson, R. G., S. J. Phillips, M. M. Loranty, P. S. A. Beck, T. Damoulas, S. J. Knight, and G. S. J., Shifts in arctic vegetation and associated feedbacks under climate change, *Nature Climate Change*, *3*, doi: 10.1038/nclimate1858, 2013.

Peddle, D. R., and S. E. Franklin, Classification of permafrost active layer depth from remotely sensed and topographic evidence, *Remote Sensing of Environment*, *44*(1), doi: 10.1016/0034-4257(93)90103-5, 1993.

Permafrost Subcommittee, Associate Committee on Geotechnical Research, Glossary of permafrost and related ground-ice terms, *National Research Council of Canada, Ottawa. Technical Memorandum*, (142), 1988.

Pflugmacher, D., et al., Comparison and assessment of coarse resolution land cover maps for Northern Eurasia, *Remote Sensing of Environment*, *115*(12), 3539 – 3553, doi: https://doi.org/10.1016/j.rse.2011.08.016, 2011.

Potin, P., *Sentinel-1 User Handbook*, ESA, issue 1, rev 0 ed., 2013.

Prigent, C., F. Papa, F. Aires, W. Rossow, and E. Matthews, Global inundation dynamics inferred from multiple satellite observations, 1993-2000, *Journal of Geophysical Research: Atmospheres*, *112*(D12), doi: 10.1029/2006JD007847, 2007.

Quebec Ministry of Natural Resources, Vegetation zones and bioclimatic domains of the Quebec province, Quebec Ministry of Natural Resources, 2003.

Raynolds, M. K., and D. A. Walker, Increased wetness confounds Landsat-derived NDVI trends in the central Alaska North Slope region, 1985-2011, *Environmental Research Letters*, *11*(8), 2016.

Regmi, P., G. Grosse, M. Jones, B. Jones, and K. Anthony, Characterizing post-drainage succession in thermokarst lake basins on the Seward Peninsula, Alaska with TerraSAR-X backscatter and Landsat-based NDVI data, *Remote Sensing*, *4*(12), 3741–3765, doi: 10.3390/rs4123741, 2012.

Reschke, J., A. Bartsch, S. Schlaffer, and D. Schepaschenko, Capability of C-Band SAR for operational wetland monitoring at high latitudes, *Remote Sensing*, *4*, 2923–2943, 2012.

Ringeval, B., N. de Noblet-Ducoudre, P. Ciais, P. Bousquet, C. Prigent, F. Papa, and W. B. Rossow, An attempt to quantify the impact of changes in wetland extent on methane emissions on the seasonal and interannual time scales, *Global Biogeochemical Cycles*, *24*, GB2003, 2010.

Romanovsky, V. E., S. L. Smith, and H. H. Christiansen, Permafrost thermal state in the polar Northern Hemisphere during the International Polar Year 2007-2009: A synthesis, *Permafrost Periglacial Processes*, *21*, 106–116, 2010.

Sabel, D., C. Pathe, W. Wagner, S. Hasenauer, A. Bartsch, C. Künzer, and K. Scipal, Using ENVISAT ScanSAR data for characterizing scaling properties of scatterometer derived soil moisture information over southern Africa, in *Proceedings of the ENVISAT Symposium, Montreux*, 2007.

Sabel, D., Z. Bartalis, W. Wagner, M. Doubkova, and J.-P. Klein, Development of a global backscatter model in support to the sentinel-1 mission design, *Remote Sensing*

of Environment, *120*, 102 – 112, doi: 10.1016/j.rse.2011.09.028, the Sentinel Missions - New Opportunities for Science, 2012.

Santoro, M., and T. Strozzi, Circumpolar digital elevation models >55° n with links to geotiff images., PANGAEA, doi: 10.1594/PANGAEA.779748, 2012.

Sazonova, T. S., and V. E. Romanovsky, A model for regional-scale estimation of temporal and spatial variability of active layer thickness and mean annual ground temperatures, *Permafrost and Periglacial Processes*, *14*(2), 125–139, doi: 10.1002/ppp.449, 2003.

Schaefer, K., T. Zhang, L. Bruhwiler, and A. P. Barrett, Amount and timing of permafrost carbon release in response to climate warming, *Tellus Series B: Chemical and Pysical Meteorology*, *63*(2), 165–180, doi: 10.1111/j.1600-0889.2011.00527.x, 2011.

Schaefer, K., et al., Remotely Sensed Active Layer Thickness (ReSALT) at Barrow, Alaska using interferometric synthetic aperture radar, *Remote Sensing*, *7*(4), 3735–3759, doi: 10.3390/rs70403735, 2015.

Schmitt, A., A. Wendleder, and S. Hinz, The Kennaugh element framework for multi-scale, multi-polarized, multi-temporal and multi-frequency SAR image preparation, *ISPRS Journal of Photogrammetry and Remote Sensing*, *102*, 122 – 139, doi: 10.1016/j.isprsjprs. 2015.01.007, 2015.

Schneider, J., G. Grosse, and D. Wagner, Land cover classification of tundra environments in the Arctic Lena Delta based on Landsat 7 ETM+ data and its application for upscaling of methane emissions, *Remote Sensing of Environment*, *113*(2), 380, doi: 10.1016/j.rse.2008.10.013, 2009.

Schroeder, R., M. A. Rawlins, K. C. McDonald, E. Podest, R. Zimmermann, and M. Kueppers, Satellite microwave remote sensing of North Eurasian inundation dynamics: development of coarse-resolution products and comparison with high-resolution synthetic aperture radar data, *Environmental Research Letters*, *5*, 015,003, 2010.

Schuur, E. A. G., et al., Climate change and the permafrost carbon feedback, *Nature*, *520*(7546), 171–179, 2015.

Schwamborn, G., V. Rachold, and M. N. Grigoriev, Late Quaternary sedimentation history of the Lena Delta, *Quaternary International*, *89*(1), doi: 10.1016/S1040-6182(01)00084-2, 2002.

Shiklomanov, N. I., and F. E. Nelson, Analytic representation of the active layer thickness field, Kuparuk River Basin, Alaska, *Ecological Modelling*, *123*(2-3), doi: 10.1016/S0304-3800(99)00127-1, 1999.

Shiklomanov, N. I., D. A. Streletskiy, F. E. Nelson, R. D. Hollister, V. E. Romanovsky, C. E. Tweedie, J. G. Bockheim, and J. Brown, Decadal variations of active-layer thickness in moisture-controlled landscapes, Barrow, Alaska, *Journal of Geophysical Research*, *115*(G00I04), doi: 10.1029/2009JG001248, 2010.

Siewert, M. B., J. Hanisch, N. Weiss, P. Kuhry, T. C. Maximov, and G. Hugelius, Comparing carbon storage of Siberian tundra and taiga permafrost ecosystems at very high spatial resolution, *Journal of Geophysical Research: Biogeosciences*, *120*(10), 1973–1944, doi: 10.1002/2015JG002999, 2015.

Smith, M., Potential responses of permafrost to climatic change, *Journal of Cold Regions Engineering*, *4*(1), 29–37, 1990.

Stettner, S., A. Beamish, A. Bartsch, B. Heim, G. Grosse, A. Roth, and H. Lantuit, Monitoring inter- and intra-seasonal dynamics of rapidly degrading ice-rich permafrost riverbanks in the Lena Delta with TerraSAR-X time series, *Remote Sensing*, *10*, 51, 2017.

Surdu, C. M., C. R. Duguay, L. C. Brown, and D. Fernández Prieto, Response of ice cover on shallow lakes of the North Slope of Alaska to contemporary climate conditions (1950-2011): radar remote-sensing and numerical modeling data analysis, *The Cryosphere*, *8*(1), 167–180, doi: 10.5194/tc-8-167-2014, 2014.

Torres, R., et al., GMES Sentinel-1 mission, *Remote Sensing of Environment*, *120*, 9–24, 2012.

Trofaier, A. M., S. Westermann, and A. Bartsch, Progress in space-borne studies of permafrost for climate science: Towards a multi-ECV approach, *Remote Sensing of Envi-

ronment, 203(Supplement C), 55 – 70, doi: 10.1016/j.rse.2017.05.021, earth Observation of Essential Climate Variables, 2017.

Ulaby, F. T., R. K. Moore, and A. Fung, *Microwave Remote Sensing–Active and Passive*, vol. II, Artech House, Norwood, Mass., 1982.

Ullmann, T., A. Schmitt, A. Roth, J. Duffe, S. Dech, H.-W. Hubberten, and R. Baumhauer, Land cover characterization and classification of Arctic tundra environments by means of polarized synthetic aperture X- and C-band radar (PolSAR) and Landsat 8 Multispectral Imagery - Richards Island, Canada, *Remote Sensing, 6*(9), 8565–8593, doi: 10.3390/ rs6098565, 2014.

Van Doninck, J., W. Wagner, T. Melzer, B. D. Baets, and N. E. C. Verhoest, Seasonality in the angular dependence of ASAR wide swath backscatter, *IEEE Geoscience and Remote Sensing Society, 11*(8), 1423 – 1427, doi: 10.1109/LGRS.2013.2294725, 2014.

van Huissteden, J., and A. Dolman, Soil carbon in the Arctic and the permafrost carbon feedback, *Current Opinion in Environmental Sustainability, 4*(5), 545 – 551, doi: 10. 1016/j.cosust.2012.09.008, terrestrial systems, 2012.

Vasiliev, A. A., M. O. Leibman, and N. G. Moskalenko, Active layer monitoring in West Siberia under the CALM II Program, in *Proceedings of the Ninth International Conference on Permafrost*, vol. 2, edited by D. L. Kane and K. M. Hinkel, pp. 1815–1820, Institute of Northern Engineering, University of Alaska Fairbanks, 2008.

Virtanen, T., K. Mikkola, and A. Nikula, Satellite image based vegetation classification of a large area using limited ground reference data: A case study in the Usa Basin, north-east European Russia, *Polar Research, 23*, 51–66, doi: 10.1111/j.1751-8369.2004.tb00129.x, 2004.

Wagner, W., G. Lemoine, and H. Rott, A method for estimating soil moisture from ERS scatterometer and soil data, *Remote Sensing of the Environment, 70*, 191–207, 1999.

Walker, D., W. Gould, H. Maier, and M. Raynolds, The Circumpolar Arctic Vegetation Map: AVHRR-derived base maps, environmental controls, and integrated mapping procedures, *International Journal of Remote Sensing, 23*(21), 4551–4570, 2002.

Walker, D., et al., Data report of the 2007 and 2008 Yamal expeditions, Alaska Geobotany Center, Institute of Arctic Biology, University of Alaska Fairbanks, Fairbanks, AK. 121 pp., 2009.

Walker, D. A., et al., The Circumpolar Arctic Vegetation Map, *Journal of Vegetation Science*, *16*(3), 267–282, 2005.

Wang, C., H. Zhang, Q. Wu, Z. Zhang, and L. Xie, Monitoring permafrost soil moisture with multi-temporal TERRASAR-X data in northern Tibet, *Geoscience and Remote Sensing Symposium (IGARSS), 2016 IEEE International*, doi: 10.1109/IGARSS.2016.7730558, 2016.

Watts, J., J. Kimball, A. Bartsch, and K. McDonald, Surface water inundation in the boreal- Arctic: potential impacts on regional methane emissions, *Environmental Research Letters*, *9*, 075,001, 2014.

Werninghaus, R., W. Balzer, S. Buckreuss, J. Mittermayer, and P. Mhlbauer, The TerraSAR-X mission, in *SPIE 5236, SAR Image Analysis, Modeling, and Techniques VI*, doi: 10.1117/12.511500, 2004.

Westermann, S., C. R. Duguay, G. Grosse, and A. Kääb, *Remote sensing of permafrost and frozen ground*, chap. 13, p. 408, Wiley Blackwell, doi: 10.1002/9781118368909.ch13, 2015a.

Westermann, S., T. I. Østby, K. Gisnås, T. V. Schuler, and B. Etzelmüller, A ground temperature map of the north atlantic permafrost region based on remote sensing and reanalysis data, *The Cryosphere*, *9*(3), 1303–1319, doi: 10.5194/tc-9-1303-2015, 2015b.

Whitcomb, J., M. Moghaddam, K. McDonald, J. Kellndorfer, and E. Podest, Mapping vegetated wetlands of Alaska using L-band radar satellite imagery, *Canadian Journal of Remote Sensing*, *35*, 54–72, 2009.

Wickel, A. J., T. J. Jackson, and E. F. Wood, Multitemporal monitoring of soil moisture with RADARSAT SAR during the 1997 Southern Great Plains hydrology experiment, *International Journal of Remote Sensing*, *22*(8), 1571–1583, 2001.

Widhalm, B., A. Bartsch, and B. Heim, A novel approach for the characterization of tundra wetland regions with C-band SAR satellite data, *International Journal of Remote Sensing*, *36*(22), 5537–5556, doi: 10.1080/01431161.2015.1101505, 2015.

Widhalm, B., A. Bartsch, M. B. Siewert, G. Hugelius, B. Elberling, M. Leibman, Y. Dvornikov, and A. Khomutov, Site scale wetness classification of tundra regions with C-band SAR satellite data, in *Proc. 'Living Planet Symposium 2016', Prague, Czech Republic*, ESA SP-740, 2016.

Widhalm, B., A. Bartsch, M. Leibman, and A. Khomutov, Active-layer thickness estimation from X-band SAR backscatter intensity, *The Cryosphere*, *11*(1), 483–496, doi: 10.5194/tc-11-483-2017, 2017.

Widhalm, B., A. Bartsch, and R. Goler, Simplified normalization of C-band synthetic aperture radar data for terrestrial applications in high latitude environments, *Remote Sensing*, *10*(4), doi: 10.3390/rs10040551, 2018.

Widhalm, B., A. Bartsch, A. Roth, and M. Leibman, Classification of tundra regions with polarimetric TerraSAR-X data, in *Proc. 'IGARSS 2018', Valencia, Spain*, in press.

Woodhouse, I., *Introduction to Microwave Remote Sensing*, Taylor & Francis, New York:, 2006.

Yershov, E. D., *General Geocryology*, Cambridge University Press, Cambridge, 1998.

Zhang, Z., C. Wang, Y. Tang, and H. Zhang, Surface deformation monitoring using time series TerraSAR-X images over permafrost of Qinghai-Tibet Plateau, China, *Geoscience and Remote Sensing Symposium (IGARSS), 2016 IEEE International*, doi: 10.1109/IGARSS.2016.7730558, 2016.

Zhu, Z., S. Wang, and C. E. Woodcock, Improvement and expansion of the Fmask algorithm: cloud, cloud shadow, and snow detection for Landsats 4-7, 8, and Sentinel 2 images, *Remote Sensing of Environment*, *159*, 269 – 277, doi: https://doi.org/10.1016/j.rse.2014.12.014, 2015.

Zwieback, S., X. Liu, S. Antonova, B. Heim, A. Bartsch, J. Boike, and I. Hajnsek, A statistical test of phase closure to detect influences on DInSAR deformation estimates

besides displacements and decorrelation noise: Two case studies in high-latitude regions, *IEEE Transactions on Geoscience and Remote Sensing, 54* (9), 5588–5601, doi: 10.1109/ TGRS.2016.2569435, 2016.